CARBON NANOTUBE FILM BASED NANOCOMPOSITES FOR STRETCHABLE ENERGY STORAGE DEVICES

by

Taoli Gu

A dissertation submitted to the Faculty of the University of Delaware in partial fulfillment of the requirements for the degree of Doctor of Philosophy in Mechanical Engineering

Spring 2017

© 2017 Taoli Gu
All Rights Reserved

CARBON NANOTUBE FILM BASED NANOCOMPOSITES FOR STRETCHABLE ENERGY STORAGE DEVICES

by

Taoli Gu

Approved: _____
Suresh G. Advani, Ph.D.
Chair of the Department of Mechanical Engineering

Approved: _____
Babatunde A. Ogunnaike, Ph.D.
Dean of the College of Engineering

Approved: _____
Ann L. Ardis, Ph.D.
Senior Vice Provost for Graduate and Professional Education

I certify that I have read this dissertation and that in my opinion it meets the academic and professional standard required by the University as a dissertation for the degree of Doctor of Philosophy.

Signed: _____

Bingqing Wei, Ph.D.
Professor in charge of dissertation

I certify that I have read this dissertation and that in my opinion it meets the academic and professional standard required by the University as a dissertation for the degree of Doctor of Philosophy.

Signed: _____

Tsu-Wei Chou, Ph.D.
Member of dissertation committee

I certify that I have read this dissertation and that in my opinion it meets the academic and professional standard required by the University as a dissertation for the degree of Doctor of Philosophy.

Signed: _____

Joseph P. Feser, Ph.D.
Member of dissertation committee

I certify that I have read this dissertation and that in my opinion it meets the academic and professional standard required by the University as a dissertation for the degree of Doctor of Philosophy.

Signed: _____

Chaoying Ni, Ph.D.
Member of dissertation committee

ACKNOWLEDGMENTS

These years at the University of Delaware were challenging, and I would like to give thanks for all the encouragement and help that make me through.

First of all, I would like to sincerely thank Professor Bingqing Wei, my advisor in Mechanical Engineering of the Ph.D. program, for guiding me into electrochemistry and energy storages field, for providing me with the research resources and unique insight in research direction, for always encouraging me to challenge myself, for discussing the research process very patiently. I am proud of being his student.

I would like to thank all the other committee members, Professor Tsu-Wei Chou, Professor Joseph P. Feser and Professor Chaoying Ni for serving on my committee in the Ph.D. dissertation defense, I also want to thank Professor Joshua Hertz for being my former candidacy defense committee member; not only for their encouragement, but also constructive feedback to make my final defense possible.

Without the support of the finest co-workers, I would not have been achieved so much during my time at the University of Delaware. I want to thank my former and current group members Mr. Xin Li, Dr. Qing Zhang, Dr. Zeyuan Cao, Dr. Kun Liang, and Dr. Tong Li for their help and feedback during my Ph.D. experience. In addition, I would like to thank Professor Feng Jiao, Dr. Bryan Yonemoto and Mr. Ning Ye for providing equipment support in the materials synthesis and electrochemical testing; Dr. Fei Deng and Professor Chaoying Ni for training me the basic materials characterization techniques such as SEM, TEM, AFM, and FIB.

Outside the lab, department staffs provided so many help to make me adopt to the graduate life. I would also like to thank Mrs. Lisa Katzmire, Mr. Roger Stahl, Mrs. Letitia Toto, Mr. Steven Beard, and Mrs. Ann Connor.

I want to thank all my dear friends at the University of Delaware, especially Dr. Qing Sun, Mr. Xuekai Zhang, Dr. Xiaogang Chen, Ms. Yinxin Lin, Dr. Fei Zhang, Mr. Yilu Zhou, and Dr. Zheyu Zhou for making life interesting and exciting throughout my time in UD.

I want to thank my uncle Mr. Jianjun Gu, who encourages me to be optimistic and confident when I meet great difficulties. I want to thank Ms. Hui Zhao, for her love and support. Finally, I would like to express my appreciation to my dearest parents, mother Yan-er Zhou and father Jianguo Gu, for their love and persistent encouragement. Without all of them, I would not be who I am today.

I cannot name everyone, but I am grateful for all the help from them for my six years in the University of Delaware.

DEDICATION

To my mother, Yan-er Zhou and father, Jianguo Gu

TABLE OF CONTENTS

LIST OF TABLES

LIST OF FIGURES

LIST OF ABBREVIATIONS

ASC Asymmetric supercapacitor

ASS Asymmetric stretchable supercapacitor

BET Brunauer-Emmett-Teller

CE Columbic efficiency

CNT Carbon nanotube

CV Cyclic voltammetry

CVD Chemical vapor deposition

DEC Diethyl carbonate

DSP Dynamically stretchable pseudocapacitor

DSR Dynamic stretching-releasing

DBR Dynamic bending-releasing

EC Ethylene carbonate

EDLC Electric double-layer capacitor

EIS Electrochemical impedance spectroscopy

Fe_2O_3 Iron oxide

GCD Galvanostatic charge-discharge

$KMnO_4$ Potassium permanganate

LMO Lithium manganese oxide

LIB Lithium-ion battery

MnO_2 Manganese dioxide

NSSP Non-sandwich stretchable pseudocapacitors

PC Propylene carbonate

PDMS Polydimethylsiloxane

SC Supercapacitor

SEM Scanning electron microscopy

SSP Sandwich-like stretchable pseudocapacitors

SWNT Single-walled carbon nanotube

$TEABF_4$ Tetraethylammonium tetrafluoroborate

TEM Transmission electron microscopy

TGA Thermal gravimetric analysis

XEDS X-ray energy dispersive spectroscopy

XPS X-ray photoelectron spectroscopy

XRD X-ray diffraction

ABSTRACT

Stretchable electronics are robust and functional when being mechanically bent, folded, twisted, and even stretched. They are attracting intense attention due to their promising applications in portable electronics and bio-implantable devices with arbitrarily adjustable surfaces. To power them, stretchable energy storage devices are the essential for the fabrication of independent and complete stretchable electronic systems. Material synthesis and structural design are the core of highly stretchable energy storage devices. Utilizing carbon nanotube (CNT) films as stretchable electrodes in supercapacitors has demonstrated excellent functionality and cycling stability. However, the main drawback of such a stretchable electric double-layer supercapacitor suffers from a low specific capacitance and energy density. In this dissertation, research efforts have been focused on three major breakthroughs in CNT film-based stretchable pseudocapacitors, stretchable asymmetric supercapacitors, as well as stretchable lithium-ion batteries, all of them exhibit excellent mechanical property and improved electrochemical performance.

The realization of dynamically stretchable pseudocapacitors using buckled MnO_2/CNT hybrid electrodes has been achieved. The stable electrochemical performance of the dynamically stretchable pseudocapacitors under various bending/stretching conditions is attributed to a fast redox reaction at the MnO_2/CNT hybrid electrodes, indicated by the extremely small relaxation time constant of less than 0.15 s. To increase the mass loading of the pseudo-capacitive materials in stretchable MnO_2/CNT electrodes so as to improve the energy density of the

pseudocapacitors, a novel all-solid-state sandwich-like capacitor design has been proposed and constructed, which overcomes the loading limitation of active materials and exhibits excellent structural and electrochemical stabilities. This novel component-level design can also be extended for improving the performance of other stretchable electrochemical systems. Afterward, we devote to developing a high operating voltage stretchable supercapacitor by taking advantage of the asymmetric design with MnO_2/CNTs as the positive electrode and Fe_2O_3/CNTs as the negative electrode. Due to the synergistic effects of the two electrodes with an optimized potential window, the stretchable cell voltage is increased to 2 V, and the energy density is significantly enhanced.

Based on the successes on stretchable supercapacitors, a more challenge task for developing reliable and stretchable lithium-ion battery has been tackled. A bottle neck issue has been resolved by applying a low-temperature hydrothermal synthesis to fabricate the stretchable $LiMn_2O_4$/CNT cathode. Chemical bonding is confirmed between the active materials and CNT scaffolds for the first time, which is the most important characteristic of the stretchable electrodes in a lithium-ion battery system.

With the unique mechanical and electrochemical properties, a variety of new technologies, such as smart textiles, soft robotics, active medical implants, and stretchable consumer electronics will benefit from the CNT film-based stretchable energy storage devices.

Chapter 1

INTRODUCTION

1.1 General

Ever-increasing energy demands, as well as diminishing fossil fuel, require the urgently searching for sustainable energy storage systems that are reliable, low-cost and environmentally friendly. This is one of the greatest global challenges that our society is facing nowadays.[1-5] Continuous progress in developing electrochemical energy storage systems such as lithium-ion batteries (LIBs) and supercapacitors (SCs) for their applications ranging from electric vehicles, hybrid electric vehicles and portable devices to grid storage over the last three decades has been rapidly moving forward.[6-10]

Very recent years, electronics that can be bendable, foldable, twistable, and even stretchable, such as wearable electronics, electronic papers, bendable smartphones, stretchable displays, and bio-implantable medical devices have been urgently needed.[11-13] To power these devices, there is a persistent requirement for developing equally flexible and stretchable energy storage devices, which can be conformal with adjustable deformation while maintaining their electrochemical and mechanical performance.[14-16] Stretchable energy storage devices, such as stretchable LIBs and SCs, claim higher requirements with the material properties and structural design compared to the flexible ones. The simple bendability in traditional flexible devices sustaining the induced strains $\leq$ 1% is far insufficient from a practical application where the stretchable devices would experience much more challenging

stretching-releasing which must accommodate a large tensile strain deformation >>1% when coupled with arbitrarily shaped surfaces.[17-20] Hence, it is believed that achieving the flexibility/bendability is just the very first step to accomplishing fully stretchable devices. Stretchable energy storage is an emerging area and will require more attention and finally becomes mainstream technologies in the near future.

Very recently, research on stretchable energy storage devices has been focused on various stretchable strategies such as wire-shaped,[21-23] textile-structural,[24-26] and interconnect-island-mesh configurations,[27,28] etc., with little attention paid to increasing their energy density and longer cycling life (both mechanical and electrochemical) requirements.[29-31] Besides, the development of stretchable LIBs is underdeveloped due to their relative difficulty in fabrication and operation, which prevents the stretchable energy storage devices as a reliable power source from practice. Our study on carbon nanotube (CNT) film-based stretchable pseudocapacitors, stretchable asymmetric supercapacitors, and stretchable LIBs not only fills the blank in the "wavy-configuration" high-performance stretchable energy storage, but also aims at attaining a more comprehensive understanding of the role of dynamically mechanical deformation on the performance of the stretchable energy storage devices. This will be helpful in providing extremely valuable guidelines for the design optimization of the next-generation stretchable energy storage devices, thus finally explores the potential commercialization in their applications for stretchable electronics.

1.2 Carbon Nanotube Films

Nanostructured carbon materials have been extensively studied and widely used as the electrode materials in energy storage systems, due to their high

conductivity, high specific surface area, high-temperature stability, excellent anti-corrosion property, controllable porous structure, and relatively low cost.[32-35] Currently, they are also the ideal scaffold/substrates or conductive additives to be coupled with active materials to form composite electrodes for energy storage applications.[36-39]

1.2.1 Synthesis by chemical vapor deposition

Among those nanostructured carbon materials, CNT is one of carbon allotropes with a unique one-dimensional cylindrical nanostructure. Chemical vapor deposition (CVD) becomes the top choice method for large-scale production of CNT films.[40] The experimental setup for the CVD growth consists of a gas system to deliver a desirable gas atmosphere and a heating system which is a ceramic tube furnace shown in Figure 1.1a. The detailed procedure for preparing the CNT films is described as follows: Two chemical feedstock, ferrocene powder (acting as the carbon source and catalyst) and sulfur powder (serving as the single-walled CNT promotion additive) are heated up to 1150 ^{o}C, while argon gas and pure hydrogen gas were introduced into the furnace at the same time. Sulfur powder acts as an additive to promote the single-walled CNT growth and is widely recognized as a predominant in controlling the wall numbers of an individual CNT. During the heating process, the ceramic tube can be shifted in the furnace, so the mixture of ferrocene and sulfur (atomic ratio Fe:S = 10:1) is located in the appropriate heating area in the furnace. After 30 mins reaction time, the furnace is cooled down to room temperature while still keeping the argon gas running to protect the formation of CNT films. The thickness of the film can be easily controlled by the amount of the chemical feedstock and deposition time, which is in the range of hundreds of nanometers to hundreds of microns. CNT films can be collected on the

top ceiling inside the ceramic tube both near inlet and outlet region. Figure 1.1b shows the as-synthesized CNT films. The film area can be up to 200 cm^2. The inset in Figure 1.1b shows a typical scanning electron microscopy (SEM) image of CNT films after post-treatment. As shown in the figure, the CNT film is extremely purified, with a combination of the mesoporous and microporous structures.

This direct deposition of CNT films outperformed other synthesis methods of CNT with several advantages: Firstly, the precursor only contains a solid component and no gas, or liquid carbon sources are introduced. Secondly, the films can be directly deposited on various flexible metallic foils substrates (e.g. copper foil, stainless steel, etc.) during the synthesis process. Lastly, the as-deposited CNT films can be easily peeled off from any substrates with flexibility and bendability and could be further made stretchable when coupled with the pre-stretched polydimethylsiloxane (PDMS) by using the simple pre-strain-then-buckling method.

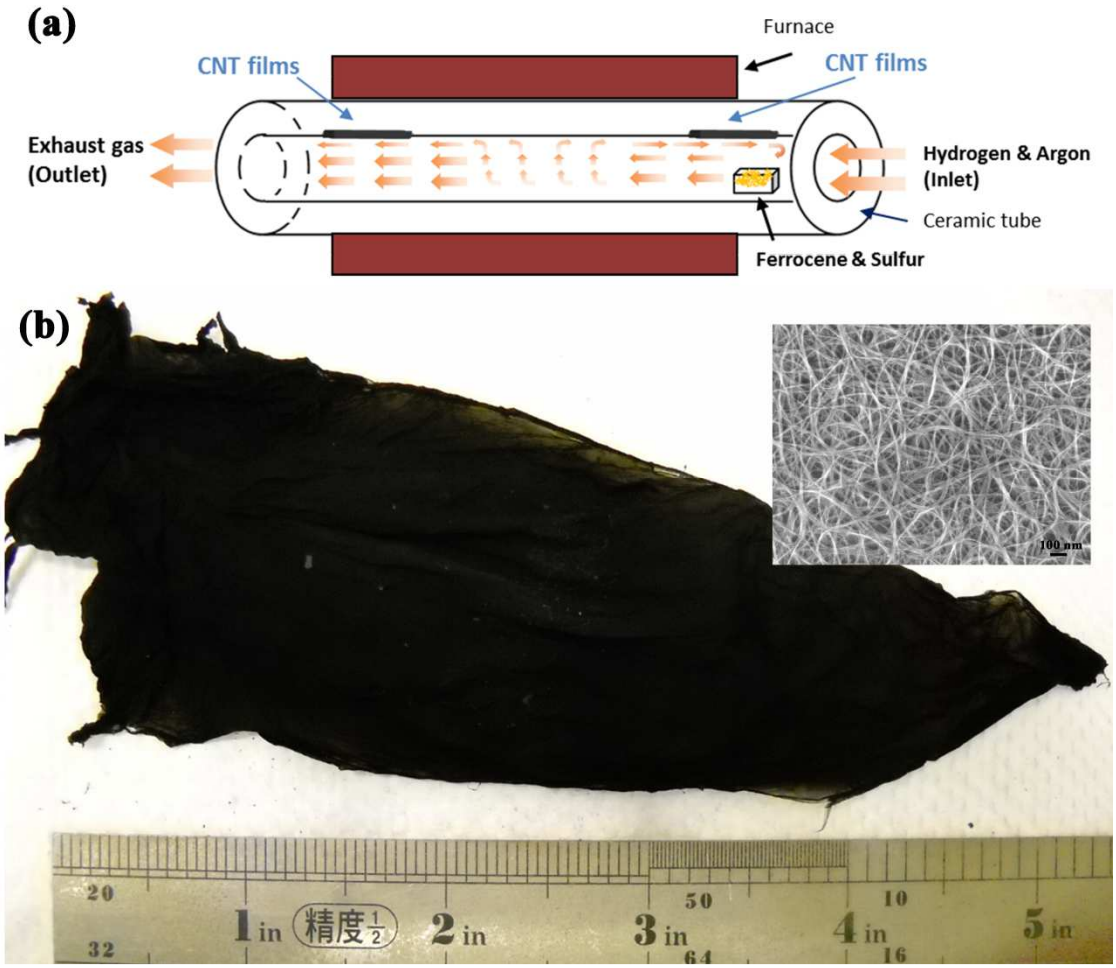

Figure 1.1 (**a**) Illustration of CVD growth process of large-scale CNT films. (**b**) The photography of CVD products with SEM image (inset) showing the morphology of entangled CNT network.

1.2.2 Unique properties

Compared with other nanostructured CNTs in the powder form,[41-43] CNT films with controllable mesh-like networks, which are self-assembled by CNTs as building blocks, provide unique properties in terms of mechanical robustness, large specific surface area, thermal stability, and superior electrical conductivity ($10^4 \sim 10^5$ S cm^{-1})

in a more stable and flexible integrity. The films are ideal free-standing and binder-free electrodes for next-generation energy storage devices.

To be specific, the original CNT films without any post-treatment after production have a porous structure with the large specific surface area and contain impurities such as amorphous carbon and iron catalysts derived from the pyrolysis of ferrocene during the high-temperature synthesis. The next step post-purification can remove the impurities and also transform the original hydrophobic surface to hydrophilic by increasing surface functional groups such as hydroxyl and carboxyl without damaging the integrity of the films. Post-purification process with heat treatment in air at 450 °C for 60 mins and afterward rinsing with acid (37% HCl) are often used. The purified films still maintain the porous structures (Inset in Figure 1.1b). The presence of oxygen-containing functional groups could also improve the adhesion of CNT films with other active materials to form nanocomposite electrodes for LIBs and SCs. When the films are under ultrasonication in alcohol, their intrinsic sticky properties are unchanged, also making them a potential conductive additive. Most importantly, CNT films exhibit excellent stretchability up to 150% when coupled with PDMS, and it is also important that the electrical resistance experiences no remarkable change even under 120% tensile strain.

In conclusion, all of these unique properties including high stretchability, homogeneous and controllable porous size, superior electrical conductivity, adhesive surface, as well as functionality into nanocomposites,[44] awards the CNT films to open a promising field and worth the investigation and research of their potential candidates for stretchable energy storage systems.

1.3 Supercapacitors

1.3.1 Principle

Supercapacitors, also refer to ultra-capacitors, are attracting increasing applications in bio-implantable devices, hybrid electric vehicles, and renewable energy stationary plants.[45-47] According to different charge storage mechanisms, SCs are classified into three major types: electric double-layer capacitors (EDLCs)[48], pseudo- or redox capacitors[49] and asymmetric supercapacitors (ASCs)[50]. Based on the types of electrolytes, the supercapacitors can be mainly classified to aqueous, including acidic solutions such as sulfuric acid (H_2SO_4)[51], neutral solutions (e.g. sodium sulfate (Na_2SO_4)[52]), and alkali solutions (e.g. sodium hydroxide (NaOH)[53]), and non-aqueous, including organic solutions such as tetraethylammonium tetrafluoroborate ($TEABF_4$) in propylene carbonate (PC)[54], and ionic liquids[55-57]. The potential window of a supercapacitor is mainly determined by the electrolyte. The aqueous-based supercapacitors usually have a relatively narrow potential window which is usually less than 1.2 V, while it can be extended more than 3 V by switching to an organic electrolyte. A typical supercapacitor configuration normally assembled in a cell design similar to LIB in practical application, which consists of two electrodes (symmetric or asymmetric) immerse in the electrolyte and a separator that electrically isolates them.

Supercapacitors provide high power density, moderate energy density, fast charge-discharge, and ultra-long cycling life compared to batteries. The specific capacitance (C) of a supercapacitor is defined in Equation 1.1

$$C = \frac{Q}{V} \qquad (1.1)$$

where Q is the charge stored on the electrode and V is the potential operating window.

The energy density (E) of a supercapacitor is defined as in Equation 1.2:

$$E = \frac{C V^2}{2} \qquad (1.2)$$

The maximum power density (P_{max}) of a supercapacitor is expressed by Equation 1.3:

$$P_{max} = \frac{V^2}{4R} \qquad (1.3)$$

where R is the equivalent series resistance of all the components in the device.

1.3.2 Electric double-layer capacitors

Electric double-layer capacitors take advantage of the electrical double-layer at the interface between the electrode and the electrolyte. The accumulation of electrons at the electrode is a non-Faradaic process (Figure 1.2a). The electric double-layer is formed through the accumulation of electrolyte ions at the electrode/electrolyte interface during charge and discharge processes. Accordingly, the capacitance is contributed by electrostatic separation of charges at interfaces of electrodes/electrolytes, referenced as the Helmholtz double-layer. Applying a potential across two electrodes of a supercapacitor will form double layers at both electrodes. To be specific, double layers in one electrode consist of two layers of ions: the first layer is due to the charge polarization at the surface near the electrode. The second layer emerges due to the absorption of solvated ions coming from the electrolyte. Between the two layers, there is usually a monolayer of solvent molecules, e.g. water molecules for the aqueous electrolyte. The monolayer generates the inner Helmholtz plane effects by physically adsorbing on the electrode and separating the oppositely polarized ions from each other. A number of charges in the electrode is exactly matched by the number of counter-charges in the outer Helmholtz plane.

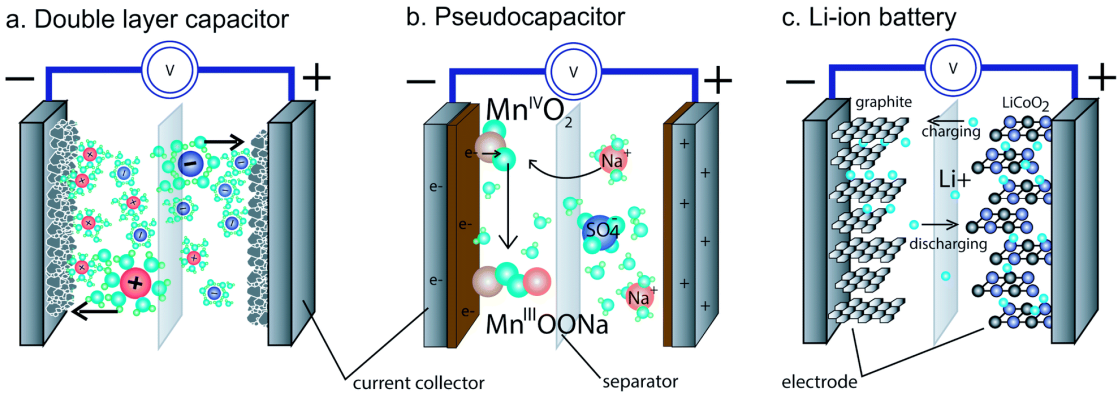

Figure 1.2 Illustrations for an (**a**) all carbon EDLC, (**b**) a pseudocapacitor and (**c**) a lithium-ion battery. All devices have an active material (e.g., carbon, MnO_2, $LiCoO_2$), current collectors, a separator, and an electrolyte, (e.g., Na_2SO_4, or $LiPF_6$ solutions). Reprinted with permission from reference 104 @ 2014, Royal Society of Chemistry

The specific capacitance (C_{dl}) of an EDLC is measured as in Equation 1.4:

$$C_{dl} = \frac{\varepsilon_r \varepsilon_0}{d} A \qquad (1.4)$$

where ε_r is the relative permittivity of the medium in the double-layer, ε_0 is the vacuum permittivity, A is the specific surface area of the electrode, and d is the effective thickness of the double-layer. In this equation, we can find that it is the larger surface area and the extremely shorter distance between the double layers will contribute to the higher specific capacitance.

1.3.3 Pseudocapacitors

Pseudocapacitors can usually deliver a capacitance with more than 10 or 100 times of EDLCs because they not only store charges in the electric double-layer but take advantage of the charge-transfer process through reversible Faradaic reactions. The basic requirement is that the electrode materials should have electrochemical redox activity with the electrolytes (Figure 1.2b). This process is similar to the

charge-discharge in batteries where the passage of Faradaic current occurs but different from a LIB, in which the ions are deeply intercalated into the material's lattice, the pseudo-capacitance is originated from the weakly attached surface ions. The adsorbed ions have no chemical reaction with the atoms of the electrode. In other words, no chemical bonds forms but only a charge-transfer process takes place. In general, conductive polymers and metal oxides are common electrode materials for pseudocapacitors.

In particular, some metal oxides show excellent pseudo-capacitance. Table 1.1 lists the theoretical capacitance of typical metal oxides as well as the charge storage reactions. It can be seen that the transition metal oxide electrodes have at least one order higher specific capacitance than carbon electrodes.[58] Metal oxide electrodes can deliver a large specific capacitance and high energy density at a low current density, however, with increased current densities, the retention is extremely poor. Therefore transition metal oxides may not be applied alone as the pseudocapacitor electrodes for practical due to some drawbacks.[59-62] To be specific, the electrical conductivity of most metal oxides except ruthenium (IV) oxide (RuO_2)[63] is very low. The high resistance of transition metal oxides increases the charge-transfer resistance of the electrode and causes a large internal resistance loss at high current densities. Thus the power density and the rate capability are very poor, which hinders their practical application. Besides, the strain in the transition metal oxide during the charge-discharge processes causes the unreturnable cracking of the structure, leading to poor cycling stability.

It is desirable to develop a nanocomposite electrode containing both carbon materials and transition metal oxide as the pseudocapacitor electrode, which combines

the merits of both components. On the one hand, in such nanocomposite electrode systems, the carbon materials not only serve as the support of metal oxides but also provide the conductive channels for fast charge transport. The high conductivity of carbon nanostructures benefits the rate capability and power density at a high charge-discharge rate. The CNT film discussed in the earlier section is such a good candidate due to its intrinsic property. The surface functional groups in CNT, the defects, and the grain boundaries can also serve as the redox centers for the charge storage reactions. On the other hand, the transition metal oxides are the primary sources that store the energy; it contributes mainly to high specific capacitance and thus high energy density of the nanocomposite electrodes. A synergistic effect could be expected, and the material cost can be reduced.

Table 1.1 Pseudo-capacitance of selected typical metal oxides

Oxide	Charge storage mechanism	Theoretical capacitance ($F\ g^{-1}$)
MnO_2	$MnO_2 + \mathbf{M}+ e^- = \mathbf{M}MnO_2$ (**M** could be H^+, Li^+, Na^+, TEA^+, $BMMI^+$)	1380(ref.64)
Co_3O_4	$Co_3O_4 + OH^- + H_2O = CoO_2 + H_2O + e^-$	3560(ref.65)
V_2O_5	$V_2O_5 + 4\mathbf{M} + 4e^- = \mathbf{M}_4V_2O_5$ (**M** could be H^+, Li^+, Na^+, TEA^+, $BMMI^+$)	2120(ref.66)
$RuO_2.xH_2O$	$RuO_2 + xH^+ + xe^- = RuO_{2-x}.(OH)_x$ $(0 < x < 2)$	2200(ref.63)

1.3.4 Asymmetric supercapacitors

The supercapacitor can also be constructed in an asymmetric configuration by pairing one EDLC with one pseudo- electrode or one pseudo- with another kind of pseudo- electrode, which is called asymmetric supercapacitors, differing from the symmetric supercapacitor with two identical electrodes. Recently, designing ASCs has

been an effective approach to increase the specific energy density of aqueous symmetric supercapacitors.[67-69] Asymmetric supercapacitors usually consist of a redox reaction positive electrode (e.g. metal oxides as the energy source) and an EDLC-type negative electrode (e.g. carbon materials as the power source) that can make full use of the different potential windows of the two electrodes to increase the operational potential, which thus beyond the maximum potential (~1.2 V) in the aqueous electrolyte cell system, accordingly resulting in a significantly improved energy density (Equation 1.2). Therefore, ASCs simultaneously carry both the advantages of SCs (relatively high rate capability) and LIBs (relatively high energy density).[70-71]

1.3.5 Electrochemical tests and calculation

The electrochemical testing techniques such as galvanostatic charge-discharge (GCD), cyclic voltammetry (CV) and electrochemical impedance spectroscopy (EIS) are the three most common techniques to measure the specific capacitance, rate capability, cycling stability, resistance, and diffusion of supercapacitors. Commercially, supercapacitors are packaged in the two-electrode design. Three-electrode cell consists of a working electrode, a reference electrode, and a counter electrode. The three-electrode testing method is usually applied for detecting the stable potential windows of positive and negative electrodes for ASCs. For example, the electrochemical performance of the positive and negative electrodes are investigated in a three-electrode system using platinum foil, Ag/AgCl, and 1 M Na_2SO_4 aqueous solution as the counter electrode, reference electrode, and electrolyte, respectively. Both electrodes (positive and negative) usually show a stable potential window, which can be used to pair them into the ASC cell.[72,73] Three-electrode cells differ from the two-electrode cells in many important aspects. To begin with, in the

three-electrode configuration, only one electrode, i.e. the working electrode, is made of an active material being analyzed. The charge transfer process under applied potential across the working electrode is markedly different from that in a two-electrode configuration. For a three-electrode cell, the potential applied to the working electrode is versus the reference electrode. In other words, the three-electrode cell is valuable for analyzing the faradic reactions and voltages at a single surface. In addition, the potential across counter electrode in a three-electrode cell is not controlled or measured.[74,75]

The specific capacitance (C) was usually calculated from the discharge of GCD curves based on Equation 1.5:

$$C = \frac{I \times \Delta t}{m \times \Delta V} \qquad (1.5)$$

where m, I, Δt, ΔV are the weight of the electrode materials, discharge current density, the discharge time, and the discharge potential range, respectively.

1.3.6 Carbon-based stretchable supercapacitors

Bendable, foldable, twistable, and even stretchable are needed for SCs to meet the increasing market requirement,[76-78] representing a new direction in research. Compared to stretchable LIBs, stretchable SCs have been developed rapidly due to relatively easier fabrication and structure design.

There has been considerable research on flexible energy storage systems over more than two decades, while the stretchable batteries and SCs have not attracted much attention since the pioneering work by our group in 2009.[79] As discussed above, CNTs possess not only superb electrochemical performance but also excellent mechanical robustness. In our previous research work, a periodically buckled CNT film structure could be formed by using the pre-strain-then-bucking method (Figure

1.3a), owing to different mechanical property between the stiffer CNT film and the compliant PDMS substrate (Figure 1.3b). This pre-strain-then-bucking usually consists of three steps: 1) perstraing the elstomeric substrate (PDMS); 2) transferring the CNT on the pre-stretched substrate; and 3) releasing of the substrate. The results showed no significant change in the GCDs and CVs of the stretchable SCs with 0 and 30% strains. The initial specific capacitance was found to change from 54 F g^{-1} to 52 F g^{-1} for the stretchable SCs under 30% strain (Figure 1.3c).

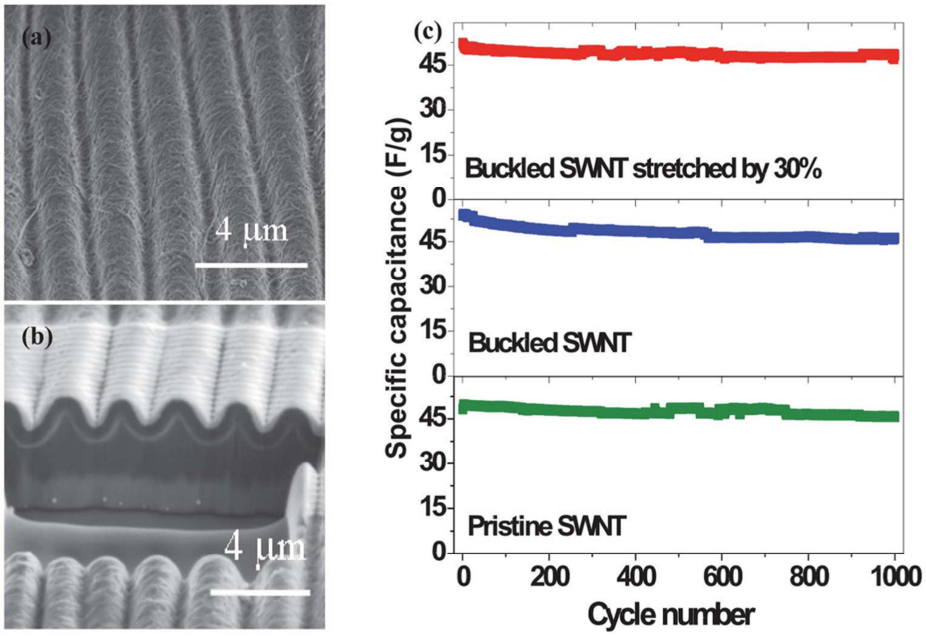

Figure 1.3 (**a** and **b**) SEM images of buckled CNT films. (**c**) The comparison of specific capacitance for the supercapacitors based on buckled CNT films under 30% strain, buckled CNT films without pre-strain and pristine CNT films. Reprinted with permission from reference 79 @ Copyright 2009 WILEY-VCH Verlag GmbH & Co. KGaA, Weinheim

In order to further understand the dynamic coupling effects of mechanical-electrochemical properties in fully stretchable EDLCs, we have also investigated a dynamically stretchable EDLC with simultaneously monitored electrochemical behavior under dynamic stretching-releasing (DSR) modes.[80] It is found that the CV curve under the DSR mode (e. g. the strain rate of 2.22% strain·s^{-1}) shifts between the two static CV curves with 31.5% and 0% static strains (Figure 1.4a). Accordingly, the capacitances calculated from the GCD testing of the EDLC under all DSR strain rates (1.11%, 2.22%, and 4.46% strain·s^{-1}) are in the range between 0% and 31.5% static strain ones (Figure 1.4b). The possible reason for these patterns is due to the variation in the electrode/electrolyte interface under different mechanical states, resulting in the change of the charge-transfer and Warburg diffusion resistance. EIS result further confirms that these trends are mainly contributed by the much increased Warburg diffusion resistance under the DSR mode, compared with the static state of the stretchable cells (Figure 1.4c). At 0% strain, the buckled CNT electrode with wavy structure leads to the high resistance at the electrode/electrolyte interface as well as the ionic diffusion length, while at 31.5% strain, the pre-buckled CNT electrode is almost flat with less ionic diffusion length, thus in favor of faster kinetics (Figure 1.4d). Thus, at 4.46% strain·s^{-1}, the diffusion process is slightly improved, compared to that at 1.11% and 2.22% strain·s^{-1}, which could be attributed to the faster changing of the wavy structure, leading the ions to be kept within the effective outer diffuse layer. Hence, this CNT-based novel "wavy" strategy provides a promising approach for the stretchable EDLCs for in wearable electronic devices. Afterward, many studies followed our group’s work and have also demonstrated the feasibility of the buckled CNT to achieve stretchability as well as excellent electrical conductivity.

Lu et al. demonstrated a multi-wall carbon nanotube(MWCNT)-based stretchable supercapacitor via a facile water-surface-assisted synthesis.[81] By combining the excellent conductivity of MWCNTs with the high stretchability of PDMS, this 3-D network exhibited a high conductivity of 4.19 S cm^{-1} and could be stretched to 50% strain without affecting its conductivity. The MWCNT-based stretchable supercapacitor possessed more than 95% capacitance retention after 500 charge-discharge cycles.

Moreover, textile materials are also used as stretchable substrates to carry carbon-based materials. With the simple "dipping" process using CNT ink, Hu et al. demonstrated highly conductive textiles with the specific capacitance of 60 F g^{-1}.[82,83] Besides, by using two highly aligned CNT sheets as both the current collector and electrode, Chen et al. fabricated a transparent stretchable supercapacitors with a specific capacitance of 7.3 F g^{-1}, which can also be biaxial stretched up to 30% without obviously capacitance loss under hundreds of stretching and releasing cycles.[84]

Wire-shaped design for stretchable supercapacitors were also attracted plenty of attentions. Xu et al.[22] studied a stretchable wire-shaped supercapacitor consisting of two CNT fiber electrodes twisted together on a spandex fiber, with specific capacitance of 4.99 mF cm^{-2}, and the ability to undergo large tensile strain of 100%. The electromechanical performance was improved after 20 mechanical cycles. Such wire-shaped supercapacitor still suffer from the low capacitance, low working potential (usually 0.8V), and thus low energy and power densities, preventing them from practical applications. Xu et al.[85] then reported a stretchable asymmetric supercapacitor with MnO_2/CNT hybrid fiber as the positive electrode and CNT fiber

as the negative electrode, and KOH-PVA gel as electrolyte. The wire-shape supercapacitor possessed a high specific capacitance of 157.53 μF cm^{-1} at 50 mV s^{-1} and a high energy density of 46.59 nW h cm^{-1} with the corresponding power density of 7.63 μW cm^{-1}. Additionally, after 10,000 cycles, the specific capacitance retention was ~ 99%, demonstrating its long cycling stability.

Other stretchable EDLCs such as stretchable graphene-based supercapacitors are also fast developed.[86-89] Xu et al.[87] demonstrated a laminated ultrathin four-layer CVD graphene film electrode for stretchable SCs, the specific capacitance showed no degradation until the tensile strain increased up to 40%. Moreover, Li et al.[89] fabricated rGO-based stretchable SCs via pressure spray printing and machine coating, high and adjustable volumetric capacitance with 77.9 F cm^{-3} with the 5 μm rGO layer was achieved. A transparent stretchable SC based on CVD grown wrinkled multilayer graphene electrodes has also been reported by Chen et al.[86] which is capable of sustaining a tensile strain of up to 40% with transparency up to 60% with hundreds of stable stretching-releasing cycles.

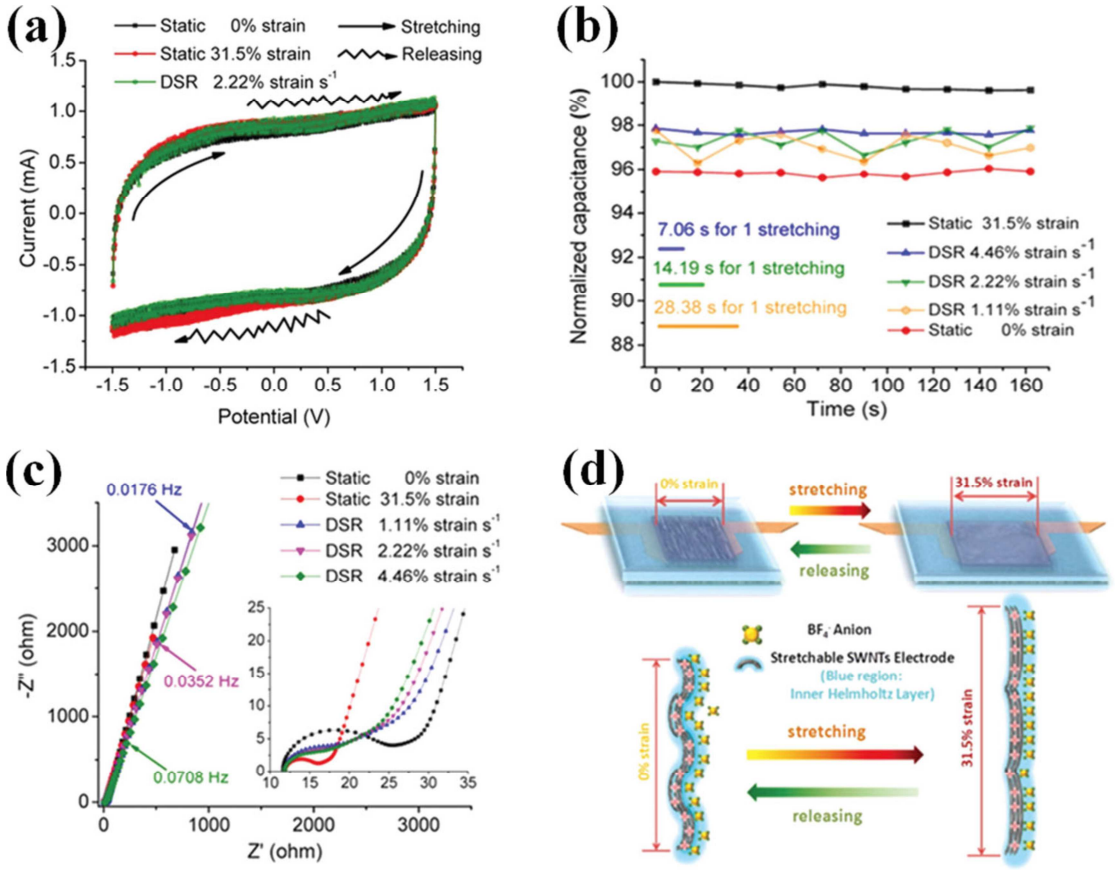

Figure 1.4 (**a**) CV curve under the DSR mode at a rate of 2.22% strain·s^{-1}, demonstrating the green CV curve shifts between the two static CV curves. (**b**) Comparison of the normalized capacitance at different strain rates. (**c**) Nyquist plots of the stretchable SC at different strains and under various strain rates applied (inset: high-frequency region). (**d**) Schematic of the stretchable SC at different strains showing changing electrode/electrolyte interface due to stretching/releasing.

1.4 Lithium-ion Batteries

Since the first introduction in 1991, LIBs have been attracting more and more attention and extensively studied as a power source for portable electronics, electric vehicles, and large-scale stationary energy storage systems, owing to its high energy density, excellent stability, and high operating voltage.[90-92] LIB involves a reversible

insertion or extraction of lithium ions, which called the guest species, into or out of a host matrix which is a suitable lithium insertion compound, during the charge or discharge process. Until now, the second-generation LIBs have been extensively developed. Many electrode materials were investigated including the spinels, e.g. lithium manganese oxide (LMO), as cathode,[93] $Li_4Ti_5O_{12}$ (LTO) as the anode;[94] and a big family of metal oxides as cathodes or anodes with the advantages of low cost, abundance and environmental friendliness.[95-97]

1.4.1 Principle

A typical commercial LIB consists of a graphite anode, a lithium cobalt oxide ($LiCoO_2$) cathode, and a separator immersed in a liquid organic electrolyte (e.g. 1 M $LiPF_6$ in 1:1 of diethyl carbonate (DEC) and ethylene carbonate (EC) by volume). The schematic in Figure 1.2c illustrates the principle of LIBs involving the electrochemical reactions at both cathode and anode in Equations 1.6 and 1.7:

$$LiCoO_2 \underset{Discharge}{\overset{Charge}{\rightleftharpoons}} Li_{(1-x)}CoO_2 + xLi^+ + xe^- \qquad \text{Cathode} \qquad (1.6)$$

$$6C + xLi^+ \underset{Discharge}{\overset{Charge}{\rightleftharpoons}} Li_xC_6 \qquad \text{Anode} \qquad (1.7)$$

The cathode and anode are the source and sink of the lithium ions, respectively. The electrolyte balances the charge transfer by promoting the ionic transport in the inner cell, which is separated from the electronic transport happening in the external circuit via electron flow for power supply. Throughout the charging process, lithium ions migrate from the $LiCoO_2$ (cathode) through the electrolyte and are intercalated into the graphite to form Li_xC_6 (anode). While during the discharging process, the reverse movement of lithium ions happens: lithium ions are extracted from the Li_xC_6 and intercalated into the $LiCoO_2$.

The open circuit voltage U_{ocv} of a LIB is determinded by the difference in the lithium ion chemical potential between the cathode ($\mu_{cathode}$) and the anode (μ_{anode}) in Nernst Equation, which can be described as Equation 1.8:

$$U_{ocv} = \frac{\mu_{cathode} - \mu_{anode}}{F} \quad (1.8)$$

where F is the Faraday constant. The U_{ocv} is given by the Gibbs free energy involved in both the electron transfer and the lithium ion transfer. It is further governed by the crystal structure for the lithium ions to be inserted and extracted.

1.4.2 Electrochemical tests and calculations

The assembly of the cells involves two configurations for LIBs, i.e., half-cell or full-cell configurations. To analyze the battery performance, it is important to have basic knowledge of the electrochemical characteristics of the cathode or anode such as specific capacity and rate capability measured by employing a series of electrochemical testing.

Coin cell in half-cell configuration is typically assembled by a hydraulic machine with three primary components: two electrodes and one separator saturated in the electrolyte. The working electrode could be either a cathode or an anode material as a positive electrode. Li metal is the standard reference/counter material as negative electrodes in the half cell to evaluate the lithium ion insertion/extraction capability of the working electrode material. The maximum capacity of any particular cathode or anode materials that generate and store lithium ions is usually determined in half cells under the GCD test discussed in Section 1.3.5. The exact amount of lithium ions that a cathode material generates should match the amount of an anode material that can actually store. For instance, assuming that the cathode material of $LiCoO_2$ will deliver a specific capacity of 140 mAh g^{-1} in the half-cell configuration, which means 1 g

$LiCoO_2$ can generate lithium ions about a maximum of 140 mA of capacity in 60 mins. Different from the testing in SC, to better implement the GCD testing in LIB, it is convenient to take the current density as a reference rate denoted by 1C that enables one-time of charge or discharge completed within 1 h when it is applied to any material, assuming with the theoretical specific capacity. For example, the theoretical specific capacity for graphite is 372 mAh g^{-1},[98] so 1 C rate is 372 mA g^{-1} for the GCD test with graphite.

GCD is also the most common method to evaluate other electrochemical performance such as rate capability and cycling stability of LIBs at various current densities. The rate performance of LIB is tested by carrying out GCD tests at various current rates such as 0.1 C, 0.2 C, 0.5 C, 1 C, 2 C, 10 C, and even higher current rates. The rate capability determines the specific capacity of the batteries at various specific rates, at which they are charged and discharged. The LIB as power sources with better rate capability signifies a faster charging/discharging. Apart from GCD, there are two other major electrochemical methods similar to the tests in SCs: CV and EIS, which are also relied on to evaluate the electrochemical performance of LIB. CV and EIS are conducted on a multi-channel potentiostat with necessary accessories such as coin cells or test cells.

In the full-cell configuration, anode materials are with relatively lower potentials versus Li^+ /Li while cathode materials are with higher potentials. Commercial batteries are in the full-cell configuration. The Li-containing cathode material is able to generate lithium ions to insert into the anode material via electrolyte upon charging. The reverse process occurs in the discharge. In Chapter 5, the anode

material was charge-discharged several cycles before the assembly of the full cell to eliminate the first capacity loss.

1.4.3 Stretchable lithium-ion batteries

LIB is an ideal candidate for stretchable storage systems for the applications of wearable devices, bendable displays, and implantable medical devices. "Wave configuration" is the well-known representative strategy for stretchable SCs as discussed in section 1.3.6. The key advantage of this strategy is the deposition of rigid materials on a prestrained elastic substrate, and the subsequent release of the pre-strain can make any thin layer of rigid materials stretchable. However, the majority of the reports has focused on the stretchable SCs by using this strategy due to relatively less difficulty in fabrication and operation in stretchable SC systems. On the contrary, there is very few work involving stretchable LIBs, especially the CNT-based stretchable LIBs. Very recently, wavy stretchable electrodes with a gum-like stretchability were reported by Peng et al.[99] A CNT sheet, a blend of active material (LMO/CNT powder), and another CNT sheet were attached on the LMO/CNT to generate the sandwich structure. Un-curing PDMS fluid was then introduced onto the sandwich structure as the binder. Finally, curing PDMS and releasing the pre-strain were carried out to make the wavy electrode. The fabricated wavy electrodes with the sandwich configuration demonstrated high stretchability and almost unchanged capacity after 500 stretching cycles. Another advance in stretchable LIBs has been very recently made by Liu et al.[100] They used the 3D porous sponge-like PDMS scaffolds to construct pore structure for stretchable LIBs. Infiltration of PDMS into sugar and removal of sugar cube by dissolution in water enable the simple production of 3D porous PDMS scaffolds. Active materials such as slurry LTO anode and lithium

iron phosphate ($LiFePO_4$) cathode were pasted on the PDMS scaffolds. The electrodes showed high stretchability of 80% and excellent capacity retention of 82% over 500 cycles. Although the excellent performances obviously originated from the wavy structure, it should be noted that the introduction of the polymer binder is unavoidable to form the electrode which degrades the ion transport capability, inhibits the electrical conductivity, and leads to an obvious capacity loss. Similar to the wavy structure, the same challenge in textile design for stretchable LIBs also exists; i.e. there is no in-situ chemical bonding between the active material and scaffold,[101] especially for the textile structural configuration, which usually has an exceptional characteristic of stretchability. When the active materials, such as carbon grease, $LiFePO_4$, and LTO are directly pasted on textile as stretchable battery electrodes, a significant decrease in electric conductivity is always observed due to the gradual loss of contacts between the active materials and substrate during repeated mechanical stretching/releasing, hurting the performance of the stretchable LIBs.

Fabrication of integrated LIBs with high stretchability is also another effective way to reach system-level deformability. Roger et al. demonstrated a segmented design in the active electrode materials; with "self-similar" interconnect structures.[27] an array of 100 disks of electrode connected in parallel was covered by elastomer sheets. The highly system-level stretchable LIBs showed excellent electrochemical performances and mechanical properties with 300% strain and stable capacity density of ~1.1 mAh cm^{-2}. Origami and kirigami are also able to realize a high level of stretchability. Song et al.[102] demonstrated an origami LIB that can be highly deformed by folding and twisting. The LCO cathode and LTO anode electrodes were prepared by slurry coating on paper current collectors, and the packaging is aluminized

polyethylene. The origami LIB showed many identical parallelogram faces that were connected by “mountain” and “valley” creases, which could be almost fully compressible in one direction. However, the foldability of the origami LIBs is restricted and uneven surfaces could be introduced by repeatable folding. Hence, this group developed kirigami LIBs,[103] showing large stretchability higher than 150%. Conventional materials including graphite and LCO with slurry coating were applied. This kirigami LIB showed good and stable electrochemical performances at deformed status. Over 85% capacity retention over 100 cycles could be achieved under stretched states. For these system-level configurations for stretchable LIBs, the biggest challenge is that the effective areal specific capacity is still extremely low. How to balance the high areal coverages and high levels of stretchability is a very challenging work in this design. Besides, its fabrication process is relatively complex, leading to a high fabrication cost.

1.5 Research Motivation and Dissertation Scope

Diverse aspects of CNT films ranging from synthesis to its unique properties as well as the potential applications in energy storage devices including SCs and LIBs are discussed in the above sections.[105,106] It is believed that combining the free-standing binder-free CNT films, which possess a high electric conductivity, large specific surface area as well as stretchability with active electrode materials, will enable the fabrication of high-performance nanocomposite electrode materials for stretchable energy storage devices. This motivates us to focus on the study of CNT film-based nanocomposites for stretchable energy storage devices in this dissertation.

Previously, it was already demonstrated by our group that the pure CNT films are an excellent candidate material for stretchable EDLCs. Nevertheless, no reports

have been extended to the nanocomposites based on CNT films with pseudo-capacitive materials. In Chapter 2, manganese dioxide (MnO_2)/CNT nanocomposite is prepared by a facial room temperature synthesis method to assemble a dynamically stretchable pseudocapacitor (DSP). The excellent pseudo-capacitive stability of the DSP based on MnO_2/CNT electrode under both electrochemical charge-discharge cycles and mechanical stretching-releasing cycles is attributed to the bond between the MnO_2 nanoparticles and CNT. It is concluded based on detailed electrochemical analysis that the extremely small relaxation time constants explained fundamentally that repeated stretching and releasing at the applied strain rates would not affect the stable performance of stretchable pseudocapacitors.

Although DSPs were first successfully developed, increasing the mass loading of pseudo-capacitive materials while maintaining high electrochemical performance for stretchable pseudocapacitors remains a bottleneck and was very challenging. Therefore, in Chapter 3 we present a novel architectural design of stretchable electrodes with a high mass loading of pseudo-capacitive materials. Here we report an all-solid-state sandwich-like stretchable pseudocapacitor (SSP), which overcomes the limitation of maximum loading of active pseudo-capacitive materials and exhibits excellent structural and electrochemical stabilities, giving rise to outstanding cycling stability and rate capability.

Stretchable single-cell energy storage devices suffer from a relatively low operating voltage in aqueous electrolyte and thus a low energy density. In Chapter 4, we built an all-solid-state ASS using the wrinkled MnO_2/CNT film as a positive electrode and the wrinkled iron oxide (Fe_2O_3)/CNT composite film as a negative electrode in a neutral Na_2SO_4/polyvinyl alcohol (PVA) gel electrolyte. Due to the high

specific capacitance and excellent rate performance of both electrodes, as well as the synergistic effects of the two electrodes with an optimized potential window, the ASS exhibits superior electrochemical and mechanical performances. Experimental results and systematical analysis conclude that an optimized ASS can be reversibly cycled in the voltage window between 0 and 2 V, and shows a supreme energy density of 45.8 Wh kg^{-1}.

Besides the stretchable pseudocapacitors and stretchable asymmetric supercapacitors, the sufficiently stretchable LIB is yet underdeveloped, which is one of the biggest challenges preventing us from realizing fully deformable power sources. In Chapter 5, we report a low-temperature hydrothermal synthesis of a cathode material for stretchable lithium-ion battery by the in-situ growth of LMO nanocrystals in CNT film networks. The LMO/CNT film composite has demonstrated the chemical bonding between the LMO active materials and CNT scaffolds, which is the most important characteristic of the stretchable LIB electrodes. When coupled with a wrinkled manganese oxide (MnO_x)/CNT film anode, a binder-free, all-manganese-based stretchable full battery cell was assembled, which delivered a high average specific capacity of ~97 mAh g^{-1} and stabilized after over 300 cycles with an enormous strain of 100%. Furthermore, combining with other merits such as low cost, natural abundance and environmentally friendly, our all-manganese design is expected to accelerate the practical applications of stretchable LIBs for fully flexible and biomedical electronics.

In the last part of Chapter 6, some of the perspectives and opportunities in the areas of material synthesis and structural design facing the emerging stretchable energy storage devices field are also discussed.

REFERENCES

1 Bruce, P. G.; Freunberger, S. a.; Hardwick, L. J.; Tarascon, J.-M. Li–O_2 and Li–S Batteries with High Energy Storage. *Nat. Mater.* **2012**, *11*, 19–29.

2 Dunn, B.; Kamath, H.; Tarascon, J.-M. Electrical Energy Storage for the Grid: A Battery of Choices. *Sci.* **2011**, *334*, 928–935.

3 Chen, H.; Cong, T. N.; Yang, W.; Tan, C.; Li, Y.; Ding, Y. Progress in Electrical Energy Storage System: A Critical Review. *Prog. Nat. Sci.* **2009**, *19*, 291–312.

4 Kamat, P. V. Meeting the Clean Energy Demand: Nanostructure Architectures for Solar Energy Conversion. *Phys. Chem.* **2007**, *392*, 2834–2860.

5 Shove, E.; Walker, G. What Is Energy For? Social Practice and Energy Demand. *Theory, Cult. Soc.* **2014**, *31*, 41–58.

6 Chan, C.; Peng, H.; Liu, G.; McIlwrath, K.; Zhang, X.; Huggins, R.; Cui, Y. High-Performance Lithium Battery Anodes Using Silicon Nanowires. *Nat. Nanotechnol.* **2007**, *3*, 31–35.

7 Liu, C.; Li, F.; Ma, L.-P.; Cheng, H.-M. Advanced Materials for Energy Storage. *Adv. Mater.* **2010**, *22*, E28–62.

8 Wang, X.; Lu, X.; Liu, B.; Chen, D.; Tong, Y.; Shen, G. Flexible Energy-Storage Devices: Design Consideration and Recent Progress. *Adv. Mater.* **2014**, *26*, 4763–4782.

9 Yuan, C.; Wu, H. Bin; Xie, Y.; Lou, X. W. Mixed Transition-Metal Oxides: Design, Synthesis, and Energy-Related Applications. *Angew. Chemie - Int. Ed.* **2014**, *53*, 1488–1504.

10 Patrice, S.; Gogotsi, Y.; Dunn, B. Where do batteries end and supercapacitors begin? *Sci.* **2014**, *343*, 1210-1211.

11 Rogers, J. A.; Someya, T.; Huang, Y. Materials and Mechanics for Stretchable Electronics. *Sci.* **2010**, *327*, 1603–1607.

12 Sun, Y.; Choi, W. M.; Jiang, H.; Huang, Y. Y.; Rogers, J. a. Controlled Buckling of Semiconductor Nanoribbons for Stretchable Electronics. *Nat. Nanotechnol.* **2006**, *1*, 201–207.

13 Hammock, M. L.; Chortos, A.; Tee, B. C. K.; Tok, J. B. H.; Bao, Z. 25th Anniversary Article: The Evolution of Electronic Skin (E-Skin): A Brief History, Design Considerations, and Recent Progress. *Adv. Mater.* **2013**, *25*, 5997–6038.

14 Xie, K.; Wei, B. Materials and Structures for Stretchable Energy Storage and Conversion Devices. *Adv. Mater.* **2014**, *26*, 3592–3617.

15 Yan, C.; Lee, P. S. Stretchable Energy Storage and Conversion Devices. *Small* **2014**, *10*, 3443–3460.

16 Liu, W.; Song, M.-S.; Kong, B.; Cui, Y. Flexible and Stretchable Energy Storage: Recent Advances and Future Perspectives. *Adv. Mater.* **2016**, *1603436*.

17 Li, L.; Wu, Z.; Yuan, S.; Zhang, X.-B. B. Advances and Challenges for Flexible Energy Storage and Conversion Devices and Systems. *Energy Environ. Sci.* **2014**, *7*, 2101-2122.

18 Lee, S.-Y.; Choi, K.-H.; Choi, W.-S.; Kwon, Y. H.; Jung, H.-R.; Shin, H.-C.; Kim, J. Y. Progress in Flexible Energy Storage and Conversion Systems, with a Focus on Cable-Type Lithium-Ion Batteries. *Energy Environ. Sci.* **2013**, *6*, 2414-2423.

19 Hong, S.; Myung, S. Nanotube Electronics: A Flexible Approach to Mobility. *Nat. Nanotechnol.* **2007**, *2*, 207–208.

20 Sun, Y.; Rogers, J. A. Inorganic Semiconductors for Flexible Electronics. *Adv. Mater.* **2007**, *19*, 1897–1916.

21 Choi, C.; Lee, J. M.; Kim, S. H.; Kim, S. J.; Di, J.; Baughman, R. H. Twistable and Stretchable Sandwich Structured Fiber for Wearable Sensors and Supercapacitors. *Nano Lett.* **2016**, *16,* 7677–7684.

22 Xu, P.; Gu, T.; Cao, Z.; Wei, B.; Yu, J.; Li, F.; Byun, J.-H.; Lu, W.; Li, Q.; Chou, T.-W. Carbon Nanotube Fiber Based Stretchable Wire-Shaped Supercapacitors. *Adv. Energy Mater.* **2014**, *4*, 1300759.

23 Yang, Z.; Deng, J.; Chen, X.; Ren, J.; Peng, H. A Highly Stretchable, Fiber-Shaped Supercapacitor. *Angew. Chemie - Int. Ed.* **2013**, *52*, 13453–13457.

24 Padaki, N. V. Knitted Preforms for Composite Applications. *J. Ind. Text.* **2006**, *35*, 295–321.

25 Yue, B.; Wang, C.; Ding, X.; Wallace, G. G. Polypyrrole Coated Nylon Lycra Fabric as Stretchable Electrode for Supercapacitor Applications. *Electrochim. Acta* **2012**, *68*, 18–24.

26 Matsuhisa, N.; Kaltenbrunner, M.; Yokota, T.; Jinno, H.; Kuribara, K.; Sekitani, T.; Someya, T. Printable Elastic Conductors with a High Conductivity for Electronic Textile Applications. *Nat. Commun.* **2015**, *6*, 7461.

27 Xu, S.; Zhang, Y.; Cho, J.; Lee, J.; Huang, X.; Jia, L.; Fan, J. a; Su, Y.; Su, J.; Zhang, H.; *et al.* Stretchable Batteries with Self-Similar Serpentine Interconnects and Integrated Wireless Recharging Systems. *Nat. Commun.* **2013**, *4*, 1543.

28 Brosteaux, D.; Axisa, F.; Gonzalez, M.; Vanfleteren, J. Design and Fabrication of Elastic Interconnections for Stretchable Electronic Circuits. *IEEE Electron Device Lett.* **2007**, *28*, 552–554.

29 Gu, T.; Wei, B. Fast and Stable Redox Reaction of MnO_2/CNT Hybrid Electrodes for Dynamically Stretchable Pseudocapacitors. *Nanoscale* **2015**, *7*, 11626–11632.

30 Gu, T., Wei. B. High-Performance All-Solid-State Asymmetric Stretchable Supercapacitors Based on Wrinkled MnO_2/CNT and Fe_2O_3/CNT Macrofilms. *J. Mater. Chem. A* **2016**, *327*, 1603–1607.

31 Gu, T.; Wei, B. All-Solid-State Stretchable Pseudocapacitors Enabled by Carbon Nanotube Film-Capped Sandwich-like Electrodes. *ACS Appl. Mater. Interfaces* **2016**, *8*, 25243–25250.

32 Che, G.; Lakshmi, B. B.; Fisher, E. R.; Martin, C. R. Carbon Nanotubule Membranes for Electrochemical Energy Storage and Production. *Nature* **1998**, *393*, 346–349.

33 Li, X.; Wei, B. Supercapacitors Based on Nanostructured Carbon. *Nano Energy* **2013**, *2*, 159–173.

34 Masarapu, C.; Wei, B. Direct Growth of Aligned Multiwalled Carbon Nanotubes on Treated Stainless Steel Substrates. *Langmuir* **2007**, *23*, 9046–9049.

35 Subramanian, V.; Zhu, H.; Wei, B. Synthesis and Electrochemical Characterizations of Amorphous Manganese Oxide and Single Walled Carbon Nanotube Composites as Supercapacitor Electrode Materials. *Electrochem. commun.* **2006**, *8*, 827–832.

36 Jung, N.; Kwon, S.; Lee, D.; Yoon, D. M.; Park, Y. M.; Benayad, A.; Choi, J. Y.; Park, J. S. Synthesis of Chemically Bonded Graphene/carbon Nanotube Composites and Their Application in Large Volumetric Capacitance Supercapacitors. *Adv. Mater.* **2013**, *25*, 6854–6858.

37 Dai, C.; Chien, P.; Lin, J.; Chou, S.; Wu, W.; Li, P.; Wu, K.; Lin, T. Hierarchically Structured Ni_3S_2/Carbon Nanotube Composites as High Performance Cathode Materials for Asymmetric Supercapacitors. *ACS Appl. Mater. Interfaces* **2013**, *5*, 12168–12174.

38 Habisreutinger, S. N.; Leijtens, T.; Eperon, G. E.; Stranks, S. D.; Nicholas, R. J.; Snaith, H. J. Carbon Nanotube/polymer Composites as a Highly Stable Hole Collection Layer in Perovskite Solar Cells. *Nano Lett.* **2014**, *14*, 5561–5568.

39 Subramanian, V.; Luo, C.; Stephan, A. M.; Nahm, K. S.; Thomas, S.; Wei, B. Supercapacitors from Activated Carbon Derived from Banana Fibers. *J. Phys. Chem. C* **2007**, *111*, 7527–7531.

40 Zhu, H.; Wei, B. Direct Fabrication of Single-Walled Carbon Nanotube Macro-Films on Flexible Substrates. *Chem. Commun.* **2007**, 3042–3044.

41 De Volder, M. F. L.; Tawfick, S. H.; Baughman, R. H.; Hart, A. J. Carbon Nanotubes: Present and Future Commercial Applications. *Sci.***2013**, *339*, 535–539.

42 Liao, J.; Tan, M. J. Mixing of Carbon Nanotubes (CNTs) and Aluminum Powder for Powder Metallurgy Use. *Powder Technol.* **2011**, *208*, 42–48.

43 He, C.; Zhao, N.; Shi, C.; Du, X.; Li, J.; Li, H.; Cui, Q. An Approach to Obtaining Homogeneously Dispersed Carbon Nanotubes in Al Powders for Preparing Reinforced Al-Matrix Composites. *Adv. Mater.* **2007**, *19*, 1128–1132.

44 Cao, Z.; Wei, B. A Perspective: Carbon Nanotube Macro-Films for Energy Storage. *Energy Environ. Sci.* **2013**, *6*, 3183–3201.

45 González, A.; Goikolea, E.; Barrena, J. A.; Mysyk, R. Review on Supercapacitors: Technologies and Materials. *Renew. Sustain. Energy Rev.* **2016**, *58*, 1189–1206.

46 Zhong, C.; Deng, Y.; Hu, W.; Qiao, J.; Zhang, L.; Zhang, J. A Review of Electrolyte Materials and Compositions for Electrochemical Supercapacitors. *Chem. Soc. Rev.* **2015**, *44*, 7484–7539.

47 Zhang, L. L.; Zhou, R.; Zhao, X. S. Carbon-Based Materials as Supercapacitor Electrodes. *J. Mater. Chem.* **2009**, *38*, 2520–2531.

48 Pandolfo, A. G.; Hollenkamp, A. F. Carbon Properties and Their Role in Supercapacitors. *J. Power Sources* **2006**, *157*, 11–27.

49 Wang, H.; Casalongue, H. S.; Liang, Y.; Dai, H. $Ni(OH)_2$ Nanoplates Grown on Graphene as Advanced Electrochemical Pseudocapacitor Materials. *J. Am. Chem. Soc.* **2010**, *132*, 7472–7477.

50 Fan, Z.; Yan, J.; Wei, T.; Zhi, L.; Ning, G.; Li, T.; Wei, F. Asymmetric Supercapacitors Based on Graphene/MnO_2 and Activated Carbon Nanofiber Electrodes with High Power and Energy Density. *Adv. Funct. Mater.* **2011**, *21*, 2366–2375.

51 Vivekchand, S. R. C.; Rout, C. S.; Subrahmanyam, K. S.; Govindaraj, A.; Rao, C. N. R. Graphene-Based Electrochemical Supercapacitors. *J. Chem. Sci.* **2008**, *120*, 9–13.

52 Athouël, L.; Moser, F.; Dugas, R.; Crosnier, O.; Bélanger, D.; Brousse, T. Variation of the MnO_2 Birnessite Structure upon Charge/discharge in an Electrochemical Supercapacitor Electrode in Aqueous Na_2SO_4 Electrolyte. *J. Phys. Chem. C* **2008**, *112*, 7270–7277.

53 Xu, B.; Chen, Y.; Wei, G.; Cao, G.; Zhang, H.; Yang, Y. Activated Carbon with High Capacitance Prepared by NaOH Activation for Supercapacitors. *Mater. Chem. Phys.* **2010**, *124*, 504–509.

54 Hung, K.; Masarapu, C.; Ko, T.; Wei, B. Wide-Temperature Range Operation Supercapacitors from Nanostructured Activated Carbon Fabric. *J. Power Sources* **2009**, *193*, 944–949.

55 Balducci, A.; Bardi, U.; Caporali, S.; Mastragostino, M.; Soavi, F. Ionic Liquids for Hybrid Supercapacitors. *Electrochem. commun.* **2004**, *6*, 566–570.

56 Balducci, A.; Dugas, R.; Taberna, P. L.; Simon, P.; Plée, D.; Mastragostino, M.; Passerini, S. High Temperature Carbon-Carbon Supercapacitor Using Ionic Liquid as Electrolyte. *J. Power Sources* **2007**, *165*, 922–927.

57 Frackowiak, E.; Lota, G.; Pernak, J. Room-Temperature Phosphonium Ionic Liquids for Supercapacitor Application. *Appl. Phys. Lett.* **2005**, *86*, 1–3.

58 Zhi, M.; Xiang, C.; Li, J.; Li, M.; Wu, N. Nanostructured Carbon-Metal Oxide Composite Electrodes for Supercapacitors: A Review. *Nanoscale* **2013**, *5*, 72–88.

59 Brezesinski, T.; Wang, J.; Tolbert, S. H.; Dunn, B. Ordered Mesoporous Alpha-MoO_3 with Iso-Oriented Nanocrystalline Walls for Thin-Film Pseudocapacitors. *Nat. Mater.* **2010**, *9*, 146–151.

60 Xia, X. H.; Tu, J. P.; Wang, X. L.; Gu, C. D.; Zhao, X. B. Hierarchically Porous NiO Film Grown by Chemical Bath Deposition via a Colloidal Crystal Template as an Electrochemical Pseudocapacitor Material. *J. Mater. Chem.* **2011**, *21*, 671–679.

61 Xiao, J.; Wan, L.; Yang, S.; Xiao, F.; Wang, S. Design Hierarchical Electrodes with Highly Conductive $NiCo_2S_4$ Nanotube Arrays Grown on Carbon Fiber Paper for High-Performance Pseudocapacitors. *Nano Lett.* **2014**, *14*, 831–838.

62 Xia, X. H.; Tu, J. P.; Wang, X. L.; Gu, C. D.; Zhao, X. B. Mesoporous Co_3O_4 Monolayer Hollow-Sphere Array as Electrochemical Pseudocapacitor Material. *Chem Commun* **2011**, *47*, 5786–5788.

63 Wu, Z. S.; Wang, D. W.; Ren, W.; Zhao, J.; Zhou, G.; Li, F.; Cheng, H. M. Anchoring Hydrous RuO_2 on Graphene Sheets for High-Performance Electrochemical Capacitors. *Adv. Funct. Mater.* **2010**, *20*, 3595–3602.

64 Bélanger, D.; Brousse, T.; Long, J. W. Manganese Oxides: Battery Materials Make the Leap to Electrochemical Capacitors. *Electrochem. Soc. Interface* **2008**, *17*, 49–52.

65 Xia, X.; Tu, J.; Mai, Y.; Wang, X.; Gu, C.; Zhao, X. Self-Supported Hydrothermal Synthesized Hollow Co_3O_4 Nanowire Arrays with High Supercapacitor Capacitance. *J. Mater. Chem.* **2011**, *21*, 9319–9325.

66 Ghosh, A.; Ra, E. J.; Jin, M.; Jeong, H. K.; Kim, T. H.; Biswas, C.; Lee, Y. H. High Pseudocapacitance from Ultrathin V_2O_5 Films Electrodeposited on Self-Standing Carbon-Nanofiber Paper. *Adv. Funct. Mater.* **2011**, *21*, 2541–2547.

67 Yan, J.; Fan, Z.; Sun, W.; Ning, G.; Wei, T.; Zhang, Q.; Zhang, R.; Zhi, L.; Wei, F. Advanced Asymmetric Supercapacitors Based on $Ni(OH)_2$/graphene and Porous Graphene Electrodes with High Energy Density. *Adv. Funct. Mater.* **2012**, *22*, 2632–2641.

68 Yang, P.; Ding, Y.; Lin, Z.; Chen, Z.; Li, Y.; Qiang, P.; Ebrahimi, M.; Mai, W.; Wong, C. P.; Wang, Z. L. Low-Cost High-Performance Solid-State Asymmetric Supercapacitors Based on MnO_2 Nanowires and Fe_2O_3 Nanotubes. *Nano Lett.* **2014**, *14*, 731–736.

69 Transition-metal-oxide, B.; Carbon, N. S.; Chen, P.; Shen, G.; Shi, Y.; Chen, H.; Zhou, C. Preparation and Characterization of Flexible Asymmetric Supercapacitors. *ACS Nano* **2010**, *4*, 4403–4411.

70 Lu, X.; Yu, M.; Wang, G.; Zhai, T.; Xie, S.; Ling, Y.; Tong, Y.; Li, Y. H-TiO_2@MnO_2//H-TiO_2@C Core-Shell Nanowires for High Performance and Flexible Asymmetric Supercapacitors. *Adv. Mater.* **2013**, *25*, 267–272.

71 Zhang, J.; Jiang, J.; Li, H.; Zhao, X. S. A High-Performance Asymmetric Supercapacitor Fabricated with Graphene-Based Electrodes. *Energy Environ. Sci.* **2011**, *4*, 4009.

72 Qu, Q.; Zhang, P.; Wang, B.; Chen, Y.; Tian, S.; Wu, Y.; Holze, R. Electrochemical Performance of MnO_2 Nanorods in Neutral Aqueous Electrolytes as a Cathode for Asymmetric Supercapacitors. *J. Phys. Chem. C* **2009**, *113*, 14020–14027.

73 Khomenko, V.; Raymundo-Piñero, E.; Frackowiak, E.; Béguin, F. High-Voltage Asymmetric Supercapacitors Operating in Aqueous Electrolyte. *Appl. Phys. A Mater. Sci. Process.* **2006**, *82*, 567–573.

74 An, K. H.; Jeon, K. K.; Heo, J. K.; Lim, S. C.; Bae, D. J.; Lee, Y. H. High-Capacitance Supercapacitor Using a Nanocomposite Electrode of Single-Walled Carbon Nanotube and Polypyrrole. *J. Electrochem. Soc.* **2002**, *149*, A1058-A1062.

75 Chou, S. L.; Wang, J. Z.; Chew, S. Y.; Liu, H. K.; Dou, S. X. Electrodeposition of MnO_2 Nanowires on Carbon Nanotube Paper as Free-Standing, Flexible Electrode for Supercapacitors. *Electrochem. commun.* **2008**, *10*, 1724–1727.

76 Pushparaj, V. L.; Shaijumon, M. M.; Kumar, A.; Murugesan, S.; Ci, L.; Vajtai, R.; Linhardt, R. J.; Nalamasu, O.; Ajayan, P. M. Flexible Energy Storage Devices Based on Nanocomposite Paper. *Proc. Natl. Acad. Sci. U. S. A.* **2007**, *104*, 13574–13577.

77 Jost, K.; Perez, C. R.; McDonough, J. K.; Presser, V.; Heon, M.; Dion, G.; Gogotsi, Y. Carbon Coated Textiles for Flexible Energy Storage. *Energy Environ. Sci.* **2011**, *4*, 5060-5067.

78 Zheng, Y.; He, Z.; Gao, Y.; Liu, J. Direct Desktop Printed-Circuits-on-Paper Flexible Electronics. *Sci. Rep.* **2013**, *3*, 1786.

79 Yu, C.; Masarapu, C.; Rong, J.; Wei, B.; Jiang, H. Stretchable Supercapacitors Based on Buckled Single-Walled Carbon-Nanotube Macrofilms. *Adv. Mater.* **2009**, *21*, 4793–4797.

80 Li, X.; Gu, T.; Wei, B. Dynamic and Galvanic Stability of Stretchable Supercapacitors. *Nano Lett.* **2012**, *12*, 6366–6371.

81 Yu, M.; Zhang, Y.; Zeng, Y.; Balogun, M. S.; Mai, K.; Zhang, Z.; Lu, X.; Tong, Y. Water Surface Assisted Synthesis of Large-Scale Carbon Nanotube Film for High-Performance and Stretchable Supercapacitors. *Adv. Mater.* **2014**, *26*, 4724–4729.

82 Hu, L.; Pasta, M.; Mantia, F. La; Cui, L.; Jeong, S.; Deshazer, H. D.; Choi, J. W.; Han, S. M.; Cui, Y. Stretchable, Porous, and Conductive Energy Textiles. *Nano Lett.* **2010**, *10*, 708–714.

83 Pasta, M.; la Mantia, F.; Hu, L.; Deshazer, H. D.; Cui, Y. Aqueous Supercapacitors on Conductive Cotton. *Nano Res.* **2010**, *3*, 452–458.

84 Chen, T.; Peng, H.; Durstock, M.; Dai, L. High-Performance Transparent and Stretchable All-Solid Supercapacitors Based on Highly Aligned Carbon Nanotube Sheets. *Sci. Rep.* **2014**, *4*, 3612.

85 Xu, P.; Wei, B.; Cao, Z.; Zheng, J.; Gong, K.; Li, F.; Yu, J.; Li, Q.; Lu, W.; Byun, J.-H.; Kim, B.-S.; Yan, Y.; Chou, T.-W. Stretchable Wire-Shaped Asymmetric Supercapacitors Based on Pristine and MnO_2 Coated Carbon Nanotube Fibers. *ACS Nano* **2015**, *9*, 6088–6096.

86 Chen, T.; Xue, Y.; Roy, A. K.; Dai, L. Transparent and Stretchable High-Performance Supercapacitors Based on Wrinkled Graphene Electrodes. *ACS Nano* **2014**, *8*, 1039–1046.

87 Xu, P.; Kang, J.; Choi, J. B.; Suhr, J.; Yu, J.; Li, F.; Byun, J. H.; Kim, B. S.; Chou, T. W. Laminated Ultrathin Chemical Vapor Deposition Graphene Films Based Stretchable and Transparent High-Rate Supercapacitor. *ACS Nano* **2014**, *8*, 9437–9445.

88 Zang, X.; Zhu, M.; Li, X.; Li, X.; Zhen, Z.; Lao, J.; Wang, K.; Kang, F.; Wei, B.; Zhu, H. Dynamically Stretchable Supercapacitors Based on Graphene Woven Fabric Electrodes. *Nano Energy* **2015**, *15*, 83–91.

89 Li, F.; Chen, J.; Wang, X.; Xue, M.; Chen, G. F. Stretchable Supercapacitor with Adjustable Volumetric Capacitance Based on 3D Interdigital Electrodes. *Adv. Funct. Mater.* **2015**, *25*, 4601–4606.

90 Armand, M.; Tarascon, J.-M. Building Better Batteries. *Nature* **2008**, *451*, 652–657.

91 Scrosati, B. Recent Advances in Lithium Ion Battery Materials. *Electrochim. Acta* **2000**, *45*, 2461–2466.

92 Lu, L.; Han, X.; Li, J.; Hua, J.; Ouyang, M. A Review on the Key Issues for Lithium-Ion Battery Management in Electric Vehicles. *J. Power Sources* **2013**, *226*, 272–288.

93 Kim, D. K.; Muralidharan, P.; Lee, H.-W.; Ruffo, R.; Yang, Y.; Chan, C. K.; Peng, H.; Huggins, R. A.; Cui, Y. Spinel $LiMn_2O_4$ Nanorods as Lithium-Ion Battery Cathodes. *Nano Lett.* **2008**, *8*, 3948–3952.

94 Park, K. S.; Benayad, A.; Kang, D. J.; Doo, S. G. Nitridation-Driven Conductive $Li_4Ti_5O_{12}$ for Lithium Ion Batteries. *J. Am. Chem. Soc.* **2008**, *130*, 14930–14931.

95 Tarascon, J.; Poizot, P.; Laruelle, S.; Grugeon, S.; Dupont, L. Nano-Sized Transition-Metal Oxides as Negative-Electrode Materials for Lithium-Ion Batteries. *Nature* **2000**, *407*, 496–499.

96 Tarascon, J. M.; Armand, M. Issues and Challenges Facing Rechargeable Lithium Batteries. *Nature* **2001**, *414*, 359–367.

97 Taberna, P. L.; Mitra, S.; Poizot, P.; Simon, P.; Tarascon, J.-M. High Rate Capabilities Fe_3O_4-Based Cu Nano-Architectured Electrodes for Lithium-Ion Battery Applications. *Nat. Mater.* **2006**, *5*, 567–573.

98 Wang, H.; Yoshio, M. Carbon-Coated Natural Graphite Prepared by Thermal Vapor Decomposition Process, a Candidate Anode Material for Lithium-Ion Battery. *J. Power Sources* **2001**, *93*, 123–129.

99 Weng, W.; Sun, Q.; Zhang, Y.; He, S.; Wu, Q.; Deng, J.; Fang, X.; Guan, G.; Ren, J.; Peng, H. A Gum-like Lithium-Ion Battery Based on a Novel Arched Structure. *Adv. Mater.* **2015**, *27*, 1363–1369.

100 Liu, W.; Chen, Z.; Zhou, G.; Sun, Y.; Lee, H. R.; Liu, C.; Yao, H.; Bao, Z.; Cui, Y. 3D Porous Sponge-Inspired Electrode for Stretchable Lithium-Ion Batteries. *Adv. Mater.* **2016**, *28*, 3578–3583.

101 Hu, L.; La Mantia, F.; Wu, H.; Xie, X.; McDonough, J.; Pasta, M.; Cui, Y. Lithium-Ion Textile Batteries with Large Areal Mass Loading. *Adv. Energy Mater.* **2011**, *1*, 1012–1017.

102 Song, Z.; Ma, T.; Tang, R.; Cheng, Q.; Wang, X.; Krishnaraju, D.; Panat, R.; Chan, C. K.; Yu, H.; Jiang, H. Origami Lithium-Ion Batteries. *Nat. Commun.* **2014**, *5*, 1–6.

103 Song, Z.; Wang, X.; Lv, C.; An, Y.; Liang, M.; Ma, T.; He, D.; Zheng, Y.-J.; Huang, S.-Q.; Yu, H.; Jiang, H. Kirigami-Based Stretchable Lithium-Ion Batteries. *Sci. Rep.* **2015**, *5*, 10988.

104 Jost, K.; Dion, G.; Gogotsi, Y. Textile Energy Storage in Perspective. *J. Mater. Chem. A* **2014**, *2*, 10776–10787.

105 Yu, X.; Mahajan, B.; Shou, W.; Pan, H. Materials, Mechanics, and Patterning Techniques for Elastomer-Based Stretchable Conductors. *Micromachines* **2016**, *8*, 7.

106 Zhang, X.; Zhang, H.; Lin, Z.; Yu, M.; Lu, X.; Tong, Y. Recent Advances and Challenges of Stretchable Supercapacitors Based on Carbon Materials. *Sci. China Mater.* **2016**, *59*, 475–494.

Chapter 2

MANGANESE DIOXIDE/CARBON NANOTUBE HYBRID ELECTRODES FOR DYNAMICALLY STRETCHABLE PSEUDOCAPACITORS

2.1 Introduction

Fully flexible electronics can be bent, twisted and even stretched, and they represent the emerging direction towards next-generation wearable and bio-implantable electronic devices. Stretchable power sources are the key components for the fabrication of complete and independent stretchable electronic systems. To date, stretchable energy storage devices including stretchable EDLCs and stretchable LIBs have been reported to show excellent mechanical and electrochemical properties.[1-4] However, there is an urgent need to design and develop a stretchable power source with a higher power density than LIBs and a higher energy density than EDLCs. In light of this, stretchable pseudocapacitors are becoming indispensable.

Pseudocapacitors typically combine non-faradic electrostatic charge storage process from carbon based materials with redox reactions based on metal oxides and/or conductive polymers to achieve a higher specific capacitance and at the same time, to maintain their quick charge-discharge feature. A significant number of hybrid electrodes, such as CNT/RuO_2,[5] CNT/MnO_2,[6] graphene/MnO_2,[7] and graphene/ polyaniline (PANI)[8] have been investigated for flexible pseudocapacitors, however, fully stretchable pseudocapacitors are relatively underdeveloped. Hu *et al.*[9] deposited nanoparticles on the CNT films as stretchable electrodes for pseudocapacitors, but no electrochemical or mechanical testing under stretched states has been performed.

Another work on stretchable pseudocapacitors was reported based on polypyrrole (PPy) coated textiles.[10] PPy coated nylon "lycra" fabric delivered a much higher capacitance than the stretchable CNT-based electrodes,[1-3] but with poor cycling stability degraded to be less than 12.5% of the initial capacitance within 500 charge-discharge cycles. Since the conductive polymer was directly pasted on a textile as stretchable electrodes, a significant decrease in electric conductivity occurred during repeated mechanical stretching-releasing due to the gradual loss of electrical contacts between PPy and textile materials. It is therefore equivalently important to increase both the specific capacitance and the interface stability for stretchable pseudocapacitors. Unlike the stretchable EDLCs, which are based solely on buckled CNT film,[1-3] the strong bonding between the active materials (i.e. MnO_2 in this research) and CNT substrates in pseudocapacitors is another very critical requirement.

It is, therefore, crucial to explore building a stretchable pseudocapacitor system and to understand its fundamentals in order to meet the stringent requirements imposed by various applications of stretchable electronics. For example, it is unclear whether a redox reaction of a pseudocapacitor is fast enough to maintain its electrochemical stability under intensely and dynamically mechanical stretching and bending. How would the dynamic stretching/releasing affect the electrochemical properties of the stretchable pseudocapacitors since the charge storage mechanism of pseudocapacitors is completely different from that of EDLCs?

In this chapter, we demonstrated dynamically stretchable pseudocapacitors (DSPs) based on the MnO_2/CNT hybrid electrodes for the first time, with simultaneously monitoring mechanical and electrochemical behavior at different charge-discharge current densities and mechanical strain rates. Most importantly, the

redox reaction process of the typically pseudo-capacitive material MnO_2 has been found to be extremely fast owing to the strong bonded, inherently superior conductive and porous CNT films,[11] which facilitate charge transfer of the redox process of the stretchable pseudocapacitors. Because of this, the pseudo-capacitive stability would not be affected even by a dynamic mechanical deformation. These understanding would provide important guidelines for the design and development of highly stable and stretchable pseudocapacitor devices.

2.2 Experimental

2.2.1 DSP assembly

First, CNT films were prepared using a modified CVD method according to previously published work.[11] In brief, the precursor, a mixture of ferrocene and sulfur (atomic ratio Fe:S=1:10, both from Sigma-Aldrich), was heated to 1150 ^{o}C in a tube furnace with a mixed gas flow of Ar (1500 mL min^{-1}) and H_2 (150 mL min^{-1}). After a 75 min reaction, the as-obtained unpurified CNT films were transferred into a ceramic cubicle to be heat-treated at 430 ^{o}C in air for 30 min. When the furnace was cooled to room temperature, the CNT films were immersed in a concentrated HCl (37% by volume percent) solution for 72 h to remove the Fe_2O_3 oxidized from Fe catalysts during the heat treatment. The films were then rinsed with deionized water until the pH became neutral.

MnO_2/CNT hybrid film electrodes were then prepared by a modified precipitation method.[12] Briefly, the purified CNT film was immersed in ethanol, while 0.1 M potassium permanganate ($KMnO_4$) aqueous solution was drop-wisely added. A thin layer of nanostructured MnO_2 was deposited on the surface of the CNT bundles

with different precipitation time. The resulting MnO_2/CNT electrodes were rinsed excessively in deionized water and ethanol and finally dried at room temperature for 24 h.

The procedure to prepare the buckled MnO_2/CNT electrode is as follows: a custom-made two-way movable stage was utilized to pre-stretch a PDMS substrate; the pre-strained PDMS was subjected to UV light for 1 min to activate the surface functional groups to facilitate the strong bonding with the MnO_2/CNT film. Next, the freestanding MnO_2/CNT film was attached and secured to the PDMS substrate. Finally, the PDMS was released to its original length to form the "wavy" structure of the buckled MnO_2/CNT film. Elastomeric polyurethane separator was prepared by electrospinning.[2] Finally, these components were assembled and 1M $TEABF_4$/PC electrolyte was injected into the cell package. Stretchable cells were assembled in an argon-filled glove box (MBraun Unilab).

2.2.2 Characterizations

The morphology and structure of the MnO_2/CNT and CNT films were characterized using scanning electron microscopy (3 kV, JEOL JSM-7400F). The mass of active materials was acquired by using a micro/ultra-micro balance (Mettler Toledo XP6) with 0.001 mg accuracy. The GCD tests were carried out on four-channel battery testing equipment (Arbin Instrument, Ltd.). EIS was performed on a PARSTAT 2273 potentiostat/galvanostat (Princeton Applied Research) with 10 mV amplitude of AC signals from 100 kHz to 10 mHz. CV measurements were also obtained using the electrochemical workstation (Princeton Applied Research) in the scan range of -1.5 to 1.5 V. The electrochemical measurements were performed while the DSP was being stretched and released between 0 % (MnO_2/CNT film was buckled)

to 33.33% strain (MnO_2/CNT film was almost flattened). The strain rates were set at 1.5, 3, and 6 % s^{-1}, respectively. The dynamically stretching-releasing (DSR) test results reveal the real performance of the stretchable energy storage device.

2.2.3 Calculations

The specific capacitance of the MnO_2/CNT electrodes was calculated based on the total mass of the electrode and from the slope of the discharge curves. The energy and power densities were calculated by conducting GCD cycling with different constant current densities ranging from 100 mA g^{-1} to 100 A g^{-1}. The frequency dependence of the real and imaginary parts (C' and C'') of electrochemical capacitance was obtained from EIS measurements.

2.3 Results and Discussion

Figure 2.1a presents a typical SEM image of the pristine CNT films synthesized using a CVD method.[11] It can be seen that the SWNT bundles entangle each other to form porous structures consisting of mesopores and macropores, which provide superior electrical conductivity, large electrode/electrolyte interfaces and accessible pathways for electrolyte ions, thus facilitating the charge transfer by reducing the electronic and ionic diffusion resistances. Figure 2.1b illustrates the morphology of the MnO_2/CNT hybrid films as the stretchable pseudocapacitor electrodes. The MnO_2 nanoparticles are uniformly deposited on the surfaces of the CNT bundles to form a thin MnO_2 layer by employing a facile precipitation method.[12]

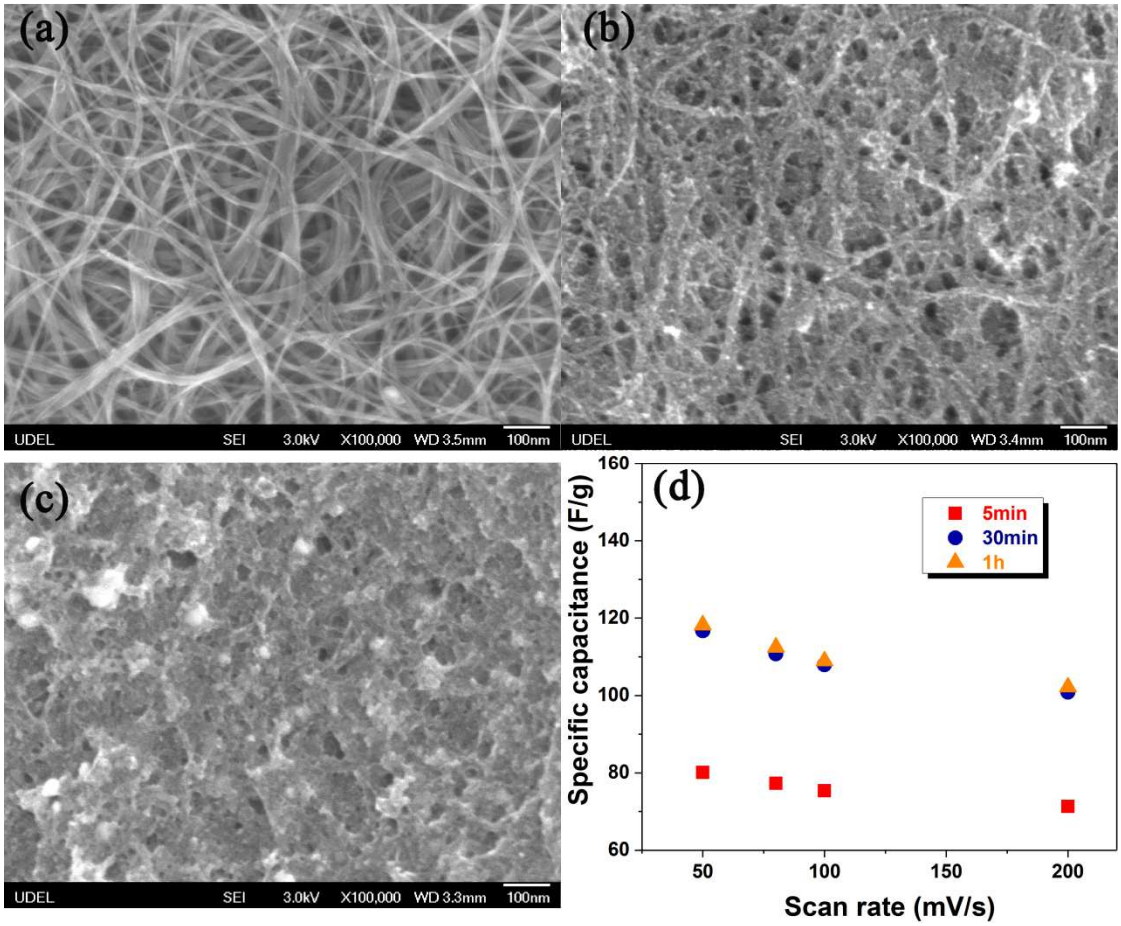

Figure 2.1 (**a**) Pristine CNT film as synthesized before coating MnO_2 layers. (**b**) Buckled MnO_2/CNT electrode as-synthesized with 30 min precipitation. (**c**) Buckled MnO_2/CNT electrode after 10000 charge-discharge cycles and 24300 stretching-releasing cycles simultaneously (**d**) Scan rate dependence of the specific capacitance based on the total mass of the MnO_2/CNT electrodes with respect to different precipitation times (5 min, 30 min, and 1 hour as examples).

After long GCD cycles (10000 cycles) under a dynamic mechanical stretching-releasing (24300 cycles) at 6% s^{-1} strain rate, the surface morphology was examined with SEM (Figure 2.1c). There are no noticeable detachments of the MnO_2 nanoparticles from the CNT bundles except some residues from the electrolyte salt, as

compared with those before the cycling test in Figure 2.1b. The MnO_2 thin layers retain similar morphologies after the long charge-discharge and stretching-releasing cycles, indicating very strong bonding between the MnO_2 nanoparticles and the CNT bundles. This behavior can be attributed to the interconnected porous and fabric-like structures of the CNT film as well as the surface functional groups introduced during the post-treatment of the CNT films that significantly enhance the bonding between the active material (MnO_2) and the CNT bundles. The merit of the thin MnO_2 layer grown on the CNT bundles is the diffusion path shortening of electrolyte ions during the fast charge-discharge processes, thus ensuring its full contribution to the pseudocapacitive performance, and significantly improving the specific capacitance of the DSPs. More important and significant for DSPs, however, the thin MnO_2 layer attached on the CNT surfaces can withstand intense stress during mechanical stretching and releasing, which is critical in determining whether the hybrid materials could be used as a good candidate for stretchable/flexible energy storage devices. As shown in Figure 2.1d, the optimized loading (20% MnO_2 mass ratio) in our experiments was obtained with 30 min precipitation. The DSPs were characterized using the optimized loading for all MnO_2/CNT electrode preparations in the following discussion.

Figure 2.2a illustrates the assembly of DSPs, including two PDMS packages embedded with two buckled MnO_2/CNT electrodes and an elastomeric separator. The as-fabricated pseudocapacitors are highly deformable and can be dynamically stretched and released without destroying their structural integrity (as a schematic in Figure 2.2b). The electrochemical characterization of the DSPs under GCD cycling was examined at a high current density of 10 A g^{-1}, exhibiting the high power

capability of the hybrid MnO_2/CNT electrodes. The symmetry profile of the charge and discharge curve also reveals the real capacitive characteristics of the DSPs and in particular, the inherently fast surface redox behavior of the MnO_2/CNT pseudo-capacitive materials. Although mechanical stretching-releasing modes are different for each state, the charge-discharge curves at different strain rates almost overlap, proving that the pseudocapacitive behavior is stable, reversible and independent of strain rate.

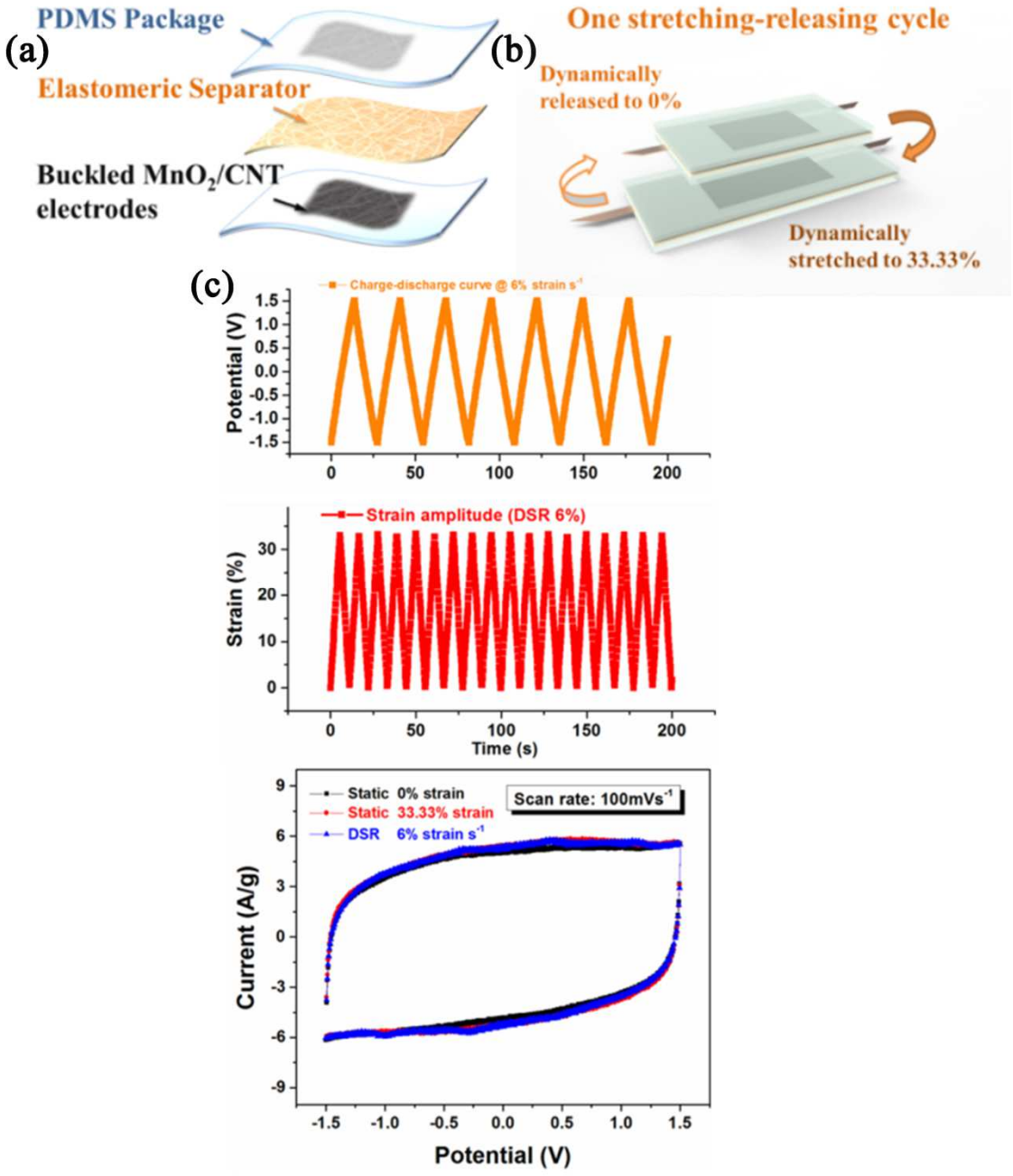
(a)
PDMS Package
Elastomeric Separator
Buckled MnO_2/CNT electrodes
(b)
One stretching-releasing cycle
Dynamically released to 0%
Dynamically stretched to 33.33%
(c)
Charge-discharge curve @ 6% strain s^{-1}
Potential (V)
Strain amplitude (DSR 6%)
Strain (%)
Time (s)
Static 0% strain
Static 33.33% strain
DSR 6% strain s^{-1}
Scan rate: 100mVs^{-1}
Current (A/g)
Potential (V)

Figure 2.2 (**a**) Schematic of the main components of the dynamically stretchable pseudocapacitors (DSPs). (**b**) Schematic of one mechanical stretching-releasing cycle: reversible dynamic stretching and releasing between 0 and 33.33% applied strains. (**c**) **Upper**: galvanostatic charge-discharge curve at the current density of 10 A g^{-1} under dynamic stretching-releasing (DSR) at a strain rate of 6% strain s^{-1}. **Middle**: the simultaneous dynamic mechanical strain amplitude variation between 0 and 33.33% strains at the 6% strain s^{-1}. **Bottom**: cyclic voltammograms (CVs) of the DSPs measured at a scan rate of 100 mV s^{-1}.

Dynamic CV is another important electrochemical-mechanical coupling test used to evaluate the electrochemical stability of the stretchable pseudocapacitors. CVs were tested under a DSR state and a statically stretched state with respect to the minimum strain (0%) and maximum strain (33.33%). As exemplarily shown in Figure 2.2c, under the DSR mode with a high strain rate of 6% strain s^{-1} (11.11 s for one mechanical stretching-releasing cycle, which is defined to be a dynamic stretching from 0 to 33.33% applied strain and then back to the 0% strain.), the reproducible and stable capacitive behavior of the DSPs at the scan rate of 100 mV s^{-1} reveals uncoupling effect between the mechanical strain and the electrochemical performance. The changes in electrochemical performance of the fabricated pseudocapacitor seem to be subtle under the dynamic mechanical stretching-releasing processes at the high strain rate of 6% strain s^{-1}. In addition, it is interesting to note that the CV curve under the DSR mode shifts between the static CV curves of the maximum (33.33% fixed static strain) and the minimum (0% fixed static strain). Accordingly, the pseudo-capacitance under different testing conditions also shows similar results; i.e. at various DSR strain rates (from 1.5 to 6% strain s^{-1}) and different scan rates (from 100 to 1000 mV s^{-1}), the CV curves for the DSR cases shift between the CV curves of 0 to 33.33% static strain (Figure 2.3). It is worthy of mentioning that the CV curves at the

extremely high scan rate of 1000 mV s^{-1} also maintain a typical rectangular shape, analogous to non-faradaic processes for stretchable EDLCs, indicating a highly reversible and fast faradaic reaction of MnO_2 due to the improved conductivity of the interconnected CNT film. These results further prove the excellent pseudo-capacitive stability of DSPs under stretching-releasing modes with high scan rates.

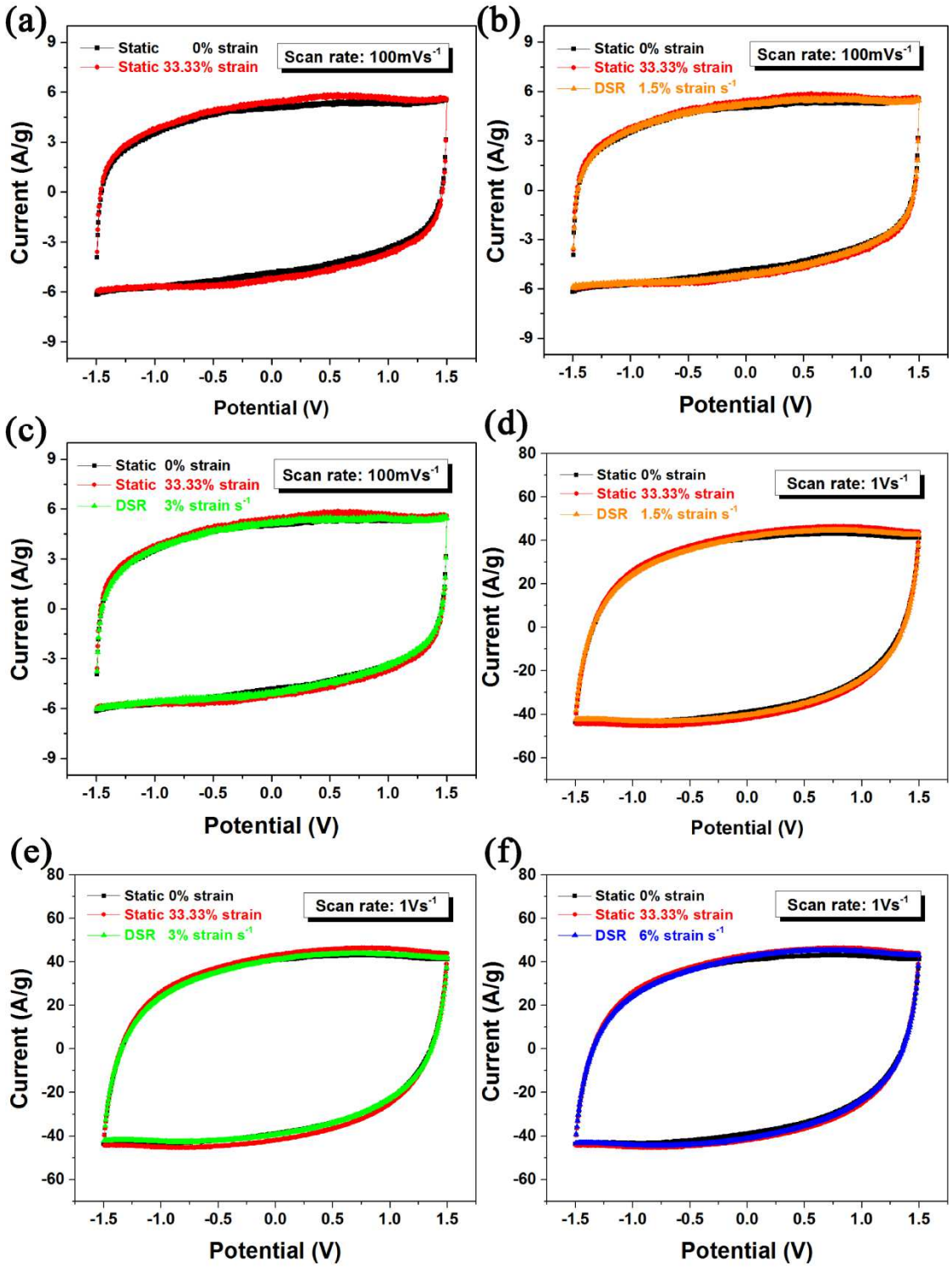
(a)
Static 0% strain
Static 33.33% strain
Scan rate: 100mVs-1
Current (A/g)
Potential (V)
(b)
Static 0% strain
Static 33.33% strain
DSR 1.5% strain s-1
Scan rate: 100mVs-1
Current (A/g)
Potential (V)
(c)
Static 0% strain
Static 33.33% strain
DSR 3% strain s-1
Scan rate: 100mVs-1
Current (A/g)
Potential (V)
(d)
Static 0% strain
Static 33.33% strain
DSR 1.5% strain s-1
Scan rate: 1Vs-1
Current (A/g)
Potential (V)
(e)
Static 0% strain
Static 33.33% strain
DSR 3% strain s-1
Scan rate: 1Vs-1
Current (A/g)
Potential (V)
(f)
Static 0% strain
Static 33.33% strain
DSR 6% strain s-1
Scan rate: 1Vs-1
Current (A/g)
Potential (V)

Figure 2.3 (**a**) CV curves under static 0% and 33.33% strain at a scan rate of 100 mV s^{-1}. The cell (under the static 33.33% strain) gives approximately 5% larger specific capacitance than that of the cell under the static 0% strain. (**b**) CV curves under the DSR mode at a strain rate of 1.5% strain s^{-1}, demonstrating that the orange CV curve shifts between the two statically stretched reference CV curves. (**c**) CV curves under the DSR mode at a strain rate of 3% strain s^{-1} which also shifts between the two reference CV curves. CV curve under the DSR mode at strain rate of (**d**) 1.5% strain s^{-1}, (**e**) 3% strain s^{-1} and (**f**) 6% strain s^{-1} at a high scan rate of 1000 mV s^{-1}

To explore the long cycle stability of the DSPs, 10000 GCD cycles were carried out at a current density of 10 A g^{-1}. As shown in Figure 2.4a, the capacitance retention with the 30-min-precipitation hybrid MnO_2/CNT electrodes has maintained up to 97.30%, 97.64% and 98.50% at the strain rates of 1.5, 3 and 6% strain s^{-1}, respectively. However, the capacitance retention for the hybrid MnO_2/CNT electrodes with 1-hour precipitation dropped to 76.15% and 59% after 10000 GCD cycles at the strain rates of 3% and 6%, respectively, a poor cycling stability compared to the 5 min and 30 min hybrid MnO_2/CNT electrodes (Figure 2.4b,c).

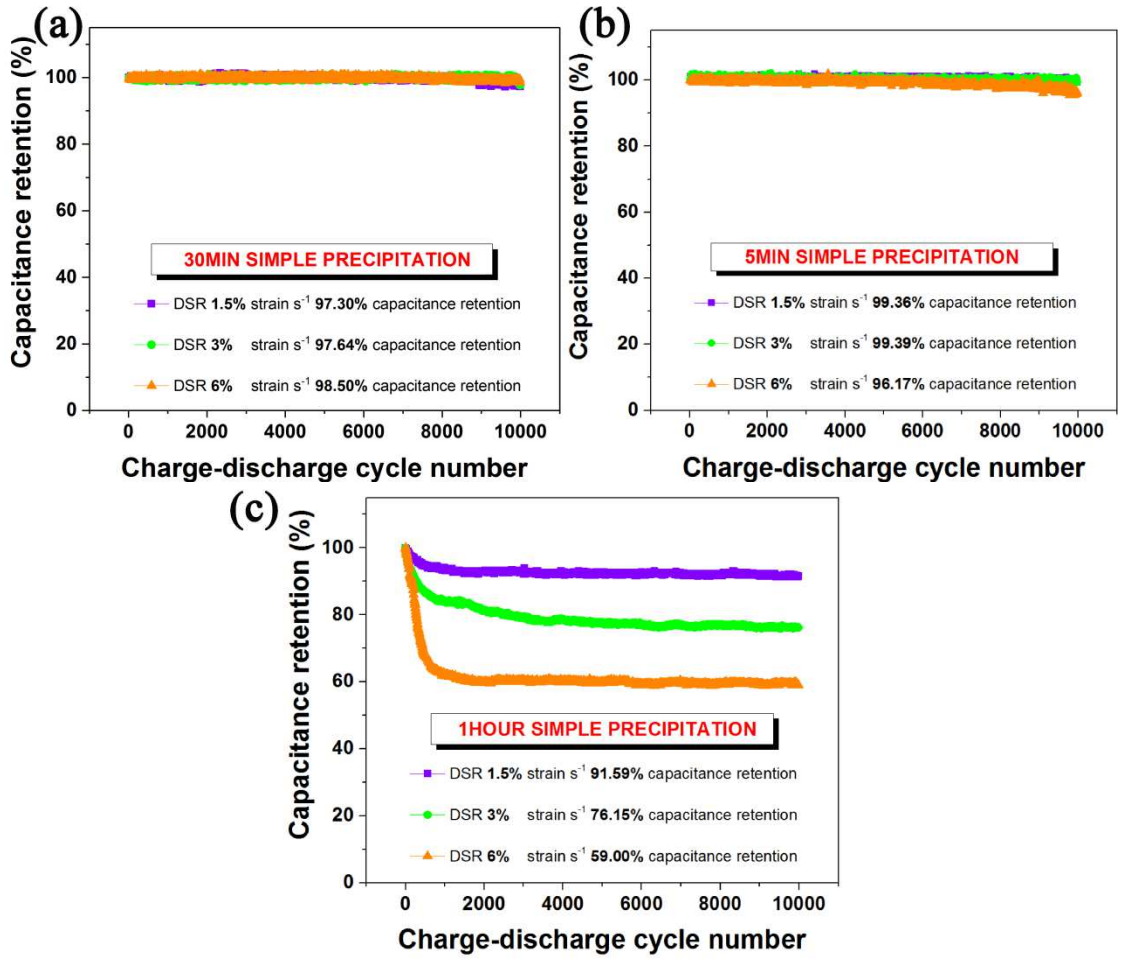

Figure 2.4 Simultaneously applied DSR cycling at the strain rates of 1.5, 3, and 6% strain s^{-1}, the DSP with 10000 electrochemical charge-discharge cycles with (**a**) 30 min (**b**) 5 min (**c**) 1-hour precipitation

The MnO_2 mass loading on CNT films can be just controlled by adjusting the precipitation time. The specific capacitance of the MnO_2/CNT based pseudocapacitors could be further increased by obtaining a thicker MnO_2 nanoparticle layer on the CNT film surface. The specific capacitance of the MnO_2/CNT electrode is about 150 F g^{-1} (based on the total mass of the MnO_2/CNT electrodes) and 750 F g^{-1} (based on the mass of MnO_2 only) achieved at 2 mV s^{-1}, which then drops to about 120 F g^{-1} and

600 F g^{-1} respectively at 50 mV s^{-1} (shown in Figure 2.5a). It is interesting to note that after 5 min precipitation, the specific capacitance of the hybrid film has been largely increased to 80 F g^{-1}, almost doubles the capacitance of the pure CNT-based EDLCs (~45 F g^{-1}) at 50 mV s^{-1}, indicating that this fabrication process for the MnO_2/CNT hybrid films has the potential for being scaled up. However, a thicker MnO_2 nanoparticle layer will not hold a tight bonding between MnO_2 and CNT and leads to irreversible detachment of the MnO_2 nanoparticle layer when a strong mechanical force is applied (Figure 2.5b-d). It further confirms that the 30-min-precipitation hybrid MnO_2/CNT electrodes provide the best overall performance and a thicker MnO_2 layer (1-hour-precipitation) would result in a bad contact and bonding with the CNT films.

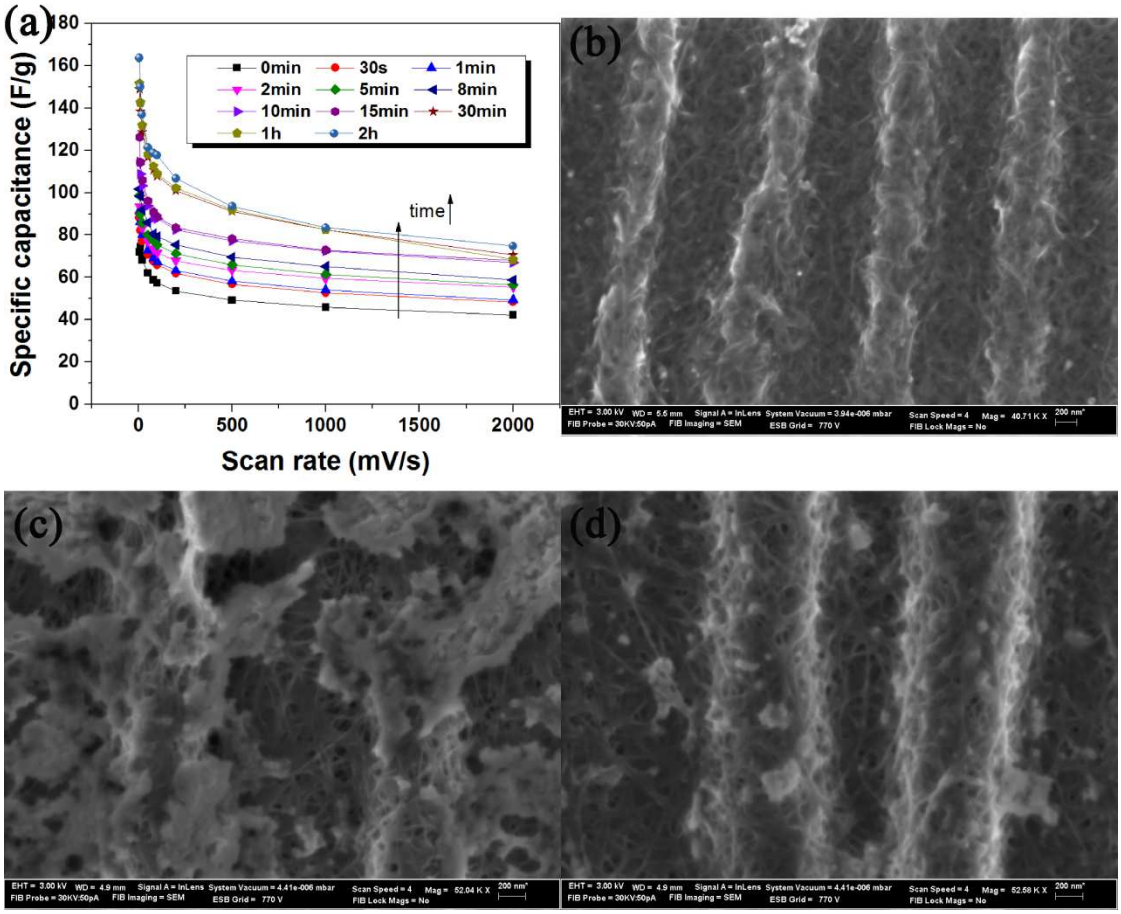

Figure 2.5 (**a**) Comparison of the total mass specific capacitance with respect to different simple precipitation time (from 0 min to 2 hours). (**b**) SEM image of the buckled MnO_2/CNT electrode shows the stable bonding between MnO_2 and CNT substrate (**c**) SEM image of a thicker MnO_2 nanoparticle layer on the CNT film surface with 1 hour precipitation before GCD and DSR cycles (**d**) SEM image of 1 hour precipitation sample after long GCD cycles (10000 cycles) under DSR cycles (24300 cycles) at 6% s^{-1} strain rate.

For stretchable energy storage devices, the attainable mechanical stretching-releasing cycles, which reveal their durability for practical applications, are also very critical in addition to evaluating their GCD cycling stability. The DSPs were tested for 5000 DSR cycles with different strain rates of 1.5, 3, and 6% strain s^{-1} (one

stretching-releasing cycle time is 44.44, 22.22, and 11.11 s, respectively) and at a constant current density of 10 A g^{-1}. Figure 2.6a shows that the capacitance retention is extremely high at all strain rates where the capacitance fades by less than 1%, further proving the excellent durability of the pseudocapacitors from the mechanical viewpoint.

To illustrate the particular capacitance variation under both charge-discharge and the stretching-releasing cycles, the dynamic behavior at different strain rates is enlarged and depicted in Figure 2.6b and c. The capacitance fluctuates from 90 to 92 F g^{-1}, and the variation is less than 1.5 F g^{-1}, which is within 2.5% of the capacitance. This extremely stable capacitive behavior at various strain rates indicates that there is no significant effect from the mechanical stretching-releasing on the charge-discharge performance of the pseudocapacitor cell, proving that the pseudocapacitors can be reversibly charged and discharged under dynamic stretching.

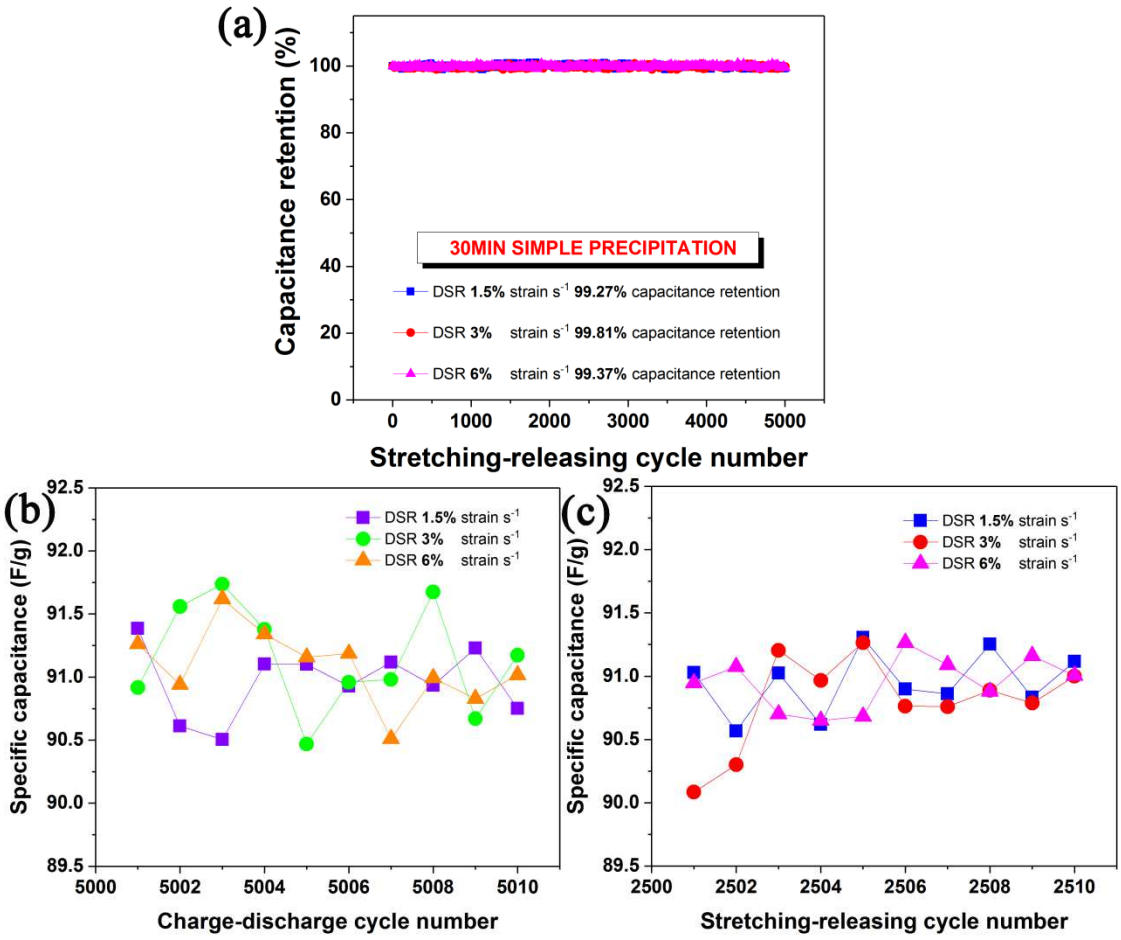

Figure 2.6 Simultaneously applied DSR cycling at the strain rates of 1.5, 3, and 6% strain s^{-1}, the DSP with 30 min precipitation shows excellent cycling stability for (**a**) 5000 mechanical stretching-releasing cycles. Less than 1.5 F g^{-1} capacitance fluctuation is observed from the zoomed-in charge-discharge cycles from 5001 to 5010 (**b**) and the stretching-releasing cycles from 2501 to 2510 (**c**).

In order to investigate the rate capability of DSPs, the cycling performance at a progressively increasing current density was recorded at the strain rate of 6% strain s^{-1} and is shown in Figure 2.7a. Even experiencing sudden changes of current density, the stretchable pseudocapacitor exhibits very stable capacitance at each current density

(50 cycles at each current density) from 2 to 50 A g^{-1}. After 250 continuous cycles at various current densities, the current density was turned back to 2 A g^{-1} and ~99.9% of the initial capacitance (~112 F g^{-1}) can be recovered.

To further highlight the stability of the stretchable structure design of DSPs, programmed CV testing was also recorded (Figure 2.7b). The DSP was initially subjected to 10 continuous cycles at 10 mV s^{-1} and was then measured at 20, 50, 100, 200, and 500 mV s^{-1}, successively and at the strain rate of 6% strain s^{-1}. The stepwise testing reveals that the cell can maintain electrochemically stable even after sudden scan rate changes and continues to be stable under the intense and dynamic mechanical loading. The specific capacitance of the MnO_2/CNT cell decreases to 100 F g^{-1} from ~119 F g^{-1} as the scan rate increases from 50 to 200 mV s^{-1}, representing only 16% decrease compared with that at the scan rate of 50 mV s^{-1}. This result indicates the excellent capacitive behavior and high-rate capability of DSPs. Furthermore, upon switching the scan rate back to 10 mV s^{-1}, the specific capacitance of MnO_2/CNT was able to be fully recovered, demonstrating excellent capacitance retention of the DSPs. It is also meaningful to point out that in order to examine the endurable capability of the cell, we purposely suspended the CV test for one week, and resumed the test for another 10 cycles at the same scan rate of 10 mV s^{-1}. There is only a slight capacitance loss, thus showing excellent capacitance durability.

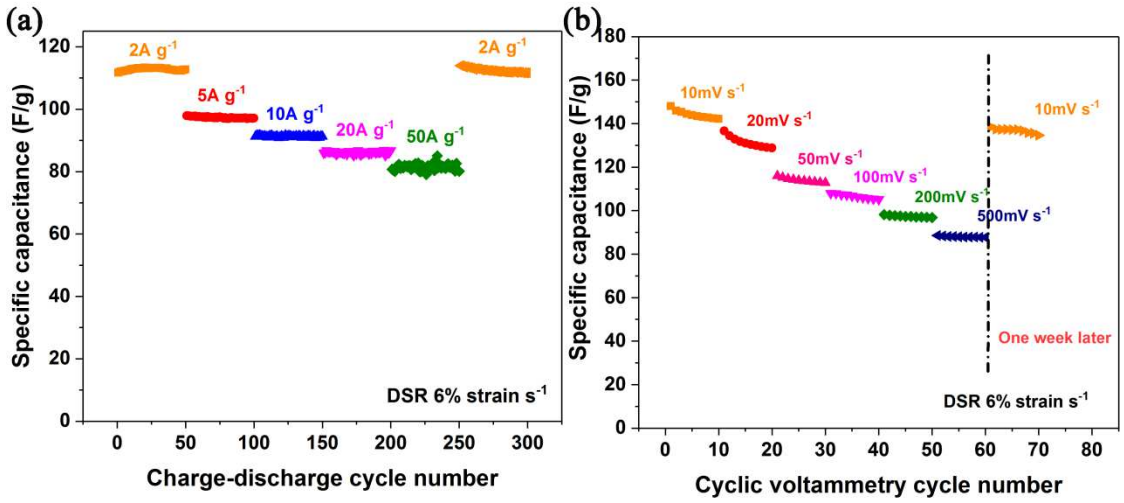

Figure 2.7 Cycling stability at (**a**) consecutively varied current densities and (**b**) with consecutively various cyclic scan rates at the strain rate of 6% strain s^{-1}.

Pseudocapacitance is expected to be much higher than EDLC-capacitance because pseudo-capacitive materials take advantage of relatively slower redox reactions. However, it is unclear on the redox kinetics of the hybrid MnO_2/CNT system for stretchable pseudocapacitors. The principal objective of the EIS measurements is to gain insights into how fast the pseudocapacitive behavior can be for the MnO_2/CNT system in stretchable modes and its coupling effects with the dynamic mechanical strain rate. Figure 2.8a shows the Nyquist plots in the frequency range from 100 kHz to 10 mHz measured at equilibrium open circuit potential at different strain rates from 0.15% strain s^{-1} to 6% strain s^{-1} with repeated dynamic stretching and releasing. We introduced here an extremely slow strain rate of 0.15% strain s^{-1} (444.4 s for one mechanical stretching-releasing cycle) in order to create a mechanically stable environment to ensure that the mechanical cycle time is sufficiently long for the redox reaction of the stretchable pseudocapacitors. The

Nyquist plots can be represented by a modified Randles circuit with a set of resistors and capacitors in series and parallel as shown in Figure 2.8b. The first intersection point on the real axis of the Nyquist plot in the high-frequency region provides the value of the series resistance R_s. The charge transfer resistance R_{ct} is the second intersection point of the semicircle on the real axis which is mainly derived from the resistance between the electrode and the electrolyte. The double layer capacitance C_{dl} is connected in parallel to R_{ct}. The semicircle proves that there are charge transfer processes for the MnO_2/CNT pseudocapacitors. After the semicircle, the Nyquist plots show a long tail in the low-frequency region pertaining to the diffusion of ions into the bulk of the electrode. The transition from the mid-frequency to the low-frequency tail is represented by the Warburg diffusion element, W_o. Faradaic capacitance arisen from the contribution of MnO_2 is represented as C_{pseudo}. At high frequencies, the capacitor impedance becomes much smaller, and the system resistance is dominated by the resistors and polarization impedances. At low frequencies, an ideal polarizable capacitance would give a straight line with large angles with respect to Z' or almost parallel to Z''.

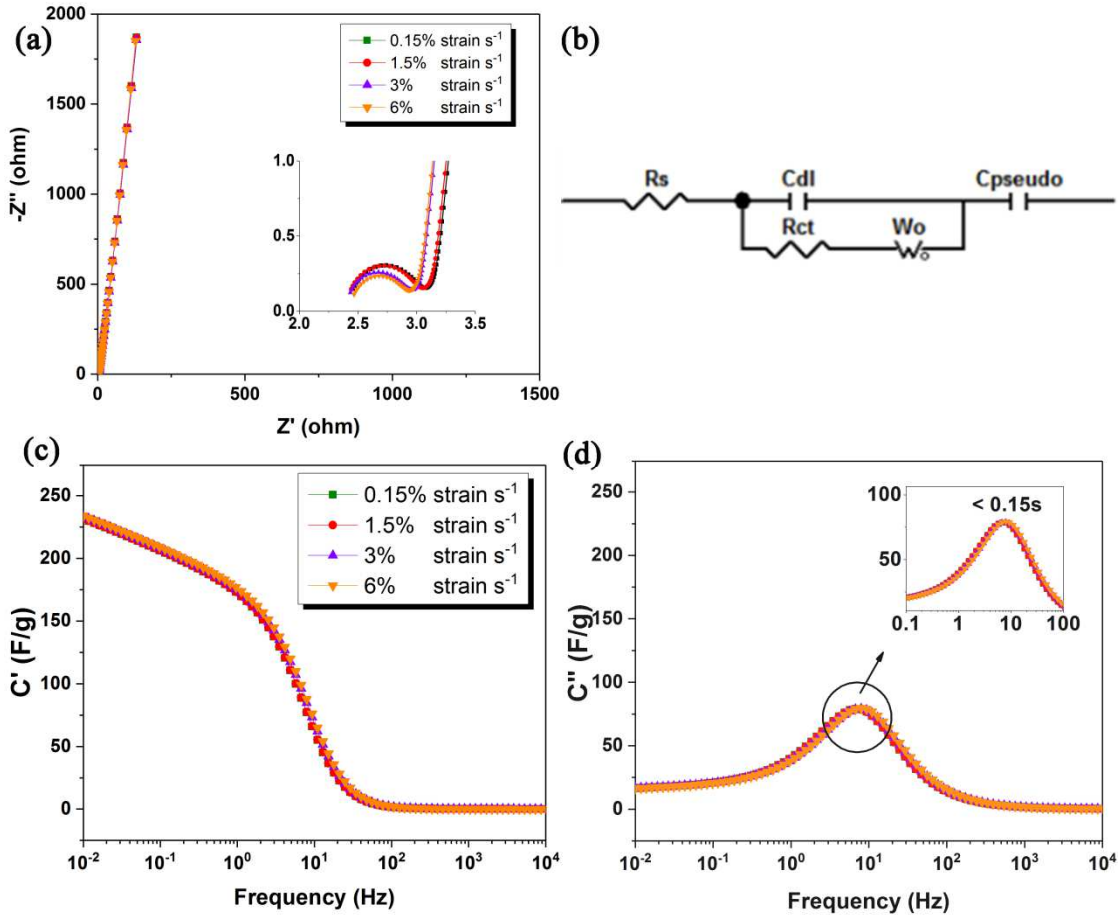

Figure 2.8 (**a**) Electrochemical impedance spectroscopy measurements on the dynamically stretchable pseudocapacitors at different strain rates with repeated stretching and releasing in the frequency range from 100 kHz to 10 mHz. **Inset**: the enlarged high-frequency region of the Nyquist Plots. (**b**) Modified Randles equivalent circuit representing the circuit elements in the Nyquist plots. The equivalent circuit is used to fit the Nyquist plots using the software ZVIEW. (**c**) Bode plots of the real specific capacitance. (**d**) Bode plots of imaginary specific capacitance related to the relaxation time constant. Both are calculated from EIS data for the DSPs at 0.15, 1.5, 3, and 6% strain s^{-1}. C' and C'' are real specific capacitance and imaginary specific capacitance, respectively.

As shown in Figure 2.8a, the low-frequency straight lines are almost vertical, indicating the good capacitive behavior. Both R_s and R_{ct} are very small at all strain

rates as shown in the inset of Figure 2.8a, which emphasizes the high-frequency semicircle of the pseudocapacitors with excellent electric pathways of CNT and fast redox reactions of MnO_2 as a pseudo-capacitive material resulted from the MnO_2/CNT hybrid structure.

All of the equivalent circuit-fitting results were performed using the EIS data fitting program ZVIEW and presented in Table 2.1. It is observed that the values of all fitting parameters are almost stable with different strain rates. However, it is interesting to notice that the strain rate slightly affects the pseudo-capacitive performance; with a small R_{ct} decrease of 0.43 ohms at DSR 6% s^{-1} compared to 0.57 ohms at DSR 0.15% s^{-1}, indicating an improved electrode/electrolyte interface at a relatively high strain rate. This could be attributed to better wetting of the MnO_2/CNT surface by the increased strain rate, which gives easier access of the electrolyte ions into the electrode materials. We express it as the mechanical activation for stretchable/flexible energy storage devices: a faster dynamic stretching and releasing leads to an increase in the values of C_{dl} and C_{pseudo}; however, the increments are very small. Compared to EDLCs, a pseudocapacitor with the buckled MnO_2/CNT electrodes has two components to contribute to the mass capacitance, EDLC capacitance (C_{dl}) and the pseudocapacitance (C_{pseudo}). As shown in Table 2.1, it is evident that the DSP system is pseudo-capacitance dominant and the pseudo-capacitive stability could ensure the stable performance of the DSPs.

Table 2.1 Equivalent circuit parameters obtained from the curve fitting results

Fitting Parameter	$R_s(\Omega)$	C_{dl} (F/g)	$R_{ct}(\Omega)$	$W_o(\Omega)$	C_{pseudo}(F/g)
0.15% strain s^{-1}	2.45	0.12	0.57	0.48	106.35

1.5% strain s^{-1}	2.44	0.12	0.57	0.48	106.76
3% strain s^{-1}	2.44	0.14	0.48	0.45	106.94
6% strain s^{-1}	2.47	0.16	0.43	0.44	109.53

The relaxation time constant τ_0 ($\tau_0 = f_0^{-1}$) is a quantitative measure of how fast a capacitor device could be charged and discharged reversibly and of practical importance in determining the rate, at which the electrical response of a capacitor device can take place. The relaxation time constant from Figure 2.8d in the frequency-dependent imaginary capacitance analysis quantitatively reveals its performance, and these results give valuable insights into the role of dynamic strain variation on the frequency response of the DSPs. In Table 2.2 and Figure 2.8d, the relaxation time constant is less than 0.15 s at all strain rates under the dynamic stretching and releasing for the DSPs, much shorter than reported values for planar activated carbon based microsupercapacitors[13] (~0.7 s) and multi-wall nanotube based supercapacitors[14] (~0.7 s). The extremely short relaxation time could be attributed to the excellent conductivity of the CNT network, which facilitates the redox reaction of MnO_2 and leads to rapid pseudocapacitive behavior. Although the mobility of the ions in the organic electrolyte is slower than that of ions in the aqueous electrolyte due to the larger viscosity and the larger ion size, the relatively weak chemisorption between the MnO_2 and electrolyte interface leads to the fast adsorption/desorption, thus extremely small relaxation time constant, which further confirms that redox reaction would be initiated from the surface layer of the MnO_2 in contact with the electrolyte. Compared to the mechanical stretching-releasing cyclic time (τ'), in which the DSP accomplishes one mechanical stretching-releasing cycle, τ_0 is extremely short, at least two magnitude shorter (Table 2.2). This extremely short relaxation time τ_0 at all strain rates for DSPs strongly suggests that the pseudocapacitors built with the buckled

MnO_2/CNT electrodes possess enormous potential for stable and instantaneous delivery of ultra-high power and energy under rapid mechanical deformation.

Table 2.2 Comparison of the relaxation time constant (τ_0) and stretching-releasing cycle time (τ') at different strain rates

Strain rate	τ_0(s)	τ'(s)
0.15% strain s^{-1}	0.148	444.4
1.5% strain s^{-1}	0.148	44.44
3% strain s^{-1}	0.126	22.22
6% strain s^{-1}	0.126	11.11

The bendability of DSPs is another determining factor when considering their enormous potential market in applications such as roll-up display devices, smart sensors, e-papers, and flexible wearable electronics. Therefore, we conducted a flexibility test of our device at dynamic bending-releasing (DBR) states that are different from static bending tests.[15] Here, we define one bending-releasing cycle as the cell is bent from 180° (flat, also 0°) to 90° and then released back to 180° (as the schematic in Figure 2.9a). The capacitance retention of the DSPs under strain rates of 1.5, 3, and 6% strain s^{-1} are shown in Figures 2.9b and 2.9c.

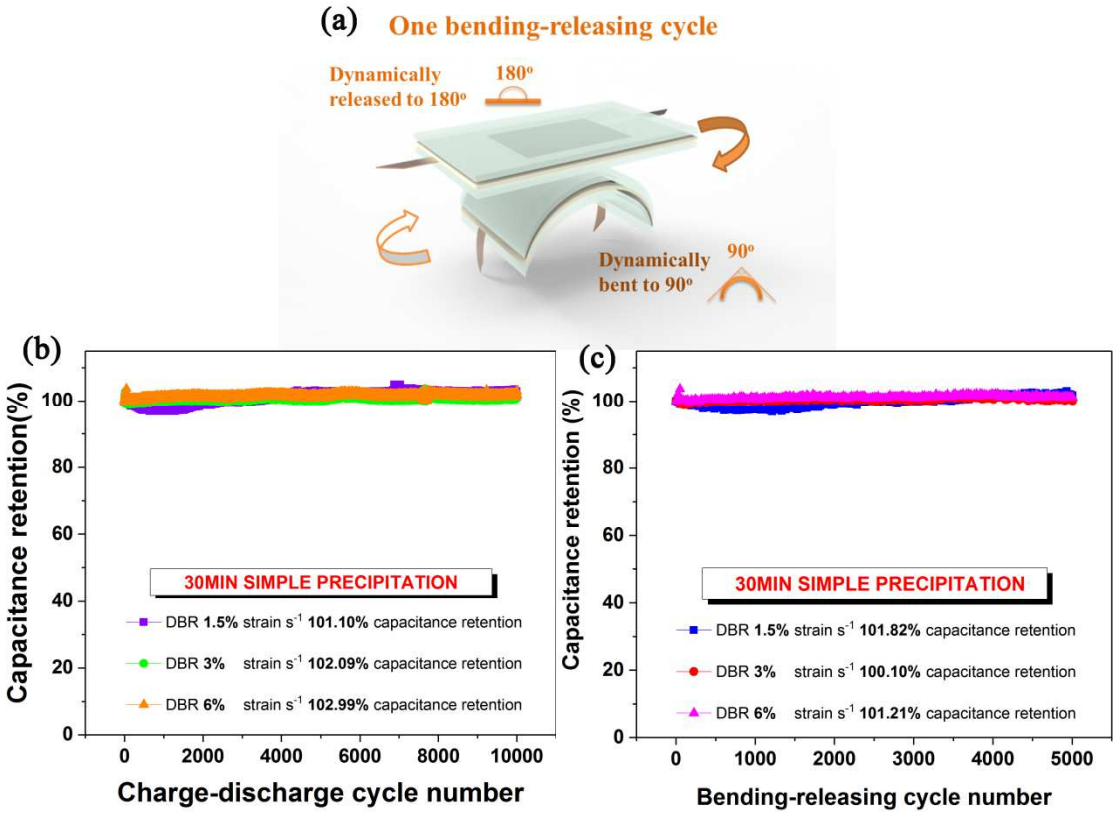

Figure 2.9 (**a**) Schematic of one mechanical bending-releasing cycle between 180° and 90°. With applied dynamic bending-releasing (DBR) cycling at a different strain rate of 1.5, 3, and 6% strain s^{-1}, the DSP shows excellent cycling stability with (**b**) 10000 GCD cycles and (**c**) 5000 mechanical bending-releasing cycles. The current density is 10 A g^{-1}.

It is worth noting that different from the EDLCs/pseudocapacitors with a fading in capacitance under bending,[16] an excellent stability for DSPs under DBR was repeatedly observed, *i.e.* at different strain rates, about 1-2% improvement in the specific capacitance retention after 10000 electrochemical charge-discharge cycles and 5000 mechanical bending-releasing cycles is achieved, further proving the remarkable flexibility and stability of the DSP cell. This is likely the result of "mechanical-electrochemical synergy activation", in which ions tend to adjust with

cycling to fully access the active electrode material under the DBR process. Therefore, the DSP is not only stretchable but also bendable, demonstrating that DSP can potentially be applied as a flexible power source in producing flexible electronic devices.

2.4 Conclusions

In conclusion, the electrochemical stability of dynamically stretchable pseudocapacitors based on the buckled MnO_2/CNT electrodes was systematically studied at different strain rates of stretching for the first time. We have successfully demonstrated an excellent pseudo-capacitive stability of the DSPs under both electrochemical charge-discharge cycles and mechanical stretching and releasing cycles. The long cycle GCD measurements also showed excellent stability in capacitance from both electrochemical and mechanical viewpoints. The extremely small relaxation time constants explained fundamentally that repeated stretching and releasing at the applied strain rates would not affect the stable performance of DSPs. All of these findings are expected to enlighten a broad area of stretchable energy storage devices including DSPs.

REFERENCES

1 Yu, C.; Masarapu, C.; Rong, J.; Wei, B.; Jiang, H. Stretchable Supercapacitors Based on Buckled Single-Walled Carbon-Nanotube Macrofilms. *Adv. Mater.* **2009**, *21*, 4793–4797.

2 Li, X.; Gu, T.; Wei, B. Dynamic and Galvanic Stability of Stretchable Supercapacitors. *Nano Lett.* **2012**, *12*, 6366–6371.

3 Niu, Z.; Dong, H.; Zhu, B.; Li, J.; Hng, H. H.; Zhou, W.; Chen, X.; Xie, S. Highly Stretchable, Integrated Supercapacitors Based on Single-Walled Carbon Nanotube Films with Continuous Reticulate Architecture. *Adv. Mater.* **2013**, *25*, 1058–1064.

4 Xu, S.; Zhang, Y.; Cho, J.; Lee, J.; Huang, X.; Jia, L.; Fan, J. a; Su, Y.; Su, J.; Zhang, H.; *et al.* Stretchable Batteries with Self-Similar Serpentine Interconnects and Integrated Wireless Recharging Systems. *Nat. Commun.* **2013**, *4*, 1543.

5 Chen, P.; Chen, H.; Qiu, J.; Zhou, C. Inkjet Printing of Single-Walled Carbon nanotube/RuO2 Nanowire Supercapacitors on Cloth Fabrics and Flexible Substrates. *Nano Res.* **2010**, *3*, 594–603.

6 Kim, J.; Lee, K. H.; Overzet, L. J.; Lee, G. S. Synthesis and Electrochemical Properties of Spin-Capable Carbon Nanotube Sheet/MnOx composites for High-Performance Energy Storage Devices. *Nano Lett.* **2011**, *11*, 2611–2617.

7 He, Y.; Chen, W.; Li, X.; Zhang, Z.; Fu, J.; Zhao, C.; Xie, E. Freestanding Three-Dimensional graphene/Mno2 Composite Networks as Ultralight and Flexible Supercapacitor Electrodes. *ACS Nano* **2013**, *7*, 174–182.

8 Zhang, K.; Zhang, L. L.; Zhao, X. S.; Wu, J. Graphene/Polyaniline Nanofiber Composites as Supercapacitor Electrodes. *Chem. Mater.* **2010**, *22*, 1392–1401.

9 Hu, L.; Pasta, M.; Mantia, F. La; Cui, L.; Jeong, S.; Deshazer, H. D.; Choi, J. W.; Han, S. M.; Cui, Y. Stretchable, Porous, and Conductive Energy Textiles. *Nano Lett.* **2010**, *10*, 708–714.

10 Yue, B.; Wang, C.; Ding, X.; Wallace, G. G. Polypyrrole Coated Nylon Lycra Fabric as Stretchable Electrode for Supercapacitor Applications. *Electrochim. Acta* **2012**, *68*, 18–24.

11 Zhu, H.; Wei, B. Direct Fabrication of Single-Walled Carbon Nanotube Macro-Films on Flexible Substrates. *Chem. Comm.* **2007**, 3042–3044.

12 Li, X.; Wei, B. Facile Synthesis and Super Capacitive Behavior of SWNT/MnO2 Hybrid Films. *Nano Energy* **2012**, *1*, 479–487.

13 Pech, D.; Brunet, M.; Durou, H.; Huang, P.; Mochalin, V.; Gogotsi, Y.; Taberna, P.-L.; Simon, P. Ultrahigh-Power Micrometre-Sized Supercapacitors Based on Onion-like Carbon. *Nat. Nanotechnol.* **2010**, *5*, 651–654.

14 Portet, C.; Yushin, G.; Gogotsi, Y. Electrochemical Performance of Carbon Onions, Nanodiamonds, Carbon Black and Multiwalled Nanotubes in Electrical Double Layer Capacitors. *Carbon* **2007**, *45*, 2511–2518.

15 Yuan, L.; Lu, X.-H.; Xiao, X.; Zhai, T.; Dai, J.; Zhang, F.; Hu, B.; Wang, X.; Gong, L.; Chen, J.; *et al.* Flexible Solid-State Supercapacitors Based on Carbon nanoparticles/MnO_2 Nanorods Hybrid Structure. *ACS Nano* **2012**, *6*, 656–661.

16 Guo, C. X.; Li, C. M. A Self-Assembled Hierarchical Nanostructure Comprising Carbon Spheres and Graphene Nanosheets for Enhanced Supercapacitor Performance. *Energy Environ. Sci.* **2011**, *4*, 4504–4507.

Chapter 3

ALL-SOLID-STATE STRETCHABLE PSEUDOCAPACITORS ENABLED BY CARBON NANOTUBE FILM-CAPPED SANDWICH-LIKE ELECTRODES

3.1 Introduction

In chapter 2, anchoring functional pseudo-capacitive materials on the wavy carbon substrates has been demonstrated for the first time in stretchable pseudocapacitors (20 *wt.*% of MnO_2); however, excessive loading of the functional guests also results in aggregation and thick coating, leading to poor electrochemical performance (i.e. cycling stability and rate capability).[1] Incorporating a high mass loading of the functional guests (i.e. pseudo-capacitive materials) in their "eigenstate" of powder (slurry or paste with solvents) into the stretchable scaffolds while maintaining the desired structure and electrical/mechanical properties is very challenging. Although pasting functional guests directly on the wavy carbon substrate is one way to introduce more active pseudo-capacitive material,[2,3] they can easily delaminate or detach from the surface of the carbon substrate or fracture. Consequently, high-performance stretchable pseudocapacitors have not been realized based on the current technological strategies. Hence, it is greatly needed to develop a multifunctional nanostructured electrode, which could simultaneously provide a high specific capacitance, good rate capability, and superior cycling stability for stretchable pseudocapacitors.

In this chapter, we construct a novel sandwich-like electrode with high stretchability and mechanical/electrochemical stability. The sandwich-like stretchable

pseudocapacitors (SSP) can bear up to 100% strain and exhibit stable performance after 10000 stretching-releasing cycles. To the best of our knowledge, it represents the highest mass loading of active pseudo-capacitive materials (76 *wt.*%) among the reported stretchable pseudocapacitors with stable performance. Moreover, the electrochemical performance remains stable under a high stretching-releasing speed of 8% strain per second. Different from the widely developed device-level stretchability,[4,5] the novel sandwich-like structural design from the component-level view of stretchability is the key to secure the high performance for stretchable pseudocapacitors.

3.2 Experimental

3.2.1 SSP assembly

The free-standing CNT films and MnO_2 were prepared using the method described in Chapter 2. Freestanding CNT films and MnO_2 nanoparticles were weighed and mixed with DI water followed by ultra-sonication to prepare the MnO_2-fragmented CNT (FCNT) composite electrodes. The as-prepared CNT film was laminated tightly with a UV-light treated PDMS substrate. The resulting ink solution consisting of MnO_2-FCNT nanoparticles was drop-casted on the CNT film which has been pre-stretched on PDMS. Then another CNT film was attached to the MnO_2-FCNT surface to form the sandwich structure. It is noted that no polymer binder or organic solvents were employed in the whole process.

To fabricate an SSP cell, liquid Na_2SO_4-PVA gel electrolyte was pasted on a pre-determined area of the CNT/MnO_2-FCNT/CNT/PDMS component. Two of such films were stacked together with the electrolyte-coated parts overlapping. The

assembled SSP was dried at RT to allow the gel electrolyte to solidify. The weight percentage of each component was measured by weighing in-process products after each step.

3.2.2 Characterizations

The surface and cross-section morphology of SSP were characterized by Zeiss Auriga 60 FIB/SEM. The dynamic electrochemical testing were performed while the SSP was being stretched and released between 0% to 100% strain. CV measurements were obtained using the PARSTAT 2273 workstation in the scan range between 0 and 0.8V.

3.2.3 Calculations

MnO_2 weight percentage calculation is based on each layer's mass. There was 76 *wt.*% of MnO_2 and 24 *wt.*% of CNT (including the CNT film and FCNT) without any non-conductive additive material. The specific capacitance of the sandwich-like and non-sandwich electrodes were both calculated on the total mass of the electrode.

3.3 Results and Discussion

Figure 3.1a illustrates the structural design of the SSP. The as-prepared CNT film was laminated tightly with a UV-light treated PDMS substrate. FCNT and MnO_2 nanoparticles were ultrasonicated with DI water, and the resulting ink solution was cast on a pre-stretched CNT film using the doctor blade coating method. Another CNT film was then placed on top of the MnO_2-FCNT core layer to form SSP without any additional treatment. It is noted that no polymer binder or organic solvents were employed in the whole process. Compared to the structure of non-sandwich

stretchable pseudocapacitors (NSSP) illustrated in Figure 3.1b, we expect our novel SSP have more structure stability and improved rate capability.

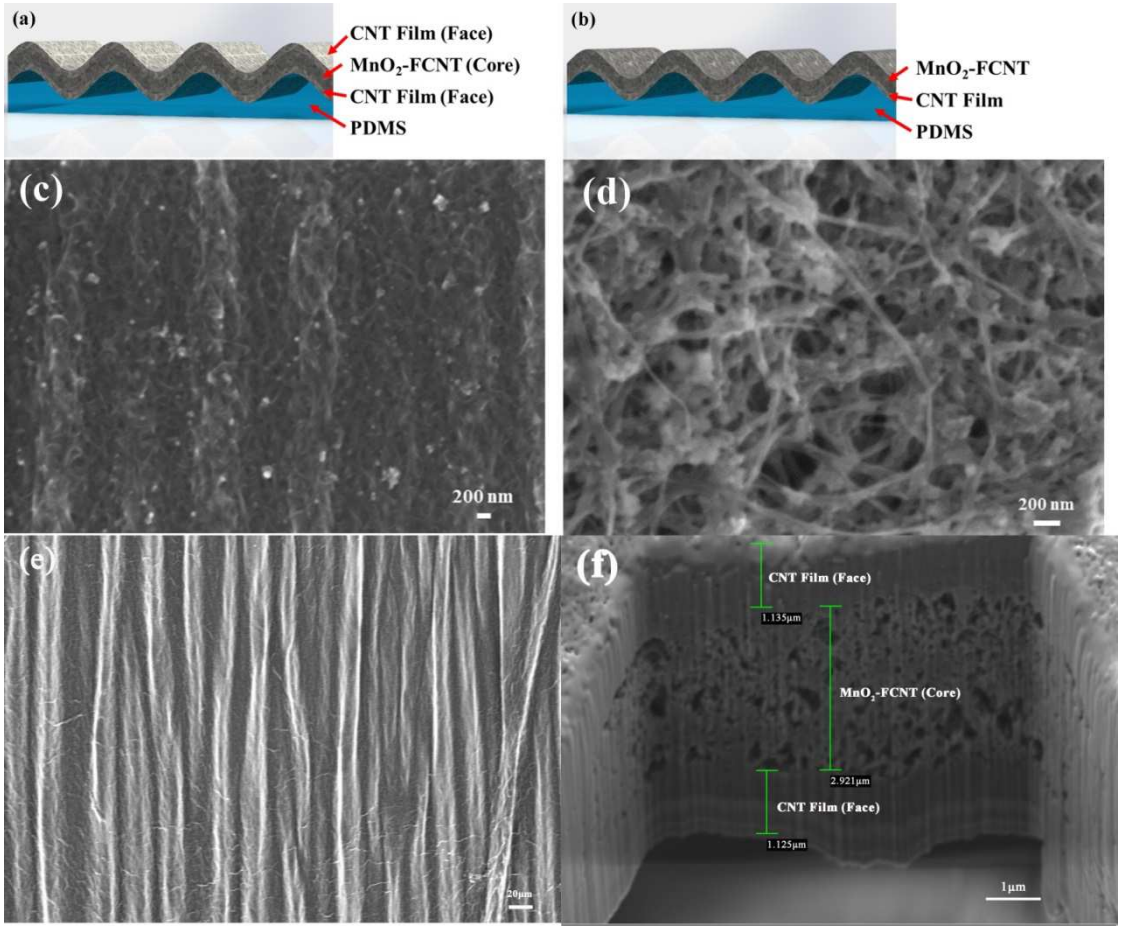

Figure 3.1 Schematic of the components of designed configurations. (**a**) Sandwich-like structure combined with a PDMS substrate. (**b**) Non-sandwich structure combined with a PDMS substrate. (**c**) SEM image of buckled sandwich-like electrode with a continuous CNT film cap. (**d**) SEM image of the MnO_2-FCNT composite with the porous structure but without a CNT film cap. (**e**) SEM image of buckled sandwich-like electrode after 10000 mechanical cycles. (**f**) Cross-sectional SEM image of the sandwich-like electrode.

The sandwich-like structure has two facial layers and one core layer. The bottom "Face" CNT film layer is employed as the conductive substrate, which holds great bonding with the PDMS to form the wavy structure. Compared to a conventional Al foil current collector, improved ion diffusion kinetics, lower polarization, and higher gravimetric energy densities could be expected. The top "Face" CNT film layer (Figure 3.1c) that encapsulating the MnO_2-FCNT "Core" layer functions not only as a current collector but also as MnO_2 reservoirs and barrier (i.e., MnO_2 trapping) layer, which is extremely vital for the mechanical stability of the stretchable pseudocapacitors. The 2-D continuous conductive CNT capping with a high surface area is favorable for efficient electrolyte infiltration and to ensure the structural stability of preventing the excessive MnO_2 nanoparticles from dissolving into the electrolyte during charge-discharge and particularly, under mechanical shocks in the stretching-releasing process. The top "Face" CNT film is also expected to buffer large volumetric expansion of MnO_2 during the cycling process. The "Core" MnO_2-FCNT composite has a high mass loading of MnO_2 nanoparticles that are homogeneously distributed in the FCNT-entangled integrity to form the porous structure (Figure 3.1d), which is self-supported and can prevent nanoparticles from aggregation. It is noted that the FCNT meshes were discovered to have played the conductive binder function,[6] which avoids the use of a polymer binder and substantially reduces the "dead volume" in the electrode.

The sandwich structures provide SSP with possible long cycling life and excellent rate capability. This design also avoids any modification of MnO_2 nanoparticles and simplifies the fabrication process of electrodes. Adhesion between the top and bottom face CNT layers is also expected to be strengthened by the

roughness of the CNT films and chemical interactions such as hydrogen bonding and the adhesive property of FCNT to prevent delamination over repeated stretching-releasing cycles. For stretchable pseudocapacitors, the attainable mechanical cycles are very critical for its potential application as a stretchable/flexible power source. In Figure 3.1e, we observe that the buckled structure of SSP still exists after 10000 repeated stretching cycles and each layer in the sandwich structure still tightly connected (Figure 3.1f), which guarantees this structure for its potential application as the stretchable pseudocapacitors. Therefore, in this component-level design, not only are all the desired functions of each constituent utilized to increase the concentration of MnO_2 mass loading, but additionally, a synergistic effect can be expected.

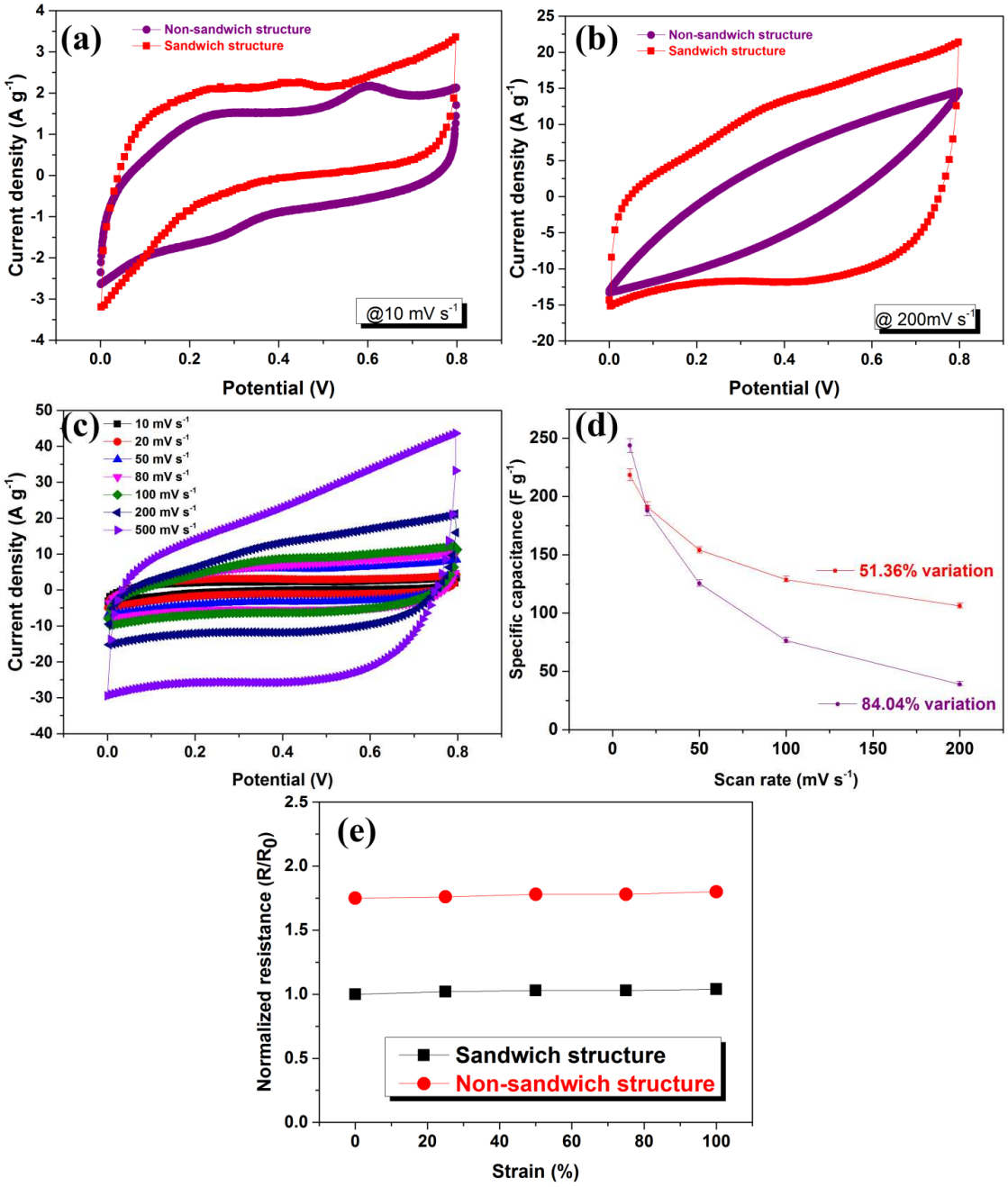

Figure 3.2 Cyclic voltammetry (CVs) of the SSP and NSSP measured at a scan rate of (**a**) 10 mV s^{-1}; (**b**) 200 mV s^{-1}. (**c**) CVs of SSP at the scan rate from 10 to 500 mV s^{-1}. (**d**) Scan rate dependence of the specific capacitance in different structures (SSP: a red dot; NSSP: a purple dot). (**e**) Comparison of normalized electrical resistances versus tensile strains of SSP and NSSP electrodes.

A series of electrochemical measurements of SSP was performed and compared to that of NSSP to prove the efficiency of this unique sandwich-like configuration in enhancing the performance of stretchable pseudocapacitors (Figure 3.2). The CV profiles of SSP retain a rectangular shape at both low and high scan rates with respect to 10 and 200 mV s^{-1} (Figure 3.2a and 3.2b), whereas the CV profiles of NSSP, recorded at the high scan rate of 200 mV s^{-1}, is obviously distorted, demonstrating the superior ion response of the sandwich-like structure. The specific capacitance of SSP at different scan rates is summarized in Figure 3.2c. To be specific, the specific capacitance decreases when the scan rate increases from 10 to 500 mV s^{-1}, at a scan rate of 50 mV s^{-1}, the specific capacitance is 154 F g^{-1}, which is better than most previously reported stretchable pseudocapacitors and stretchable micro-supercapacitors.[1,7,8] The CVs are all in a rectangular shape within the potential range from 0 to 0.8V, with little distortion even at a high scan rate of 500 mV s^{-1}, indicating that the SSP cell maintains excellent capacitive behavior. Moreover, the high MnO_2 mass loading (76 *wt.*% of MnO_2 or a specific areal mass loading of ~1.0 mg cm^{-2}) in SSP does not result in significant decrease in the rate capability (Figure 3.2d). The improved conductivity by the top CNT film in SSP significantly boosts the rate capability. As shown in Figure 3.2d, the specific capacitance of SSP is ~106 F g^{-1} at 200 mV s^{-1}, which is 51.36% of the attainable capacitance at 10 mV s^{-1}. Although a higher specific capacitance is achieved with NSSP (84 *wt.*% of MnO_2) at a low scan rate, the NSSP cell suffers from the significant low rate capability (capacitance variation changes with 84.04% in the range of 10 to 200 mV s^{-1}). This poor performance is attributed to the dense morphology of the composites which leads to inefficient electrical conductivity. Figure 3.2e shows the normalized resistance at

different strains, where R_0 is the resistance of the unstretched SSP electrode. Although the conductivity of both SSP and NSSP electrodes were not increasing too much (less than 5%) with the increase of strain up to 100%, the resistance of NSSP electrode is always ~78% higher than the SSP, further confirms that the electrical conductivity of the top CNT film is responsible for the better electrochemical performance of the SSPs, compared to NSSPs. These results indicate that the sandwich-like structure outperforms the non-sandwich structure and exhibits the better rate capability with a substantially high mass loading. The excellent performance of the SSP cell is endowed with the synergetic effect of each involved component: highly accessible specific surface area, reduced ions diffusion resistance, and increased electrical conductivity.

As discussed above, we expected that the sandwich-like structure could build up an excellent conductive bridge by trapping MnO_2 nanoparticles and also facilitate the charge transfer process and benefit to the rate capability. The increase in conductivity of the sandwich structure was also verified using EIS analysis. EIS is commonly used to analyze the electrochemical reaction kinetics. The Nyquist plots of SSP and NSSP are qualitatively similar (Figure 3.3a and 3.3b) with a typical semicircle in the high-medium frequency region and an inclined line at low frequencies, indicating the charge transfer resistance R_{ct} and a mass-transfer process, respectively. The value of R_{ct} for the SSP (~10.7 ohms) is significantly smaller than that of the NSSP (~44 ohms) before cycling due to the high conductivity and surface roughness of the top CNT film, which could also improve the adhesion with MnO_2-FCNT and lower the impedance and polarization of the pseudocapacitor. For SSP, it is worth noting that the 1000 charge-discharge cycles slightly affects the pseudocapacitive behavior; with a small decrease of R_{ct} from 10.7 to 7.6 ohms,

indicating an improved electrode/electrolyte interface. However, the MnO_2 in the NSSP structure heavily dissolved in the electrolyte without the top face CNT wrapping. It should also be noted that the SSP shows a lower R_s of 0.79 ohms before cycling and 0.94 ohms after cycling, compared to NSSP of 3.64 ohms and 5.96 ohms, respectively, which further confirms the better electrical conductivity of the SSP design.

In addition, the cycling stability tests over 1000 GCD cycles for SSP and NSSP were carried out at an extremely high current density of 10 A g^{-1}. Figure 3.3c shows that the capacitance loss of SSP was less than 5% after 1000 consecutive cycles compared with the NSSP structure of ~ 16% loss, suggesting that the synergetic effect of each component in the sandwich structure significantly improves the electrochemical stability of the electrodes.

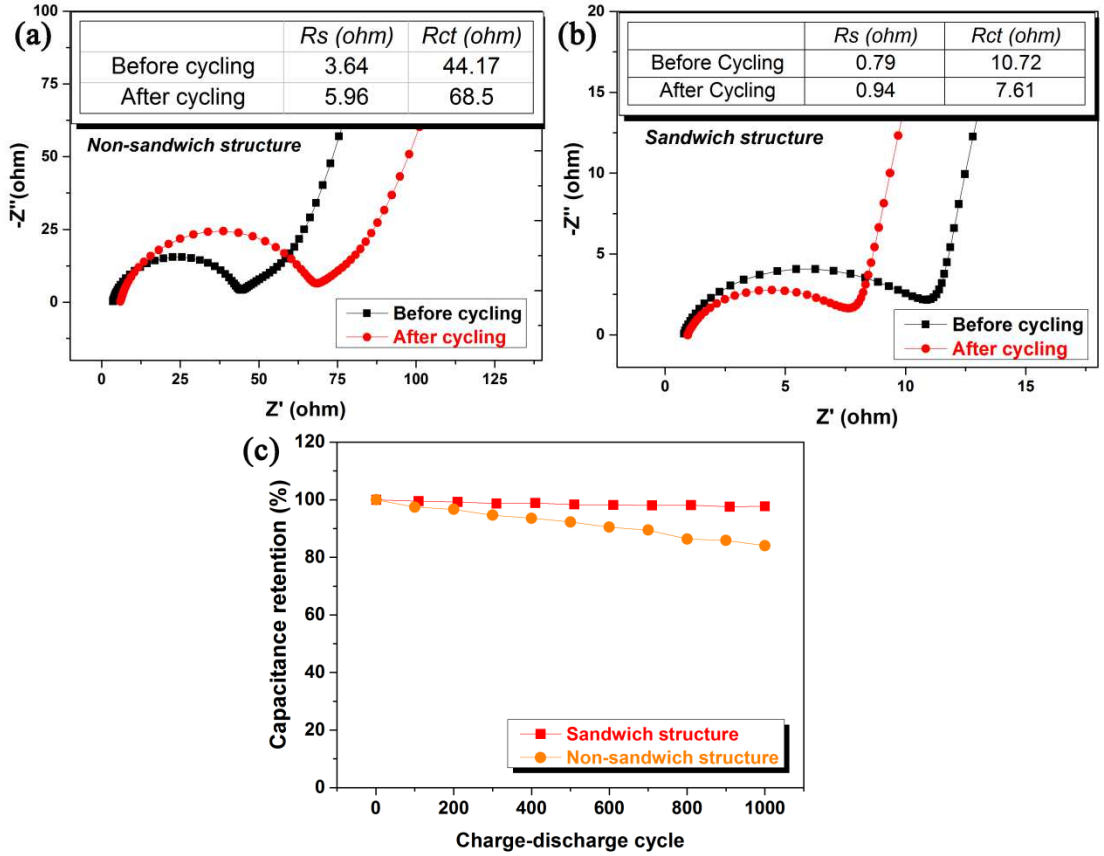

Figure 3.3 EIS tests before and after 1000 charge-discharge cycles with the enlarged high-frequency region of the Nyquist plots for (**a**) non-sandwich structure; (**b**) sandwich structure; (**c**) comparison of the capacitance retention of 1000 electrochemical charge-discharge cycles for the SSP and NSSP.

To demonstrate the stretchability of the SSP cells, GCD curves were recorded at various current densities from 0.1 to 10 A g^{-1} (Figure 3.4a) under 100% tensile strain.[9,10] The plots of potential vs. time are non-linear and maintain a symmetric pseudo-triangular shape during charging and discharging. The curves also reveal the typical pseudocapacitive behavior of the composite electrodes and the Coulombic

efficiency (CE) is as high as ~93%. The calculated specific capacitances of the SSP are 330, 245, 187, 173, 151, and 120 F g^{-1} at current densities of 0.1, 0.2, 1, 2, 5, and 10 A g^{-1}, respectively.

To further demonstrate the merits of this electrode design, cycling performance of the SSP at progressively increased scan rate was also tested (Figure 3.4b) under the 100% tensile strain. The device shows stable performance at each scan rate even suffering from the sudden potential changes. After 70 continuous cycles at varying scan rates, it was changed back to 10 mV s^{-1}, and 97.6% of the initial specific capacitance can be recovered, and another 10 cycles were maintained without noticeable decrease. This result highlights the excellent rate capability under stretching to endow the SSP structure substantial merits as a useful stretchable energy storage device.

Figure 3.4c shows the GCD curves of the SSP taken at different strains from 0, 50, to 100% at 1 A g^{-1}, indicating a slightly higher specific capacitance with the 100% strain in contrast to the 0% strain. Figure 3.4d depicts the typical CV curves in the potential window between 0 and 0.8 V at a scan rate of 100 mV s^{-1}. Similar phenomena of slightly increased specific capacitance at tensile strains from 0, 50, to 100% corresponding to the enhanced specific capacitances of 115.1, 116.4, and 116.5 F g^{-1} are also observed. The excellent stretchability and electrochemical stability are due to the improved interfacial strength to accommodate the various materials with different properties in SSP. Compared with the 0% strain, increased pressure at higher strains between the two electrodes can contribute to the better wettability and hence higher specific capacitances.

Bode plots shown in Figure 3.4e and 3.4f further explain the excellent stretchability and stability of the SSP cells. The real and imaginary parts of specific capacitance are given by the following Equation 3.1 and 3.2,

$$C' = \frac{-Z''(\omega)}{m\omega|Z(\omega)|^2} \quad (3.1)$$

$$C'' = \frac{Z'(\omega)}{m\omega|Z(\omega)|^2} \quad (3.2)$$

where C' and C'' are the real and imaginary parts of specific capacitance, respectively; Z' and Z'' are the real and imaginary parts of impedance Z, respectively; m is total mass of the electrode, and $\omega = 2\pi f$ is the radial frequency.[8] From the C' plot, it is observed that the overall frequency response of the cell from 100 kHz to 10 mHz at different strain rates are almost the same (Figure 3.4e). The stable behavior under the tensile strains from 0, 50, to 100% is in good agreement with CV and GCD results. The relaxation time constant τ^0 ($\tau^0 = f_0^{-1}$) from Figure 3.4f is less than 0.16 s at all strains. This small τ^0 is due to the excellent conductivity of the 2-D continuous conductive wrapping of the top "Face" CNT layer, which facilitates MnO_2 redox reaction and leads to rapid pseudo-capacitive behavior.

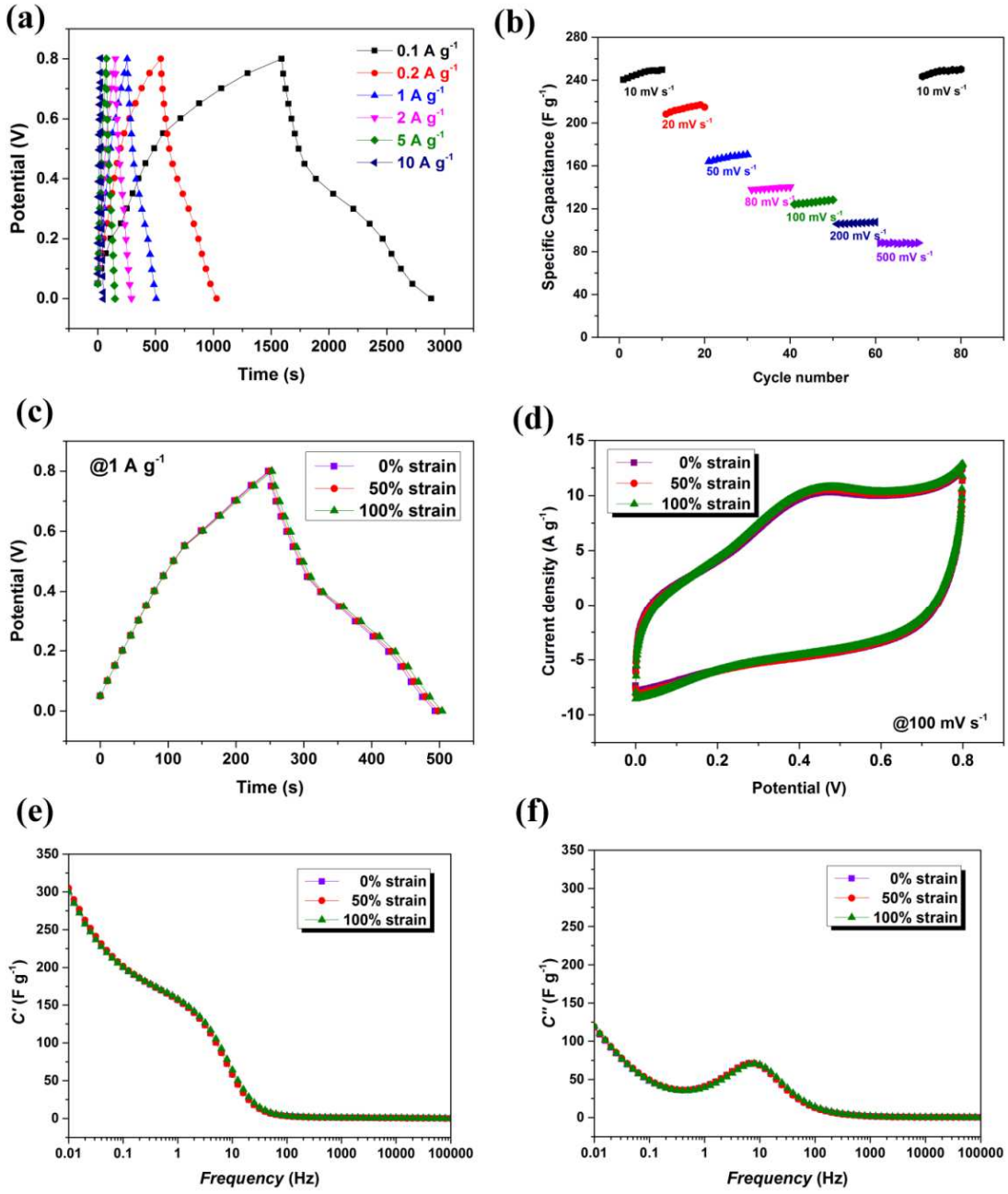
(a)
Potential (V)
Time (s)
0.1 A g-1
0.2 A g-1
1 A g-1
2 A g-1
5 A g-1
10 A g-1
(b)
Specific Capacitance (F g-1)
Cycle number
10 mV s-1
20 mV s-1
50 mV s-1
80 mV s-1
100 mV s-1
200 mV s-1
500 mV s-1
10 mV s-1
(c)
@1 A g-1
Potential (V)
Time (s)
0% strain
50% strain
100% strain
(d)
Current density (A g-1)
Potential (V)
@100 mV s-1
0% strain
50% strain
100% strain
(e)
C' (F g-1)
Frequency (Hz)
0% strain
50% strain
100% strain
(f)
C'' (F g-1)
Frequency (Hz)
0% strain
50% strain
100% strain

Figure 3.4 (**a**) GCD profiles of SSP at 0.1, 0.2, 1, 2, 5, and 10 A g^{-1} at 100% strain. (**b**) Cycling stability with consecutively various scan rates at the strain rate of 100%. Comparison of electrochemical GCD performance of SSPs with 0, 50, and 100% strains at 1 A g^{-1} (**c**) and CV at 100 mV s^{-1} (**d**). Bode plots of the (**e**) real and (**f**) imaginary specific capacitance. Both were calculated from EIS data for the SSPs at 0, 50, and 100% strains. *C*' and *C*'' are real and imaginary specific capacitance, respectively.

Long-term cycling performance of SSP was examined up to 10000 electrochemical GCD cycles at the 100% strain. Due to the highly conducting nature of the CNT framework in the electrode, the specific capacitance is 122 F g^{-1} at the current density of 10 A g^{-1} as shown in Figure 3.5a, which is higher than those delivered by MnO_2/CNT based stretchable and flexible supercapacitors (~91 F g^{-1} at the current density of 10 A g^{-1})[1] and the capacitance retention has maintained up to 95.6% for 10000 cycles at the 100% strain (in Figure 3.5a).

The sandwich structure is expected to accommodate volumetric expansion of MnO_2 during charge-discharge cycles. Compared to the conventional configuration (Figure 3.1b), the migration of MnO_2 nanoparticles can be significantly reduced by this new design with the top CNT film acts as a MnO_2 preserver. This was also verified by testing the attainable mechanical cycles, which reveal device durability for practical applications. The SSP cell was tested for 10000 mechanical cycles from 0 to 100% strain with a stretching-releasing strain rate of 8% at 10 A g^{-1}. Figure 3.5b shows that the capacitance retention was extremely high of more than 93%, to the best of our knowledge, it is the longest mechanical cycles that have been achieved for stretchable energy storage devices.[1] It is apparent that MnO_2 nanoparticles are still firmly anchored on the surface of CNTs and agglomerated at the crossing of nanotubes, although experiencing the volumetric variations generated by the electrochemical

processes and the mechanical shock at the same time. An extended electrochemical cycle is monitored under the DSR condition, where stretching-releasing processes at high speed of 8% strain per second are also introduced at the same time (Figure 3.5c), demonstrating the highly stable dynamic electrochemical performance with negligible voltage fluctuation.

Specific energy and power densities are the key determining factors for the practical applications of stretchable pseudocapacitors. The Ragone plot of SSP under 100% strain is exhibited in Figure 3.5d. The energy and power densities were calculated from the slope of discharge in GCD cycling with a cell voltage window from 0 to 0.8 V. The energy density is ~30 Wh kg^{-1} at the power density of 640 W kg^{-1}. It also preserves 13.4 Wh kg^{-1} energy density as the power density increases to 32 kW kg^{-1}. The enhanced energy density is mainly due to the increased mass loading of MnO_2 compared to the previous study.[1] The specific energy and power density of the SSP surpass the flexible and stretchable EDLCs based on CNT film and graphene.[10, 11-13] Besides, the maximum energy density (~30 Wh kg^{-1}) and power density (~32 kW kg^{-1}) of the SSP is much higher than those of flexible and stretchable conductive polymer based pseudocapacitors,[14-16] and comparable to flexible and stretchable pseudocapacitors derived from MnO_2/CNT and indium oxide (In_2O_3)/CNT inorganic composite electrodes.[17-19]

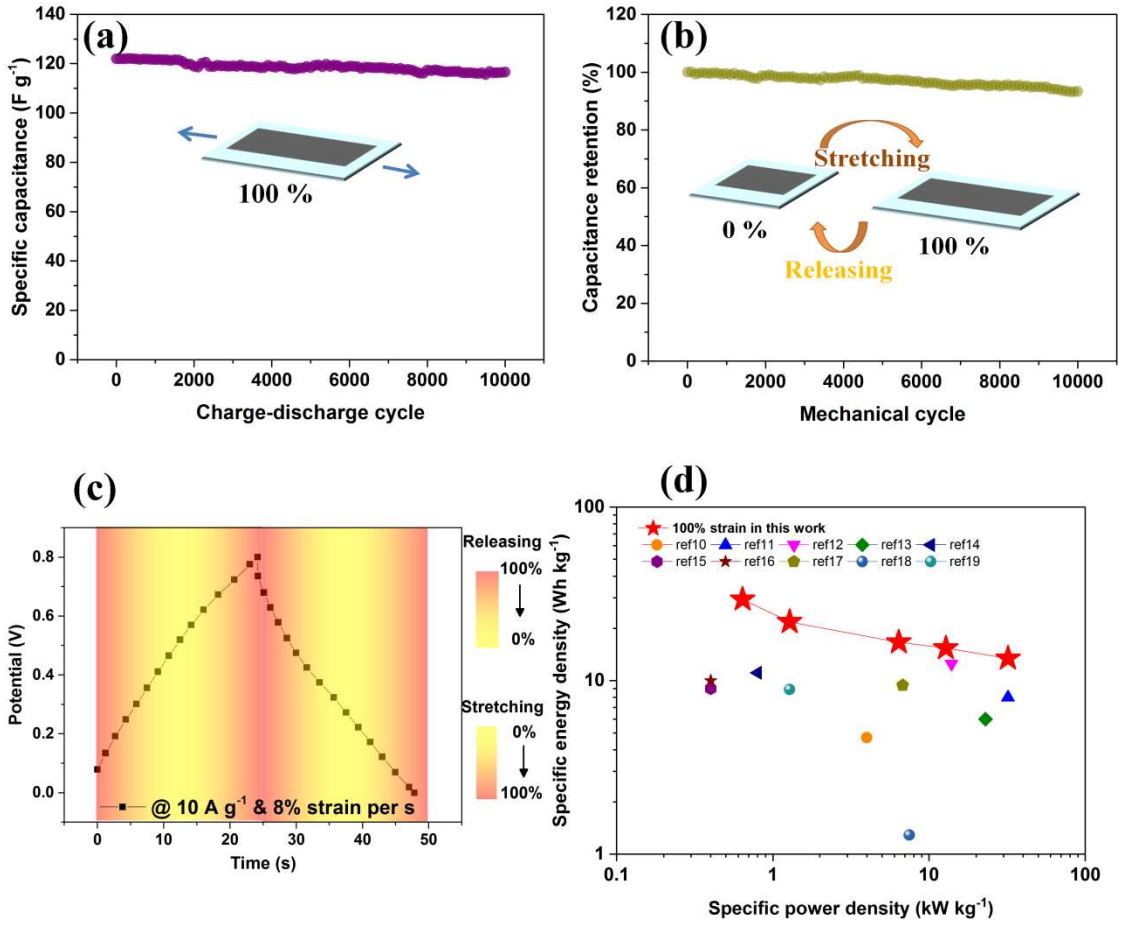

Figure 3.5 Cycling stability for (**a**) 10000 electrochemical cycles at 100% strain and (**b**) 10000 mechanical cycles between 0 and 100% strain at 8% strain per second at 10 A g^{-1}. (**c**) Randomly picked charge-discharge cycles from (**b**). (**d**) Ragone plot of SSP at 100% strain and comparison with other flexible and stretchable EDLCs and pseudocapacitors in literature.

3.4 Conclusions

In conclusion, all-solid-state stretchable sandwich-like pseudocapacitors with stable electrochemical and mechanical performance were fabricated. The results indicate that the sandwich-like structure approach to design stretchable electrodes deserves considerable attention on stretchable pseudocapacitors. This stretchable pseudocapacitor based on the sandwich CNT/MnO_2-FCNT/CNT configuration

overcomes the limitation of the maximum loading of active pseudo-capacitive materials. This component-level design paves the way for the potential application of stretchable pseudocapacitors in wearable and implantable electronic devices.

REFERENCES

1 Gu, T.; Wei, B. Fast and Stable Redox Reaction of MnO_2/CNT Hybrid Electrodes for Dynamically Stretchable Pseudocapacitors. *Nanoscale* **2015**, *7*, 11626–11632.

2 Hu, L.; Pasta, M.; Mantia, F. La; Cui, L.; Jeong, S.; Deshazer, H. D.; Choi, J. W.; Han, S. M.; Cui, Y. Stretchable, Porous, and Conductive Energy Textiles. *Nano Lett.* **2010**, *10*, 708–714.

3 Wang, C.; Zheng, W.; Yue, Z.; Too, C. O.; Wallace, G. G. Buckled, Stretchable Polypyrrole Electrodes for Battery Applications. *Adv. Mater.* **2011**, *23*, 3580–3584.

4 Xu, S.; Zhang, Y.; Cho, J.; Lee, J.; Huang, X.; Jia, L.; Fan, J. a; Su, Y.; Su, J.; Zhang, H.; Cheng, H.; Lu, B.; Yu, C.; Chuang, C.; Kim, T.-I.; Song, T.; Shigeta, K.; Kang, S.; Dagdeviren, C.; Petrov, I.; Braun, P. V; Huang, Y.; Paik, U.; Rogers, J. a. Stretchable Batteries with Self-Similar Serpentine Interconnects and Integrated Wireless Recharging Systems. *Nat. Commun.* **2013**, *4*, 1543.

5 Kaltenbrunner, M.; Kettlgruber, G.; Siket, C.; Schwödiauer, R.; Bauer, S. Arrays of Ultracompliant Electrochemical Dry Gel Cells for Stretchable Electronics. *Adv. Mater.* **2010**, *22*, 2065–2067.

6 Cao, Z.; Wei, B. Fragmented Carbon Nanotube Macrofilms as Adhesive Conductors for Lithium-Ion Batteries. *ACS Nano* **2014**, *8*, 3049–3059.

7 Liu, W.-W.; Feng, Y.-Q.; Yan, X.-B.; Chen, J.-T.; Xue, Q.-J. Superior Micro-Supercapacitors Based on Graphene Quantum Dots. *Adv. Funct. Mater.* **2013**, *23*, 4111–4122.

8 Xu, P.; Gu, T.; Cao, Z.; Wei, B.; Yu, J.; Li, F.; Byun, J.-H.; Lu, W.; Li, Q.; Chou, T.-W. Carbon Nanotube Fiber Based Stretchable Wire-Shaped Supercapacitors. *Adv. Energy Mater.* **2014**, *4*, 1300759.

9 Xie, K.; Wei, B. Materials and Structures for Stretchable Energy Storage and Conversion Devices. *Adv. Mater.* **2014**, *26*, 3592–3617.

10 Yu, C.; Masarapu, C.; Rong, J.; Wei, B.; Jiang, H. Stretchable Supercapacitors Based on Buckled Single-Walled Carbon-Nanotube Macrofilms. *Adv. Mater.* **2009**, *21*, 4793–4797.

11 Niu, Z.; Dong, H.; Zhu, B.; Li, J.; Hong, H. H.; Zhou, W.; Chen, X.; Xie, S. Highly Stretchable, Integrated Supercapacitors Based on Single-Walled Carbon Nanotube Films with Continuous Reticulate Architecture. *Adv. Mater.* **2013**, *25*, 1058–1064.

12 Niu, Z.; Zhou, W.; Chen, J.; Feng, G.; Li, H.; Hu, Y.; Ma, W.; Dong, H.; Li, J.; Xie, S. A Repeated Halving Approach to Fabricate Ultrathin Single-Walled Carbon Nanotube Films for Transparent Supercapacitors. *Small* **2013**, *9*, 518–524.

13 Kaempgen, M.; Chan, C. K.; Ma, J.; Cui, Y.; Gruner, G. Printable Thin Film Supercapacitors Using Single-Walled Carbon Nanotubes. *Nano Lett.* **2009**, *9*, 1872–1876.

14 Yue, B.; Wang, C.; Ding, X.; Wallace, G. G. Polypyrrole Coated Nylon Lycra Fabric as Stretchable Electrode for Supercapacitor Applications. *Electrochim. Acta* **2012**, *68*, 18–24.

15 Yin, Y.; Liu, C.; Fan, S. Well-Constructed CNT mesh/PANI Nanoporous Electrode and Its Thickness Effect on the Supercapacitor Properties. *J. Phys. Chem. C* **2012**, *116*, 26185–26189.

16 Meng, C.; Liu, C.; Fan, S. Flexible Carbon Nanotube/polyaniline Paper-like Films and Their Enhanced Electrochemical Properties. *Electrochem. Commun.* **2009**, *11*, 186–189.

17 Zhang, Z.; Wang, W.; Li, C.; Wei, L.; Chen, X.; Tong, Y.; Mai, K.; Lu, X. Highly Conductive Ethylene-Vinyl Acetate Copolymer/Carbon Nanotube Paper for Lightweight and Flexible Supercapacitors. *J. Power Sources* **2014**, *248*, 1248–1255.

18 Chen, P. C.; Shen, G.; Sukcharoenchoke, S.; Zhou, C. Flexible and Transparent Supercapacitor Based on In_2O_3 Nanowire/Carbon Nanotube Heterogeneous Films. *Appl. Phys. Lett.* **2009**, *94*, 2007–2010.

19 Cheng, Y.; Lu, S.; Zhang, H.; Varanasi, C. V.; Liu, J. Synergistic Effects from Graphene and Carbon Nanotubes Enable Flexible and Robust Electrodes for High-Performance Supercapacitors. *Nano Lett.* **2012**, *12*, 4206–4211.

Chapter 4

STRETCHABLE ASYMMETRIC SUPERCAPACITORS BASED ON WRINKLED MANGANESE DIOXIDE/CARBON NANOTUBE AND IRON OXIDE/CARBON NANOTUBE

4.1 Introduction

As we have illustrated in chapter 3, stretchable pseudocapacitors with the high mass loading of pseudo-capacitive materials have been achieved.[1] However, such pseudocapacitors still suffer from low working potentials (usually less than 1 V), leading to unsatisfied energy and power densities, preventing them from practical applications. Therefore, it is imperative to develop another valid approach to enhance the electrochemical performance, while maintaining their high mechanical stretchability.

The asymmetric electrode configuration, taking advantage of the pseudo-capacitive positive electrodes to improve the specific capacitance as well as the carbon-based negative electrodes to extend the operating potential, has been demonstrated as an effective way for improving the supercapacitor electrochemical performance.[2-5] The higher operating voltage can not only enhance the energy density but also, reduce the number of capacitors in series to achieve an expected output voltage. Lately, asymmetric electrode configuration has been applied to the newly emerged flexible supercapacitors, such as MnO_2//carbon or graphene,[3-5] graphene//CNT,[6] graphene-RuO_2//graphene,[2,7] and graphene-$Ni(OH)_2$//graphene,[8] but most of these flexible asymmetric supercapacitor prototypes are only capable of

bending but not stretching. The simple bendability sustaining the induced strains ≤ 1% is far insufficient for practical where the devices would experience more complicated and challenging stretching, which must adjust a large strain deformation >>1%.

Transition metal oxides dominate the pseudo-capacitive materials for electrochemical energy storage. As an example, MnO_2 has significant predominance such as abundance, low cost, and a high theoretical specific capacitance (1370 F g^{-1}).[9] Fe_2O_3 has the advantage of low cost and environmental harmlessness and shows a superior electrochemical performance in negative potentials.[10] Therefore, asymmetric supercapacitors composed of MnO_2 as the positive electrode and Fe_2O_3 as the negative electrode will become a promising energy storage candidate that possesses more economical and environmental superiority. Besides, the redox reaction process of the typically pseudo-capacitive materials has been found to be extremely fast owing to the strong bonded, inherently superior conductive, and porous CNT films.[11] In light of this, different from using sole carbon-based materials as a negative electrode in previously reported asymmetric supercapacitors,[3-8] we focused on enhancing the specific capacitance and energy density of asymmetric supercapacitors using metal oxide electrodes in both electrodes in this chapter's work.

Herein, an asymmetric stretchable supercapacitor (ASS) with the MnO_2/CNT hybrid film as the positive electrode and the Fe_2O_3/CNT composite film as the negative electrode, and Na_2SO_4/PVA gel electrolyte has been fabricated. The ASS cell with the stretchability of up to 100% possesses a high potential window of 2 V, a high energy density (45.8 Wh kg^{-1}), and high electrochemical and mechanical cycling stability. To the best of our knowledge, this is the first report of a novel asymmetric

stretchable energy storage system based on two metal oxides/CNT electrodes, which shows simultaneously excellent electrochemical performance and high stretchability.

4.2 Experimental

4.2.1 ASS assembly

The precursor, a mixture of ferrocene and sulfur (atomic ratio Fe:S =1:10, both from Sigma-Aldrich), was heated to 1150 °C in the tube furnace with a mixed gas flow of Ar (1500 mL min^{-1}) and H_2 (150 mL min^{-1}). After 30 min reaction, the as-obtained unpurified CNT films were transferred into a ceramic cubicle to be heat-treated at 450 °C in the air for 30 min. The samples were then cooled down, and the Fe_2O_3/CNT films were obtained. MnO_2/CNT films were prepared by using Chapter 2's method.

The as-prepared Fe_2O_3/CNT and MnO_2/CNT films were laminated tightly with a UV-light treated pre-stretched PDMS substrate. The stretchable electrodes were then stretched to 100% strain. Subsequently, the liquid Na_2SO_4/PVA gel electrolyte was coated on the surface of electrodes by means of dip coating, leaving the uncoated part to be connected to current collectors. One MnO_2/CNT and the other Fe_2O_3/CNT film were then stacked together with the electrolyte-coated parts overlapping with each other. The assembled ASS was placed in the fume hood under ambient conditions to allow the gel electrolyte to solidify.

4.2.2 Calculations

The specific capacitance of ASS was calculated based on the total mass of both positive and negative electrodes (0.33mg).

4.3 Results and Discussion

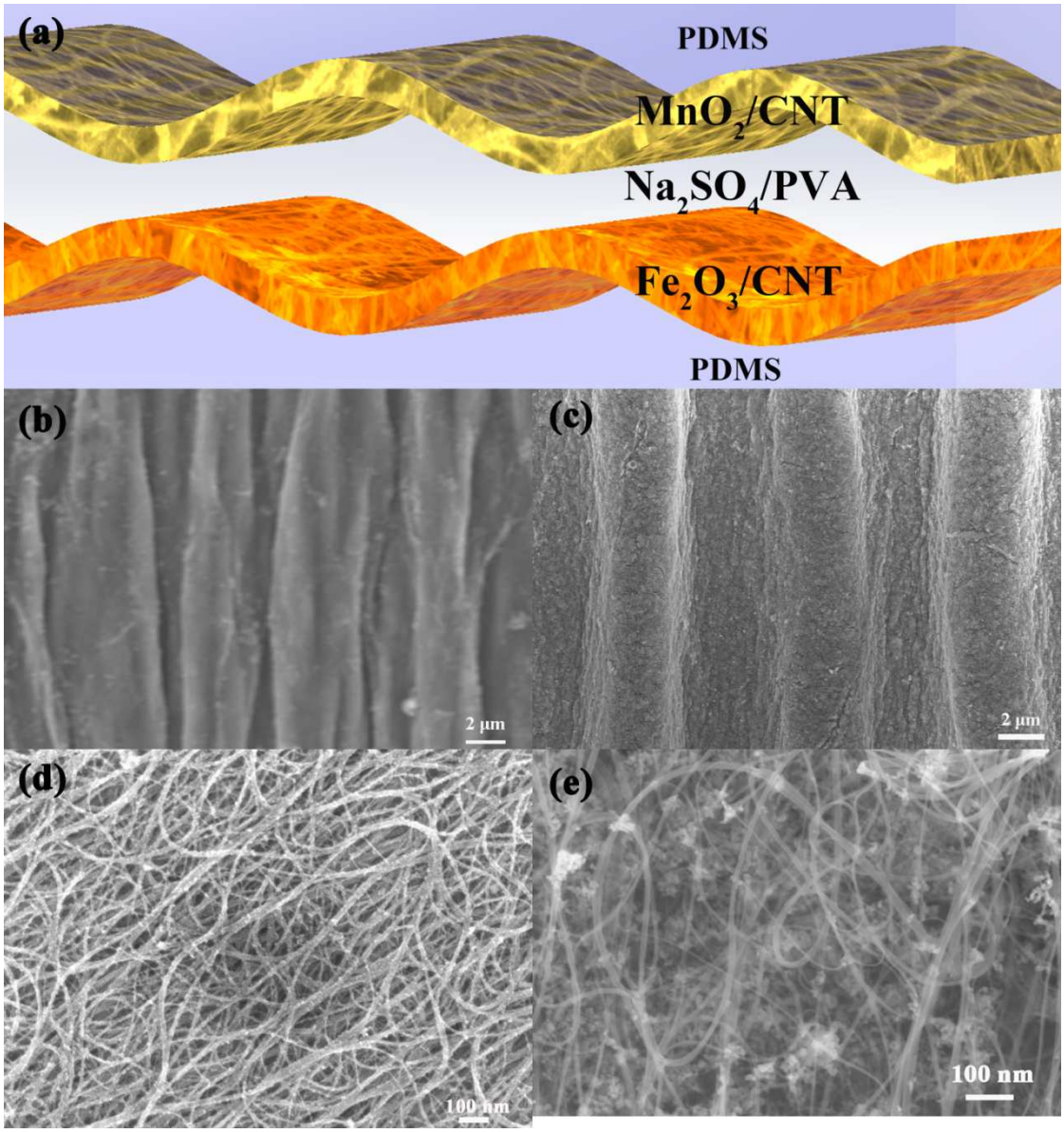

Figure 4.1 (**a**) Schematic illustration of the fabricated ASS cell based on the wrinkled MnO_2/CNT hybrid film as a positive electrode and Fe_2O_3/CNT hybrid film as a negative electrode; SEM images of the wrinkled MnO_2/CNT film (**b**) and Fe_2O_3/CNT film (**c**). Magnified SEM images of the MnO_2/CNT film (**d**) and Fe_2O_3/CNT film (**e**).

To fabricate the ASS cell, the MnO_2/CNT film, Fe_2O_3/CNT film, and Na_2SO_4/PVA gel electrolyte were used as the positive electrode, negative electrode, and electrolyte, respectively (Figure 4.1a). The ASS was made stretchable by applying the simple pre-straining-then-buckling strategy.[12,13] In brief, a custom-made, two-way movable stage was utilized to pre-stretch a PDMS substrate (with 100% pre-strain); the freestanding MnO_2/CNT and Fe_2O_3/CNT films were then attached and secured to the PDMS substrate, respectively. Subsequently, a liquid Na_2SO_4/PVA gel electrolyte was coated on the surface of electrodes by means of the dip coating. After the electrolyte had solidified, two electrodes were stacked together with the electrolyte-coated parts overlapping. Finally, the pre-strain was released to its original length to form the "wavy" structure. The SEM images of the wrinkled MnO_2/CNT and Fe_2O_3/CNT films are shown in Figure 4.1b and 4.1c, respectively. The precipitated MnO_2 particles and as-synthesized Fe_2O_3 particles were demonstrated to possess nanoscale architectures and evenly distributed with CNT bundles (Figure 4.1d and 4.1e).

To identify the potential window of the asymmetric supercapacitor and balance the charges between the positive and negative electrodes, the electrochemical performance of the hybrid MnO_2/CNT and Fe_2O_3/CNT electrodes was investigated in a three-electrode system using platinum foil, Ag/AgCl, and 1 M Na_2SO_4 aqueous solution as the counter electrode, reference electrode, and electrolyte, respectively. The MnO_2/CNT electrode shows a stable potential window of 0 ~ 1.2 V, while the Fe_2O_3/CNT electrode exhibits the stable operation in the range of - 0.8 ~ 0 V, indicating that the potential window of the assembled asymmetric supercapacitor can be potentially extended to 2 V, as shown in Figure 4.2a. At the scan rate of 50 mV s^{-1},

the specific capacitance of the MnO_2/CNT positive electrode and Fe_2O_3/CNT negative electrode are 130.2 and 129.1 F g^{-1}, respectively. The charge balance between the two electrodes follows the relationship $Q_+ = Q_-$, in which the stored charge by each electrode is determined by the specific capacitance (C), the potential window (ΔU), and the mass (m) of each electrode using the following equation 4.1:

$$Q = C * \Delta U * m \qquad (4.1)$$

Based on this calculation, the optimal mass ratio between the two electrodes should be around $m_{MnO2/CNT}/m_{Fe2O3/CNT}$ = 0.66.

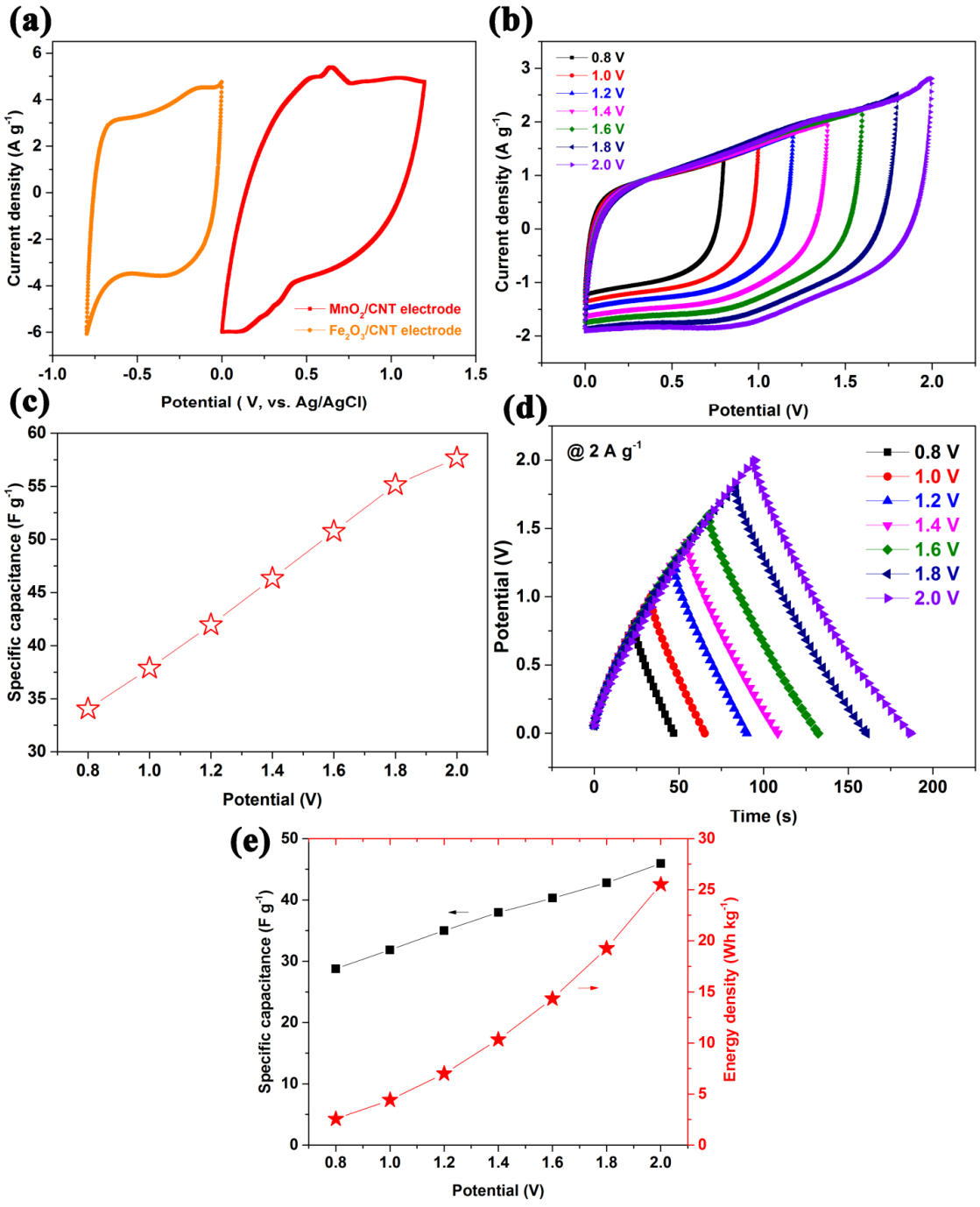
(a)
Current density (A g-1)
Potential (V, vs. Ag/AgCl)
MnO2/CNT electrode
Fe2O3/CNT electrode
(b)
Current density (A g-1)
Potential (V)
0.8 V
1.0 V
1.2 V
1.4 V
1.6 V
1.8 V
2.0 V
(c)
Specific capacitance (F g-1)
Potential (V)
(d)
@ 2 A g-1
Potential (V)
Time (s)
0.8 V
1.0 V
1.2 V
1.4 V
1.6 V
1.8 V
2.0 V
(e)
Specific capacitance (F g-1)
Energy density (Wh kg-1)
Potential (V)

Figure 4.2 (**a**) Comparative CV curves of MnO_2/CNT and Fe_2O_3/CNT electrodes performed in a three-electrode cell in 1 M Na_2SO_4 aqueous solution at a scan rate of 50 mV s^{-1}. (**b**) CV curves of an optimized MnO_2/CNT and Fe_2O_3/CNT asymmetric supercapacitor measured at different potential windows at a scan rate of 50 mV s^{-1}. (**c**) Specific capacitances of the ASS with the increase of potential window in Na_2SO_4/PVA at a scan rate of 50 mV s^{-1}. (**d**) GCD curves obtained over different voltages from 0.8 to 2 V at a current density of 2 A g^{-1}. (**e**) Effects of the extended potential window on the specific capacitance and energy density.

CV curves of the ASS cell at 50 mV s^{-1} within different potential windows are displayed in Figure 4.2b. When the potential window is increased up to 2 V, the rectangular shape of the CV curves with two weak symmetric broad redox peaks and the symmetric shape are maintained, indicating a good capacitive behavior. The weak broad redox peaks are attributed to the pseudo-capacitive behavior of the supercapacitor resulted from the Faradaic reactions of MnO_2 and Fe_2O_3. Figure 4.2c exhibits the potential window dependence of the specific capacitance of the asymmetric supercapacitor. The specific capacitance increases significantly from 34 to 57.7 F g^{-1} with the operation potential from 0.8 to 2 V, meaning that the stored energy can be improved at least by 961% according to equation 4.2:

$$E = \frac{1}{2} * \mathrm{C} * U^2. \qquad (4.2)$$

As a result, the overall performance of the supercapacitor is greatly improved. Note that operating at a higher voltage can provide an additional advantage for practical applications, by reducing the number of devices in series required to reach the desired output voltage.

Similarly, GCD was also carried out at 2 A g^{-1} with different cell voltages from 0.8 to 2 V (Figure 4.2d), and no overcharge curve was observed, inferring an excellent supercapacitor performance. The GCD result also shows an increase in charging and

discharging time with increasing the cell voltage, thus indicating the increases of capacitance and energy density. These results also coincide with the CV results. Based on Figure 4.2d, the effects of extending potential window on specific capacitance and energy density are calculated and depicted in Figure 4.2e. While the specific capacitance starts to increase slightly from 28.7 F g^{-1} at 0.8 V to 45.9 F g^{-1} at 2 V, the energy density rises significantly, and ten folded from 2.5 to 25.5 Wh kg^{-1} as the potential window is extended from 0.8 to 2 V.

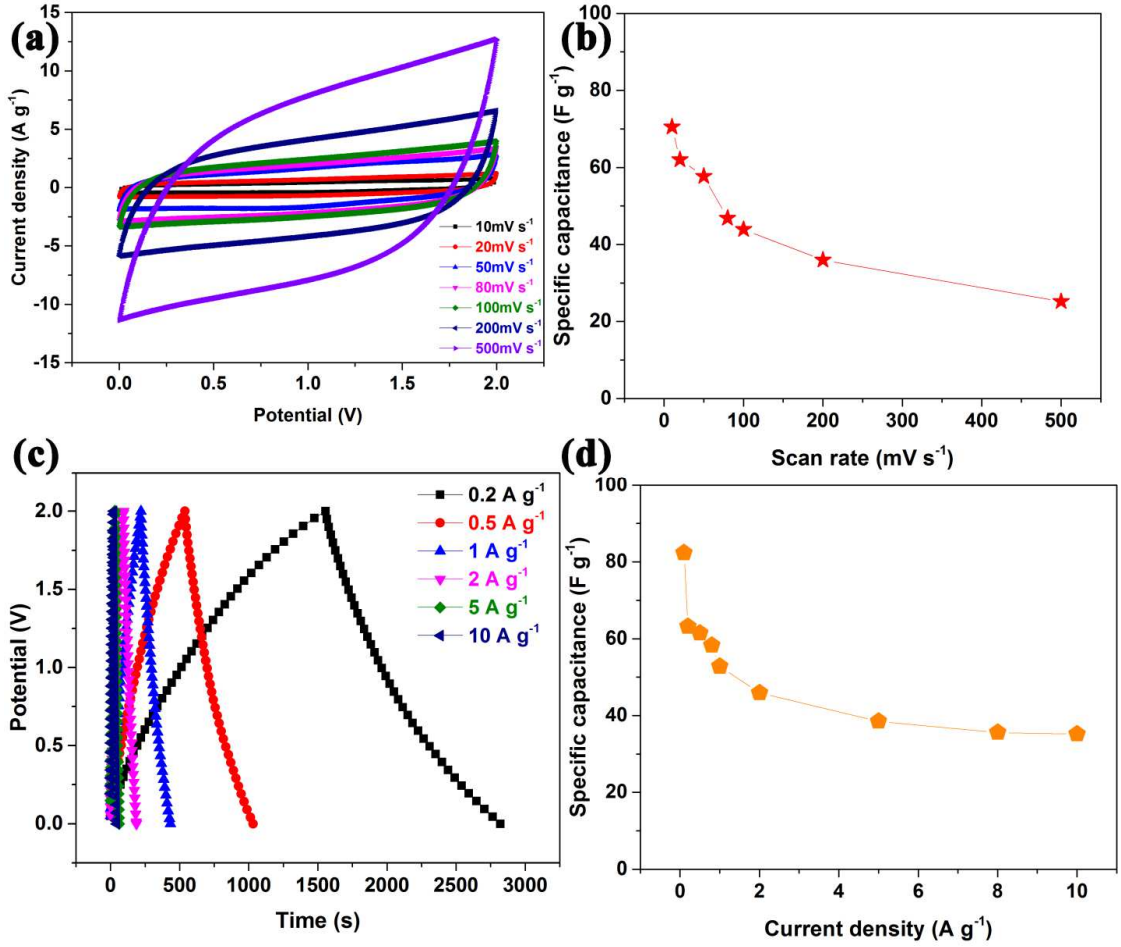

Figure 4.3 (**a**) CV curves of an optimized ASS at scan rates ranging from 10 to 500 mV s^{-1}. (**b**) The scan rate dependence of specific capacitance. (**c**) GCD curves collected at different current densities for the ASS cell operated within a voltage window from 0 to 2 V. (**d**) Specific capacitance variation with current density.

Figure 4.3a exhibits CV curves of an optimized ASS cell measured at different scan rates of 10, 20, 50, 80, 100, 200, and 500 mV s^{-1} between 0 and 2 V. The CV profiles retain a relatively rectangular shape without obvious distortion with increasing the scan rate, even at a high scan rate of 500 mV s^{-1}, indicating the desirable fast charge/discharge property of the power device. As shown in Figure 4.3b, the specific

capacitance gradually decreases with the increase of scan rates. It is understandable that at the high scan rates, ionic diffusions of Na^+ ions are most likely limited due to the time constraint, and only the outer active surface is utilized for the charge storage, resulting in a low electrochemical utilization of the electroactive materials. It is worth noting that the specific capacitance was calculated using the total mass of the two electrodes in the asymmetric supercapacitor, rather than a single electrode. More importantly, the maximum specific capacitance reaches 125.3 F g^{-1} at 1 mV s^{-1}, which is almost twice of graphene//CNT asymmetric flexible supercapacitors[6] and CNT//CNT, MnO_2/CNT//MnO_2/CNT symmetrical stretchable or flexible supercapacitors.[12,13] The exceptional performances of the ASS cell are ascribed to the high capacitance and rate performance of both MnO_2/CNT and Fe_2O_3/CNT composites. Besides, the superior performance is further confirmed by GCD measurements at different current densities. As shown in Figure 4.3c, the charge and discharge curves of the ASS device are reasonably symmetric. This further demonstrates the ideal capacitive characteristic and rapid charge-discharge property of the ASS cell. The specific capacitance calculated based on the discharge curves is 82.4 F g^{-1} (87% coulomb efficiency) at 100 mA g^{-1} (Figure 4.3d), which is substantially higher than the values obtained from recent reports for other flexible supercapacitors.[6,14]

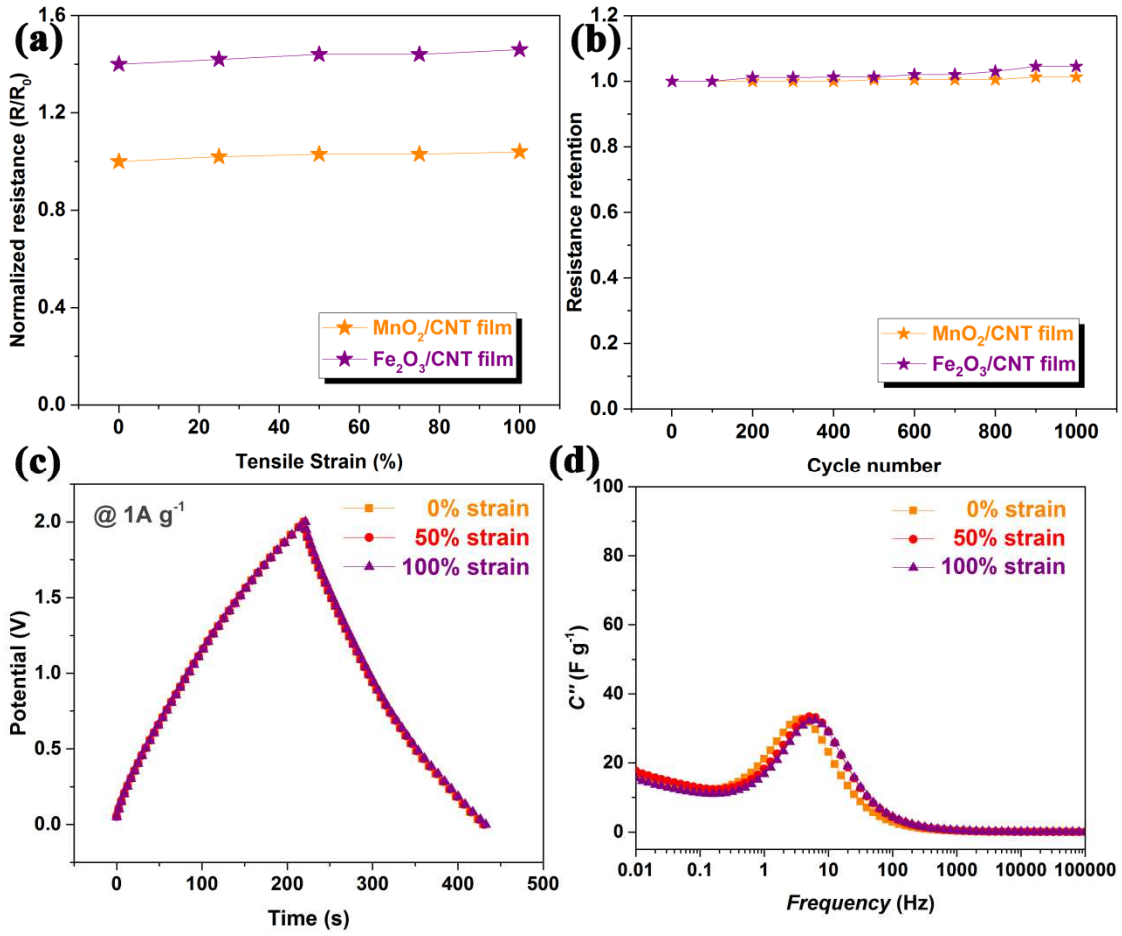

Figure 4.4 (**a**) Normalized resistance versus tensile strain of wrinkled MnO_2/CNT and Fe_2O_3/CNT films subjected to tensile strains up to 100%. (**b**) Resistance retention as a function of 1000 repeated stretching-releasing cycles between 0 to 100% strain. (**c**) Comparison of GCD electrochemical performance of ASS with 0, 50, and 100% strains at 1 A g^{-1}. (**d**) Bode plots of imaginary specific capacitance related to the relaxation time constant at 0, 50, and 100% strains.

To demonstrate the stretchability of the ASS cell, a series of electrical and electrochemical tests were performed. Figure 4.4a shows the normalized resistance at different strain levels, where R_0 is the resistance of the unstretched MnO_2/CNT electrode. Although the resistance of the Fe_2O_3/CNT electrode is ~ 15% higher than

that of MnO_2/CNT, the conductivity of both MnO_2/CNT and Fe_2O_3/CNT electrodes did not vary much (less than 5%) with the increase of tensile strain up to 100%. In other words, without changing the original film length while stretching, the wrinkled MnO_2/CNT and Fe_2O_3/CNT films accommodate the applied tensile strains by adjusting the buckling structure, resulting in nearly constant resistance.

The wrinkled MnO_2/CNT and Fe_2O_3/CNT composite films were further used to explore the resistance stability and mechanical durability during the mechanically dynamic processes between 0 and 100% strain, respectively. It should be noted that the resistance shows a small increment of < 4% after 1000 DSR cycles for both hybrid films subjected to a high strain rate of 10% strain per second (Figure 4.4b), which demonstrates an excellent mechanical robustness of the wrinkled MnO_2/CNT and Fe_2O_3/CNT films.

Similarly, in the electrochemical performance of the ASS device, the slopes of discharge curves in Figure 4.4c maintain approximately constant as the supercapacitor deformed at different tensile strains (0%, 50%, and 100%), indicating slight capacitance change. The excellent stretchability and electrochemical stability are due to the high interfacial strength to accommodate the various materials with different properties.

The relaxation time from Figure 4.4d in the frequency-dependent imaginary capacitance analysis quantitatively reveals its performance. From the C'' plot, it is observed that the overall frequency response of the cell from 0.01 Hz to 100k Hz in a relaxed and a stretched state are almost the same. The stable behavior under the tensile strains from 0, 50, and 100% is in good agreement with the GCD results in Figure 4.4c. τ^0 is less than 0.25 s at all strains. This extremely short relaxation time could be

attributed to the excellent conductivity of the CNT films, which facilitate MnO_2 and Fe_2O_3 redox reactions and lead to rapid capacitive behavior. This extremely small relaxation time constant τ_0 at different strains also strongly suggests that the ASS device possesses the tremendous potential for stable and instantaneous delivery of ultra-high power and energy under extreme mechanical deformation.

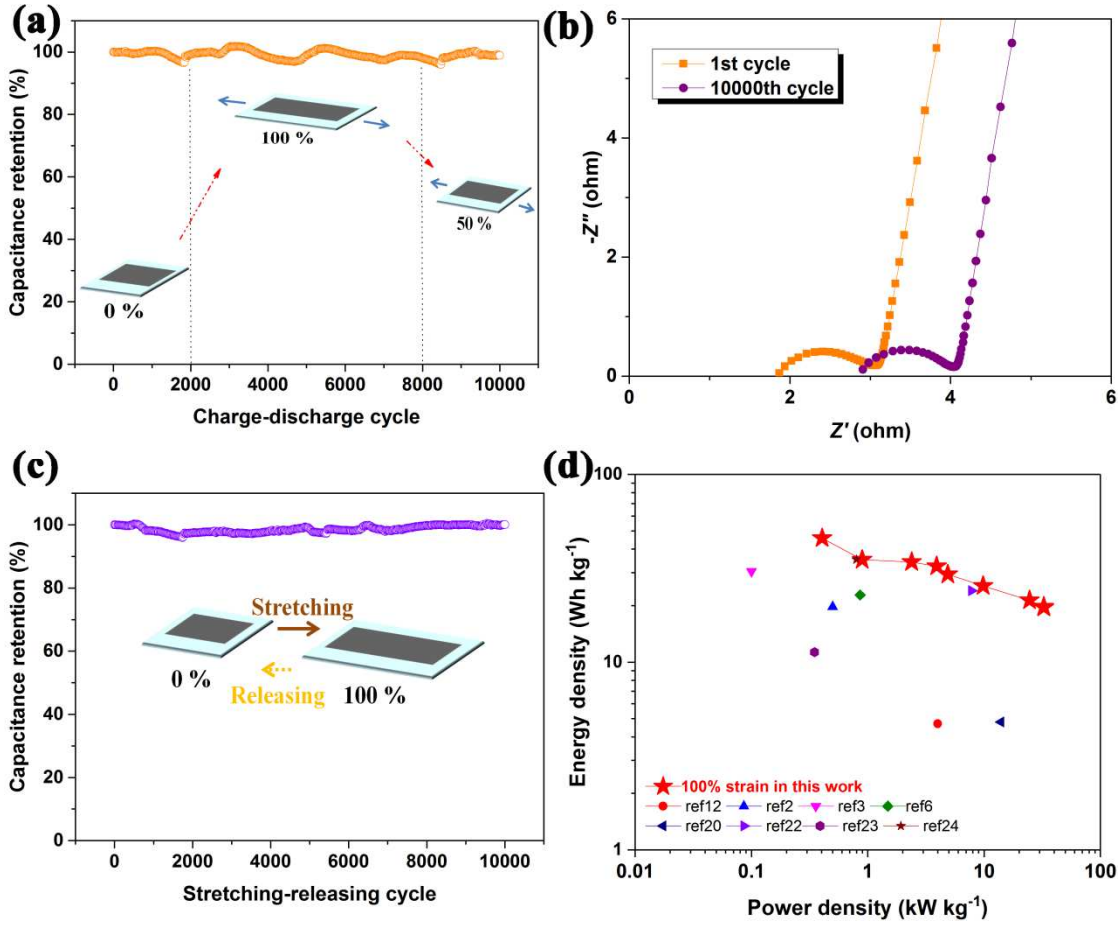

Figure 4.5 (**a**) Long cycling stability of the ASS cell under 0%, 100%, and 50% strains at the constant current density of 1 A g^{-1} over 10000 cycles. (**b**) Nyquist plots of the ASS cell in the frequency range of 100 kHz to 0.01 Hz measured after 1st and 10000th cycle. (**c**) 10000 mechanical stretching-releasing cycles between 0 and 100% strain at 10% strain per second at the current density of 1 A g^{-1}. (**d**) Ragone plot of ASS at 100% strain and comparison with other flexible and stretchable asymmetric supercapacitors in literature.

Long cycling life is an essential requirement for stretchable energy storage devices. The cycling life test for the ASS cell was carried out by repeating the GCD test between 0 and 2 V at a current density of 1 A g^{-1} for 10000 cycles. Figure 4.5a

shows the capacitance retention of the ASS cell charged between 0 and 2V as a function of the electrochemical cycle number. It is worth noting that the ASS cell is at 0% strain for the beginning 2000 GCD cycles and then strained to 100% from the 2001st cycle to the 8000th cycle, and finally at 50% strain for the rest 2000 GCD cycles. The ASS cell exhibits outstanding electrochemical stability with only 1.1% deterioration of the initial specific capacitance after 10000 GCD cycles. Therefore, the retention of 98.9% after 10000 cycles for the ASS is comparable to those of other recently reported asymmetric supercapacitors without any stretchability, such as Graphene/MnO_2//activated carbon (AC) (97% retention after 1000 cycles),[15] MnO_2/graphene//Graphene (79% retention after 1000 cycles),[3] and $Ni(OH)_2$//AC (94.3% retention after 3000 cycles).[8] These results further indicate that the ASS possesses not only exceptional electrochemical performance but also excellent stretchability.

For further understanding, the impedance of the asymmetric supercapacitor after the 1st and 10000th cycle was measured in the frequency range of 100 kHz to 0.01 Hz at open circuit potential with an AC perturbation of 10 mV (Figure 4.5b). After 10000 cycles, nearly no change is observed for *Rct* (1.1 Ω), and only a slight increase of *Rs* from 1.9 to 2.9 Ω is observed. These EIS results further demonstrate the exceptional electrochemical stability of the ASS cell.

The ASS can also be expected to accommodate volumetric expansion of MnO_2 and Fe_2O_3 during charge-discharge cycles due to highly conducting nature of the CNT framework in the composites. However, volumetric expansion effect can be further enlarged during stretching and release when a portion of the MnO_2 and Fe_2O_3 nanoparticles will have the potential to migrate more easily with dynamic mechanical shock. This was verified by testing the attainable mechanical stretching-releasing

cycles, which reveal device durability for practical applications and are also very critical in addition to evaluating their long GCD cycling stability. The ASS cell was tested for 10000 DSR cycles with a strain rate of 10% per second at a constant current density of 1 A g^{-1}. Figure 4.5c shows that the capacitance retention is extremely high where the capacitance fades by merely less than 1%, further proving the excellent durability of the ASS cell from the mechanical viewpoint. It is apparent that MnO_2 and Fe_2O_3 nanoparticles are still firmly anchored on the surface of CNTs and agglomerated at the crossing of nanotubes, although experiencing the volumetric variations generated by the electrochemical processes and the mechanical shock at the same time. Such good cycle performance is comparable with that of other stretchable supercapacitors and is highly promising for practical applications.[11-13,16]

The energy density reaches 45.8 Wh kg^{-1} at a power density of 406.6 W kg^{-1} and remains 19.6 Wh kg^{-1} at a power density of 32.7 kW kg^{-1} (Figure 4.5d). The specific energy density values achieved with a cell voltage of 2 V in this work are much higher than those of recently reported flexible/stretchable symmetrical CNT//CNT supercapacitor (< 12.5 Wh kg^{-1}),[12,13,17,18] graphene//graphene supercapacitor (< 26 Wh kg^{-1})[19], MnO_2//MnO_2 supercapacitors (< 4.8 Wh kg^{-1})[20], and polypyrrole/CNT supercapacitors (< 32.7 Wh kg^{-1})[21]. It is also better than existing asymmetric flexible supercapacitors with an aqueous electrolyte, such as RuO_2/Graphene//Graphene (19.7 Wh kg^{-1})[2], MnO_2/Graphene//Graphene (30.4 Wh kg^{-1})[12], MnO_2/CNT//CNT (6.0 Wh kg^{-1})[6], Graphene/MnO_2/CNT//AC/CNT (24 Wh kg^{-1})[22], Bi_2O_3//MnO_2 (11.3 Wh kg^{-1})[23], and Co_2AlO_4@MnO_2//Fe_3O_4 (35.2 Wh kg^{-1})[24]. Thus, it is evident that the as-assembled MnO_2/CNT//Fe_2O_3/CNT asymmetric stretchable supercapacitor displays excellent energy performance and shows an

attractive potential for practical applications. The superior electrochemical performance of ASS can be attributed to the following aspects: (1) The CNT films in the composites assist in maintaining mechanical integrity and high electrical conductivity of the overall electrodes due to their superior mechanical properties, good electrochemical stability, and excellent conductivity. (2) Well-dispersed MnO_2 nanoparticles can significantly shorten the diffusion and migration paths of electrolyte ions during the rapid charge-discharge process; accordingly, high electrochemical utilization of MnO_2 is ensured. (3) The carbon-based anodes usually limit the energy density of the asymmetric supercapacitors due to their relative lower specific capacitance. The present Fe_2O_3/CNT composite exhibits improved specific capacitance due to the synergetic effect of highly conductive CNT providing fast electron transfer and large surface area and well-dispersed Fe_2O_3 nanoparticles contributing large pseudocapacitance. The large specific capacitance of the present Fe_2O_3/CNT composite is comparable with that of the MnO_2/CNT composite, making the desirable anode-cathode coupling build a 2 V asymmetric supercapacitor with both high energy density and power density. (4) The binder-free device fabrication enables a low interfacial resistance and fast electrochemical reaction rate.

4.4 Conclusions

In conclusion, an all-solid-state asymmetric stretchable supercapacitor based on the MnO_2/CNT hybrid film positive electrode, Fe_2O_3/CNT composite film negative electrode, and the solid state Na_2SO_4/PVA gel electrolyte was fabricated. Due to the good conductivity of the CNT films and the extended potential window of 2 V, the specific capacitance and the energy density were greatly enhanced. In addition to the excellent electrochemical performance, the remarkable stretchability of up to 100%

tensile strain made this supercapacitor a promising energy storage device for practical applications. The asymmetric configuration has been demonstrated to be the preferable stretchable supercapacitor structure to achieve a higher operating voltage and high energy density without sacrificing the power delivery and cycle stability.

REFERENCES

1 Gu, T.; Wei, B. All-Solid-State Stretchable Pseudocapacitors Enabled by Carbon Nanotube Film-Capped Sandwich-like Electrodes. *ACS Appl. Mater. Interfaces* **2016**, *8*, 25243–25250.

2 Choi, B. G.; Chang, S.-J.; Kang, H.-W.; Park, C. P.; Kim, H. J.; Hong, W. H.; Lee, S.; Huh, Y. S. High Performance of a Solid-State Flexible Asymmetric Supercapacitor Based on Graphene Films. *Nanoscale* **2012**, *4*, 4983.

3 Wu, Z. S.; Ren, W.; Wang, D. W.; Li, F.; Liu, B.; Cheng, H. M. High-Energy MnO2 Nanowire/graphene and Graphene Asymmetric Electrochemical Capacitors. *ACS Nano* **2010**, *4*, 5835–5842.

4 Kang, Y. J.; Chung, H.; Kim, W. 1.8-V Flexible Supercapacitors with Asymmetric Configuration Based on Manganese Oxide, Carbon Nanotubes, and a Gel Electrolyte. *Synth. Met.* **2013**, *166*, 40–44.

5 Lei, Z.; Zhang, J.; Zhao, X. S. Ultrathin MnO2 Nanofibers Grown on Graphitic Carbon Spheres as High-Performance Asymmetric Supercapacitor Electrodes. *J. Mater. Chem.* **2012**, *22*, 153.

6 Liu, J.; Zhang, L.; Wu, H. Bin; Lin, J.; Shen, Z.; Lou, X. W. (David). High-Performance Flexible Asymmetric Supercapacitors Based on a New Graphene Foam/carbon Nanotube Hybrid Film. *Energy Environ. Sci.* **2014**, *7*, 3709–3719.

7 Wang, H.; Liang, Y.; Mirfakhrai, T.; Chen, Z.; Casalongue, H. S.; Dai, H. Advanced Asymmetrical Supercapacitors Based on Graphene Hybrid Materials. *Nano Res.* **2011**, *4*, 729–736.

8 Yan, J.; Fan, Z.; Sun, W.; Ning, G.; Wei, T.; Zhang, Q.; Zhang, R.; Zhi, L.; Wei, F. Advanced Asymmetric Supercapacitors Based on $Ni(OH)_2$/graphene and Porous Graphene Electrodes with High Energy Density. *Adv. Funct. Mater.* **2012**, *22*, 2632–2641.

9 Wei, W.; Cui, X.; Chen, W.; Ivey, D. G. Manganese Oxide-Based Materials as Electrochemical Supercapacitor Electrodes. *Chem. Soc. Rev.* **2011**, *40*, 1697–1721.

10 Qu, Q.; Yang, S.; Feng, X. 2D Sandwich-like Sheets of Iron Oxide Grown on Graphene as High Energy Anode Material for Supercapacitors. *Adv. Mater.* **2011**, *23*, 5574–5580.

11 Gu, T.; Wei, B. Fast and Stable Redox Reaction of MnO_2/CNT Hybrid Electrodes for Dynamically Stretchable Pseudocapacitors. *Nanoscale* **2015**, *7*, 11626–11632.

12 Yu, C.; Masarapu, C.; Rong, J.; Wei, B.; Jiang, H. Stretchable Supercapacitors Based on Buckled Single-Walled Carbon-Nanotube Macrofilms. *Adv. Mater.* **2009**, *21*, 4793–4797.

13 Li, X.; Gu, T.; Wei, B. Dynamic and Galvanic Stability of Stretchable Supercapacitors. *Nano Lett.* **2012**, *12*, 6366–6371.

14 He, Y.; Chen, W.; Li, X.; Zhang, Z.; Fu, J.; Zhao, C.; Xie, E. Freestanding Three-Dimensional graphene/Mno2 Composite Networks as Ultralight and Flexible Supercapacitor Electrodes. *ACS Nano* **2013**, *7*, 174–182.

15 Fan, Z.; Yan, J.; Wei, T.; Zhi, L.; Ning, G.; Li, T.; Wei, F. Asymmetric Supercapacitors Based on Graphene/MnO2 and Activated Carbon Nanofiber Electrodes with High Power and Energy Density. *Adv. Funct. Mater.* **2011**, *21*, 2366–2375.

16 Xie, K.; Wei, B. Materials and Structures for Stretchable Energy Storage and Conversion Devices. *Adv. Mater.* **2014**, *26*, 3592–3617.

17 Niu, Z.; Dong, H.; Zhu, B.; Li, J.; Hng, H. H.; Zhou, W.; Chen, X.; Xie, S. Highly Stretchable, Integrated Supercapacitors Based on Single-Walled Carbon Nanotube Films with Continuous Reticulate Architecture. *Adv. Mater.* **2013**, *25*, 1058–1064.

18 Kaempgen, M.; Chan, C. K.; Ma, J.; Cui, Y.; Gruner, G. Printable Thin Film Supercapacitors Using Single-Walled Carbon Nanotubes. *Nano Lett.* **2009**, *9*, 1872–1876.

19 Zang, J.; Cao, C.; Feng, Y.; Liu, J.; Zhao, X. Stretchable and High-Performance Supercapacitors with Crumpled Graphene Papers. *Sci. Rep.* **2014**, *4*, 6492.

20 Yuan, L.; Lu, X.-H.; Xiao, X.; Zhai, T.; Dai, J.; Zhang, F.; Hu, B.; Wang, X.; Gong, L.; Chen, J.; *et al.* Flexible Solid-State Supercapacitors Based on Carbon nanoparticles/MnO2 Nanorods Hybrid Structure. *ACS Nano* **2012**, *6*, 656–661.

21 Liang, K.; Gu, T.; Cao, Z.; Tang, X.; Hu, W.; Wei, B. In Situ Synthesis of SWNTs@MnO_2/polypyrrole Hybrid Film as Binder-Free Supercapacitor Electrode. *Nano Energy* **2014**, *9*, 245–251.

22 Cheng, Y.; Zhang, H.; Lu, S.; Varanasi, C. V; Liu, J. Flexible Asymmetric Supercapacitors with High Energy and High Power Density in Aqueous Electrolytes. *Nanoscale* **2013**, *5*, 1067–1073.

23 Xu, H.; Hu, X.; Yang, H.; Sun, Y.; Hu, C.; Huang, Y. Flexible Asymmetric Micro-Supercapacitors Based on Bi_2O_3 and MnO_2 Nanoflowers: Larger Areal Mass Promises Higher Energy Density. *Adv. Energy Mater.* **2015**, *5*, 1–7.

24 Li, F.; Chen, H.; Liu, X. Y.; Zhu, S. J.; Jia, J. Q.; Xu, C. H.; Dong, F.; Wen, Z. Q.; Zhang, Y. X. Low-Cost High-Performance Asymmetric Supercapacitors Based on Co_2AlO_4@MnO_2 Nanosheets and Fe_3O_4 Nanoflakes. *J. Mater. Chem. A* **2016**, *4*, 2096–2104.

Chapter 5

ALL-MANGANESE-BASED BINDER-FREE STRETCHABLE LITHIUM-ION BATTERIES

5.1 Introduction

As discussed in the previous chapters, the development of stretchable energy storage devices has been widely studied and focused on increasing specific capacitance of stretchable EDLCs and pseudocapacitors.[1-5] In order to achieve a higher energy density, the lithium-ion battery becomes a necessity. However, there is very few work involving stretchable lithium-ion batteries.[6-8] Rogers et al.[6] reported stretchable lithium-ion batteries by using "serpentine" interconnections; nevertheless, the interconnect structure which contributes to the stretchability results in extremely low areal utility of the devices. Other designs enabling stretchability used the "wavy" or "wire-shaped" structures,[7,8] where active materials are blended with CNT powders by using a polymer binder then on a prestrained elastic substrate. The introduction of the polymer binder is unavoidable to form the electrode but degrades the ion transport capability, inhibits the electrical conductivity, and leads to an obvious capacity loss. It is critical and highly desirable to develop chemical bonding among the constituent materials in electrodes in order to withstand the mechanical stretching-releasing process for stretchable lithium-ion batteries. It is unfortunate that no attention has been paid so far to such a binder-free electrode with chemically bonded components. A binder-free electrode will not only significantly improve the specific capacity of practical lithium-ion batteries and lower the manufacturing costs; but more

importantly, will permanently solve the cycling degradation issue introduced by the stretching-releasing process.

As discussed above, reliable stretchable lithium-ion batteries are underdeveloped. On the one hand, a uniform coating of active materials on CNT scaffolds with chemical bonding toward a high-performance binder-free and stretchable electrode is highly desirable but very challenging. On the other hand, improving the cycling stability of next-generation lithium-ion batteries with low cost, natural abundance, non-toxicity, and high stretchability is also imperative. In Chapter 2 to 4, our previous work indicated that a wrinkled CNT film had shown its great potential as stretchable scaffolds due to its unique characteristics, including high specific surface areas, high electron conductivity, and chemical/mechanical stability. Manganese oxides (MnO_x), which possesses four times greater theoretical specific capacity than graphite and a lower discharge potential, has been successfully incorporated into the CNT film with strong bonds as an anode by our group.[9] While among all the cathode candidates for a lithium-ion battery, the spinel $LiMn_2O_4$ (LMO) has favorable charge storage capacity and is low-cost, highly abundant, and environmentally friendly. In this chapter, we investigated a suitable hydrothermal synthesis realizing the *in-situ* growth of LMO nanocrystals inside three-dimensional CNT films with chemical bonding as stretchable cathode materials for lithium-ion batteries for the first time. The low temperature and annealing-free synthesis environment is also cost-effective and reduces surplus reaction steps. Moreover, the electrode prepared by buckling the LMO/CNT films with PDMS flexible substrates showed its full stretchability. When coupled with a wrinkled MnO_x/CNT film anode, a binder-free all-manganese-based stretchable lithium-ion battery was achieved, which

exhibited a high capacity and stretchability, as well as low cost and environmental friendliness.

5.2 Experimental

5.2.1 Full cell assembly

A modified method was adopted to synthesize LMO/CNT film by referring to the article.[10] All the chemicals in the following were purchased from Sigma-Aldrich and used as received. Solution A was prepared by dissolving 0.22 g lithium hydroxide into 6 ml DI water followed by adding 0.24 ml hydrogen peroxide (30 *wt*%). Then the as-prepared free-standing CNT films were immersed in the solution A for 2 hours. 0.69 g manganese acetate dissolved in 6 ml DI water formed solution B. Solution A and B were blended with 20 ml methanol and stirred for 40 min. Then the resulting black-brownish slurry with CNT film was transferred into a 40 ml Teflon-lined autoclave and hydrothermally reacted at 115 °C for 10 hours. After the reaction was complete, the films were collected and rinsed several times with deionized water and ethanol. Finally, the freestanding LMO/CNT films were dried at room temperature for 12 hours. To assemble a stretchable full battery, the LMO/CNT cathode was coupled with a MnO_x/CNT anode as reported in our previous work.[9] The wrinkled structures were prepared by the pre-strain then buckling method.[1-3] The areal mass loading of LMO/CNT is ~2.4 mg/cm^2.

5.2.2 Characterizations

The morphology and structure were characterized by using focused ion beam microscopy (FIB, Zeiss Auriga 60 FIB/SEM) and transmission electron microscopy (TEM, JEOL JEM-2010F). X-ray diffraction (XRD) patterns were recorded by Philips

X'Pert diffractometer with Cu Kα radiation. X-ray photoelectron spectra (XPS) were acquired using a VG ESCALAB 220I-XL spectrometer. The X-ray source was monochromatic Al Kα (1486.7eV) with a power of 105 W (15 kV, 7 mA). The operating pressure in the main chamber was less than 10^{-8} Torr. Nitrogen isothermal physisorption measurements were carried out using a Micromeritics ASAP 2020 physisorption analyzer. Samples were degassed by heating to 573 K under vacuum for 6 h prior to the measurement. N_2 was adsorbed on samples at 77 K to determine support surface area after cooling. The Brunauer–Emmett–Teller (BET) method was used to calculate the specific surface area from nitrogen adsorption data over the p/p_o range of 0.06 - 0.30. Thermogravimetric analysis (TGA) was carried out on a high-resolution TGA instrument (Mettler-Toledo, SDA851e) from 0 to 800 °C at a heating rate of 10 °C/min in flowing air. GCD tests of the stretchable full cell were carried out between 2.4 and 3.7 V. Cyclic voltammetry was performed by PARSTAT 2273 potentiostat/galvanostat (Princeton Applied Research) with the scan rate of 0.05 mV/s between 3.8 and 4.3 V.

5.3 Results and Discussion

A "grafting" technique by the hydrothermal reaction was used due to the relatively mild reacting environment compared to other methods with rigor conditions.[10,11] From the SEM images in Figure 5.1, the cross section of the well-defined 3D structure of the LMO/CNT films is exposed in the trapezoid trench milled by a focused Ga^+ ion beam (Figure 5.1a). The magnified SEM image (Figure 5.1b) of marked area in Figure 5.1a shows that the LMO nanoparticles are homogeneously distributed in the CNT-entangled mesh. The high contrast cross-sectional image in Figure 5.1c and the rectangular area with a higher

magnification in Figure 5.1d indicate that the bright LMO nanoparticles are impregnated along the thickness direction of the CNT films to construct the 3D composite structure. Different from the traditional electrode preparation method through the mixing of active materials, binder materials, and conductive additives, this binder-free 3D structure avoids particle aggregation and non-uniform distribution. These highly conductive CNT bundles and the absence of non-conducting polymeric binder can provide high lithium ion flux and conduct pathways, and further benefit the energy and power density.

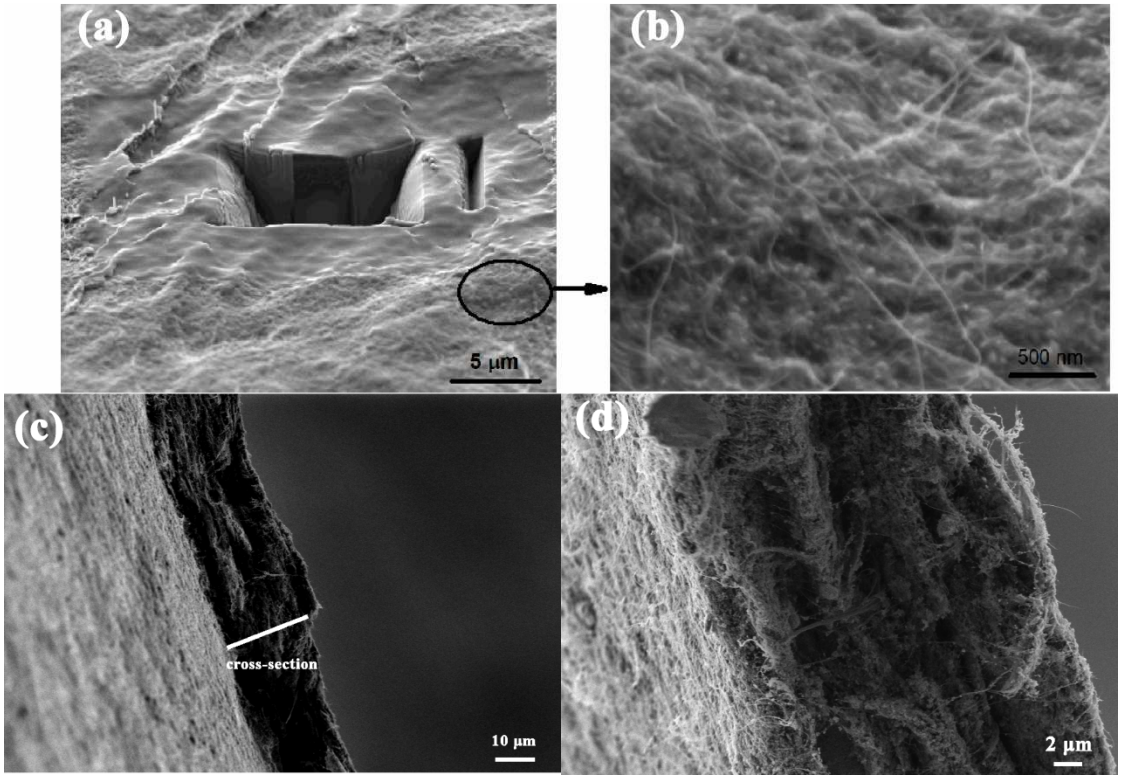

Figure 5.1 (**a**) SEM image of the LMO/CNT film composite with a milled trapezoid trench showing the cross section. (**b**) Magnified SEM image of the marked top-view area in (**a**). (**c**) A cross-sectional view of the LMO/CNT film composite and (**d**) the magnified image of cross-sectional of LMO/CNT.

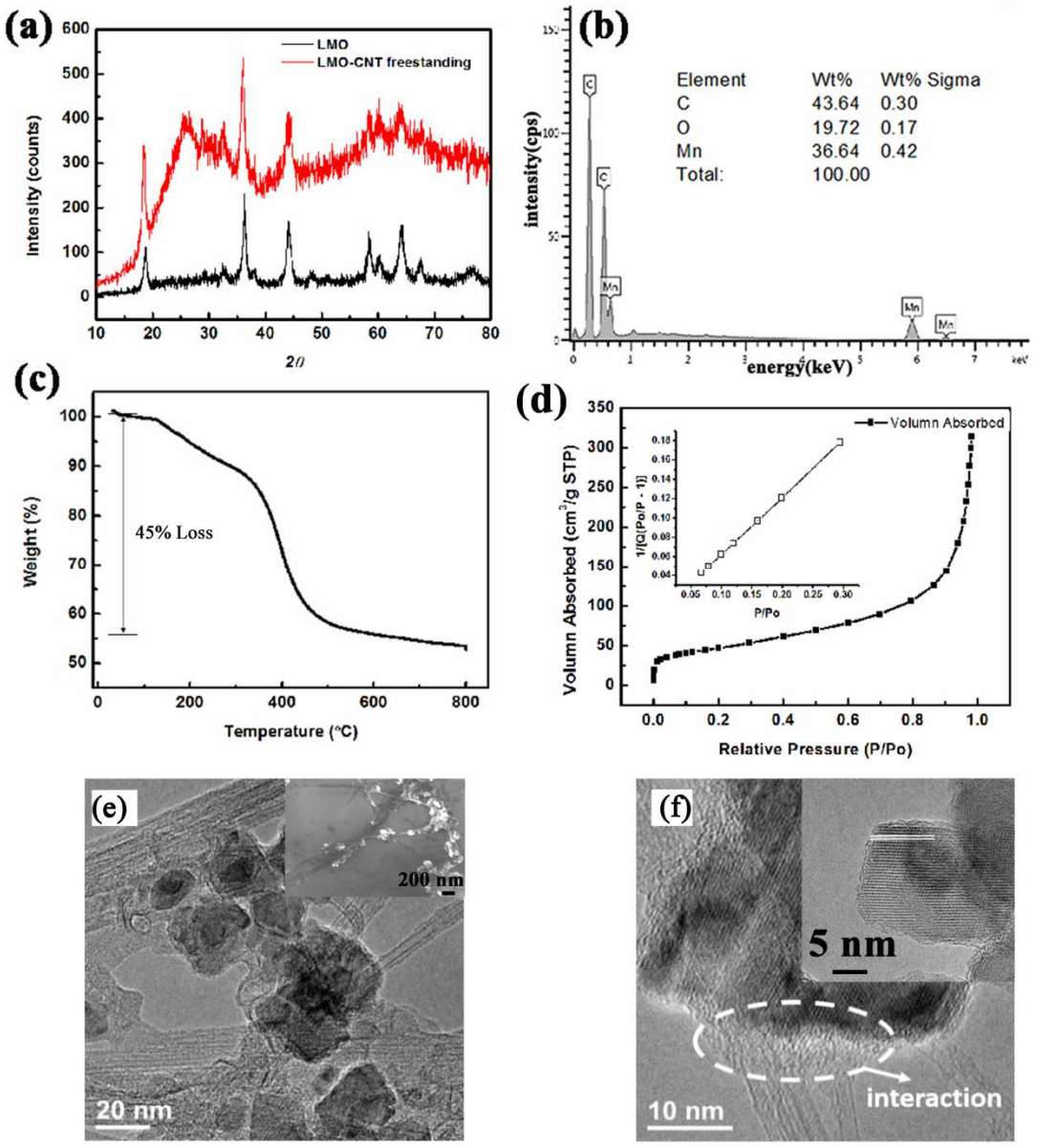

Figure 5.2 (**a**) XRD patterns of the pristine LMO and freestanding LMO/CNT film composite. (**b**) EDX spectroscopy and quantitative table of elements. (**c**) TGA curve of the LMO/CNT composite. (**d**) Nitrogen isothermal. (**e**) TEM image of individual CNTs with LMO nanoparticles from the LMO/CNT film composite after intensive ultrasonication; The inset SEM image of individual CNTs with LMO nanoparticles from the LMO/CNT film composite after intensive ultrasonication. (**f**) HRTEM image showing the interaction area between CNTs and LMO; the inset image shows individual LMO nanoparticles with well-resolved lattice fringes.

Figure 5.2a displays the XRD patterns of the LMO/CNT film composite and the pure LMO nanoparticles prepared using the same method without the CNT film. The characteristic peaks, which are identical in position to each other in both patterns, are assigned to the LMO nanoparticles with the *Fd3m* spinel structure. The intensity of these peaks after LMO was deposited in CNT is not distinctly attenuated, indicating a considerable amount of LMO in the film composite. EDX spectroscopy in Figure 5.2b confirms the existence of three major elements of C, Mn, and O. CNT is the primary carbon source, and Mn comes from LMO while the source of O is relatively complicated considering LMO and O-containing functional groups on CNT. According to the quantitative report (Inset in Figure 5.2b) and considering the accuracy of EDX results, the weight percentage of the CNT films is approximately 44%. The mass loading of LMO is then 56% assuming the rest part of the composite are all LMO nanoparticles. Figure 5.2c presents the TGA curve for the LMO/CNT composite. Typically, CNTs are completely burnt out at 800˚C where the curve arrives at a stable status. The weight percentage of remaining LMO nanoparticles is determined to be ~55%, which is in good agreement with the EDX results. The composite has a high surface area of 160 m^2 g^{-1} calculated with BET method (Figure 5.2d). Obviously, the large surface area and 3D structure are favorable to efficient electrolyte infiltration and confinement of $Mn^{3+/4+}$ ions from dissolving into electrolyte during the Li^+ intercalation and de-intercalation processes.

To probe the interaction between the LMO nanoparticles and CNTs in the 3D structure, we carried out TEM characterization of the LMO/CNT composite. The TEM samples were prepared by the ultrasound processing by immersing the composite in ethanol under a high frequency and power of 24 kHz and 200 W with constant output

amplitude for 1 hour. After intensive ultrasonication, both individual CNTs and LMO nanoparticles could be achieved in the dilute TEM samples and are clearly shown in the SEM image (Inset in Figure 5.2e). Although experienced the strong forces generated by the ultrasound, it is apparently seen that the LMO nanoparticles are still firmly anchored on the surface of CNTs and some agglomerated at the crossing of nanotubes. The corresponding TEM image (Figure 5.2e) also shows that CNTs substantially connect with the LMO nanoparticles. High-resolution TEM (HRTEM) in Figure 5.2f reveals the amorphous interaction area between each other in details. As denoted in the HRTEM of a single nanocrystal in the inset of Figure 5.2f, the inter-planar spacing of 4.86 Å could be assigned to the (111) planes of LMO, which is consistent with the XRD analysis. All these results suggest that the *in-situ* growth of LMO nanoparticles interacts with CNT films *via* chemical bonding. The presence of chemical bonding would help immobilize the LMO nanoparticles on the CNT bundles during the charge-discharge and especially stretching-releasing cycling process, which enables the composite to be a promising cathode material for a stretchable lithium-ion battery.

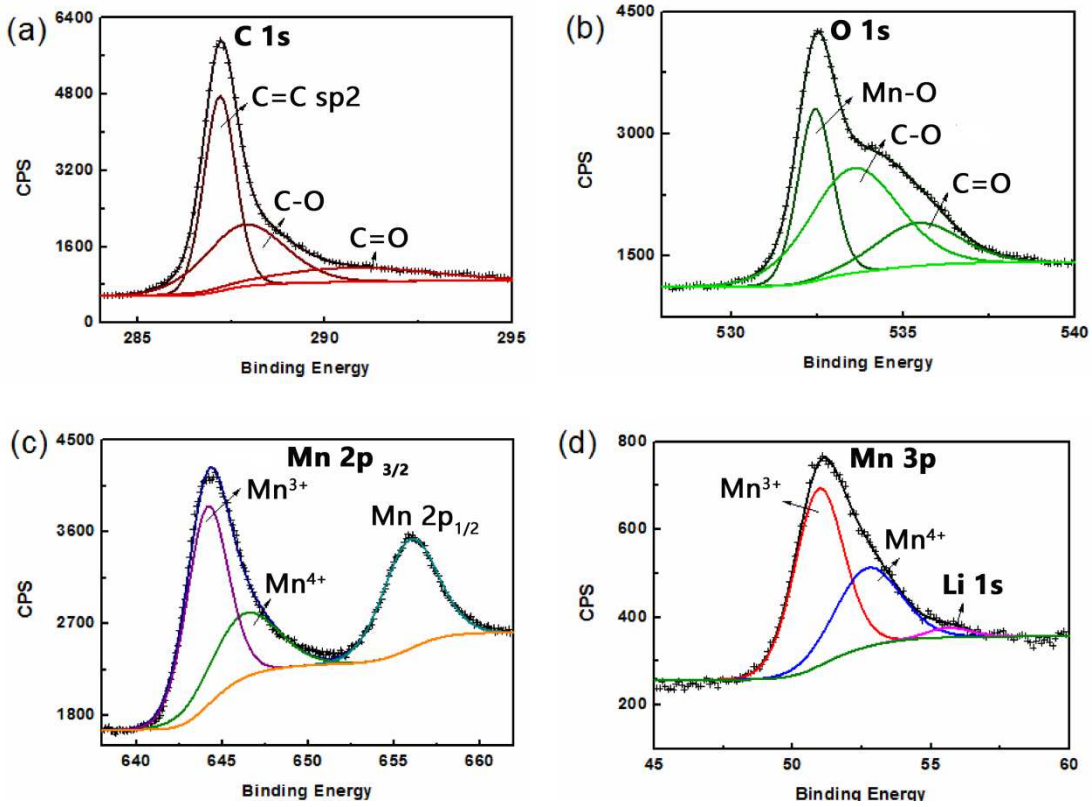

Figure 5.3 XPS spectra of (**a**) C 1s; (**b**) O 1s; (**c**) Mn 2p; and (**d**) Mn 3p with Li 1s peaks for the LMO/CNT film composite.

XPS was employed to confirm the chemical bonding between LMO and CNT further. As shown in Figure 5.3a, C 1s peak is deconvoluted into three independent peaks including the primary peak with a binding energy at 287.2 eV, which is attributed to -C=C- sp^2 bonds of the CNTs. The -C-O- and -C=O peaks respectively shifting towards the high-energy side by 0.8 eV and 2.8 eV are attributed to carboxyl and carbonyl groups on CNTs. These functional groups come from the slight functionalization during the acid purification of CNTs. Similarly, the O 1s core-level peak (Figure 5.3b) is also a convolution of three sub-peaks: the main peak at 532.5 eV is assigned to the Mn-O bonds constituting the framework of LMO; the peak at 533.6

eV is attributed to the -C-O- bonds bridging the CNT and LMO;[12] and the peak at the 535.5 eV belongs to the carbonyl groups of -C=O on CNT surface . However, it is worth noting that different from the -C-O- part in C 1s peak with a lower relative area ratio (by integrating intensities) to the main peak *i.e.* C=C sp^2 of C 1s, the -C-O- part in O 1s peak is more pronounced, and its relative area ratio to the main peak of O 1s is obviously higher. This evidence implies that the *in-situ* growth of LMO transits from an intermediate state of -C-O and Mn bonds to form the metal oxide base corresponding to the amorphous interaction area between LMO and CNT, and then that LMO nanoparticles are growing *via* lithiation. In the Mn 2p core level spectrum (Figure 5.3c), Mn $2p_{3/2}$ peak is located at 644.4 eV between two oxidation states Mn^{3+} (644.3 eV) and Mn^{4+} (646.3 eV). The energy separation between the Mn $2p_{3/2}$ and Mn $2p_{1/2}$ peaks is 11.6 eV, indicating that the stoichiometric LMO has been synthesized as identified by Ramana et al..[13] Note that the peak positions of both O 1s and Mn 2p shift ~2.4 eV with the entire C 1s peak to the higher binding energy than the pristine LMO with 530.1 eV and 641.9 eV for these two core levels. This coincidence also strengthens the existence of chemical bonding between LMO and CNT. Figure 5.3d shows the Mn 3p peak consisting of Mn^{3+}/Mn^{4+} states and the Li 1s peak with a low intensity at 55 eV, confirming that LMO is forming via the lithiation as the above implications reveal.

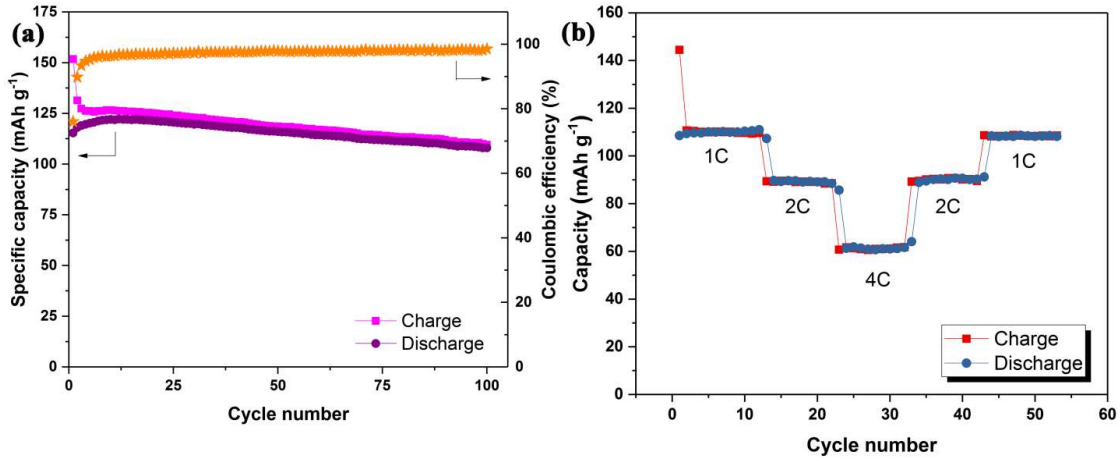

Figure 5.4 (**a**) Capacity retention of LMO/CNT. (**b**) Rate capability with various current densities.

To further demonstrate the advantage of the synergistic effect of the freestanding LMO/CNT film, electrochemical behavior was also recorded. Long-term cycling performance was examined by carrying out GCD measurement to evaluate the practical stability. Because of the high conductivity of the CNT framework in the composite and the *in-situ* chemical bond formation, which facilitates charge transfer, the charge capacity at the first cycle is ~152 mAh g^{-1} at the high current density of 1 C (~150 mA g^{-1}) as shown in Figure 5.4a. The discharge capacity starts from the initial 115 mAh g^{-1} and stabilizes at 108 mAh g^{-1} after 100 cycles. The capacity retention maintains at ~94% for such a long-term cycling with an average discharge capacity of 115 mAh g^{-1}. The Coulombic efficiency is increasing from the early-stage value of 76% to close to 100% at the end of cycling. The gap between the charge and discharge curves is gradually reduced as the cycling progresses, and an equilibrium was finally reached.

The rate capability of the LMO/CNT composite was also evaluated at high current densities of 1 C, 2 C, and 4 C (Figure 5.4b). At the 4 C rate, the LMO/CNT composite delivers a discharge capacity of 62 mAh g^{-1}. After more than 40 cycles at various current densities, the reversible capacity can be recovered to ~108 mAh g^{-1} when the current density was turned back to 1 C, which is close to its original value and also demonstrates its excellent cycling stability.

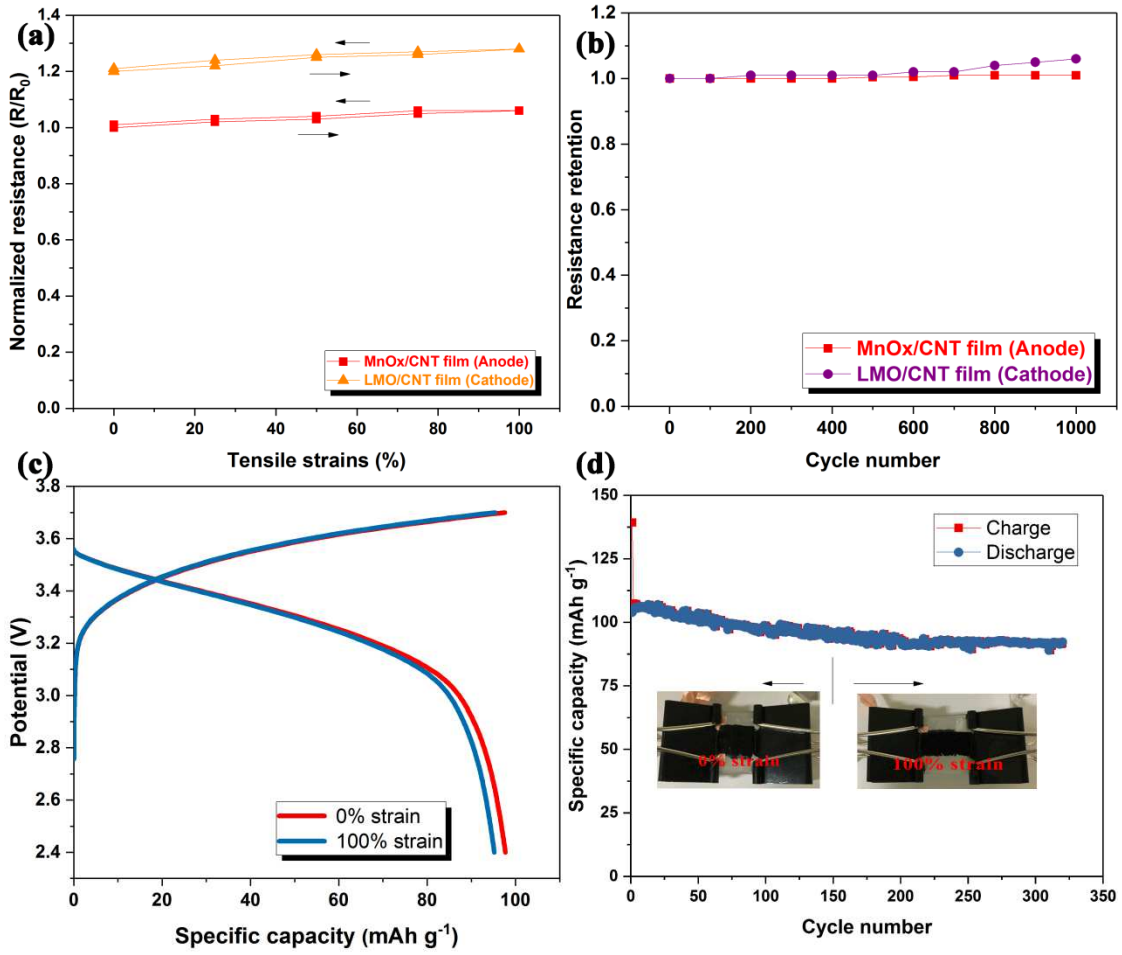

Figure 5.5 (**a**) Resistance versus tensile strains of the wrinkled MnO_x/CNT and LMO/CNT films subjected to 100% tensile strains (both stretching and releasing); (**b**) Resistance as a function of mechanical cycles between strains of 0 to 100%. (**c**) Typical charge-discharge curves before and after 100% strain and (**d**) cycling performance of the full cell.

The primary objective is to evaluate the full-cell electrochemical performance of the stretchable lithium-ion battery, which is a very critical and challenging step toward its practical application as a fully deformable power source. Herein, an all-manganese-based lithium ion battery was assembled with the wrinkled LMO/CNT cathode coupled with a wrinkled MnO_x/CNT anode. The binder-free MnO_x/CNT film

electrode has been investigated as an appealing, flexible anode material with high specific capacity and stable cycling performance at various current densities, indicating its robustness and stability as a candidate for stretchable anode material. It is also believed that the strong integrity of active materials with CNT scaffold in both films help to maintain the high electrochemical properties. To better explain and demonstrate the stretchability and stability of the wrinkled cathode and anode electrodes, a series of electrical tests was performed. Figure 5.5a shows the resistance variation of the LMO/CNT film at different strain levels. The conductivity of both LMO/CNT and MnO_x/CNT films did not increase much (< 7%) with the large strain up to 100%. Without changing the original film structure while stretching, the wrinkled LMO/CNT and MnO_x/CNT films accommodate the applied tensile strains by simply adjusting the wrinkling structure, resulting in nearly constant resistance, which proves their candidacy as electrodes for the stretchable lithium-ion battery. The wrinkled LMO/CNT and MnO_x/CNT films with repeated stretching-releasing processes between 0 and 100% strain were also tested to explore the mechanical durability of the films, respectively. Importantly, there is no noticeable increase in resistance (less than 6%) of both electrodes after 1000 stretching-releasing cycles (Figure 5.5b), which demonstrate robust mechanical stability and high reversibility compared to the serpentine interconnects-based stretchable lithium-ion battery and other "wavy" electrodes without chemical bonding.[6-8] A full cell of the all-manganese-based Li-ion battery was assembled for electrochemical testing. For the MnO_x/CNT film anodes, a pre-lithiation treatment was performed, which was constituted of three GCD cycles in the potential range 3 ~ 0.01 V vs. Li/Li^+, to eliminate the first cycling irreversible capacity loss. Figure 5.5c shows the voltage

profiles of the battery, which is cycled between 3.7 and 2.4V at 1 C. The full cell was designed on the basis of capacity limitation of the cathode. The battery performance was first tested at 0% strain, in which the full cell can deliver an average voltage above 3 V, and is also able to achieve discharge capacities of ~97 mAh g^{-1}. More importantly, the capacity exhibits good cycling performance after 150 cycles with the tensile strain as high as 100%, i.e. 88% retention is achieved after 300 GCD cycles (Figure 5.5d) and the CE is approaching 100% since the 10th cycle. The small capacity loss of 0.04% per cycle is very encouraging and indicates an outstanding cycling stability and stretchability of the full cell. To the best of our knowledge, this battery offers the highest cycling stability for stretchable lithium-ion batteries reported to date.[6] The superior electrochemical and mechanical performance of the all manganese-based binder-free stretchable Li-ion battery could be attributed to the following aspects: (1) The CNT scaffolds in both anode and cathode help in maintaining the mechanical integrity of the full cell with high electrical conductivity and adjustable mechanical stability. (2) Even without binders, the *in-situ* formed chemical bond between CNT and active materials facilitates charge transfer and withstands the large stain under stretching. The chemical bonding is considered as a key solution to satisfying the mechanical requirement for a stretchable lithium-ion battery.

5.4 Conclusions

In summary, we fabricated a stretchable cathode material for lithium-ion batteries by the *in-situ* growth of $LiMn_2O_4$ nanocrystals into three-dimensional CNT films. Based on various characterization results, we have confirmed that the *in-situ* growth of the active materials was rendered by the chemical bonding on the CNT

scaffolds. For the first time, an all manganese-based binder-free Li-ion battery was demonstrated with the excellent electrochemical performance and great stretchability. The stretchable MnO_x/CNT // LMO/CNT full cell has shown a satisfied average specific capacity of ~97 mAh g^{-1} with excellent cycling stability over 300 cycles and high stretchability (100% strain). In addition, this stretchable lithium-ion battery with the unique structure can be scaled up as the power source for commercial fabrication without complicated interconnects. Together with low cost and environmental friendly of the all manganese-based binder-free design, this research will open up the possibility of developing reliable and green stretchable lithium-ion batteries with high cycling performance.

REFERENCES

1 Xie, K.; Wei, B. Materials and Structures for Stretchable Energy Storage and Conversion Devices. *Adv. Mater.* **2014**, 26, 3592–3617.

2 Li, X.; Gu, T.; Wei, B. Dynamic and Galvanic Stability of Stretchable Supercapacitors. *Nano Lett.* **2012**, *12*, 6366–6371.

3 Gu, T.; Wei, B. Fast and Stable Redox Reaction of MnO_2/CNT Hybrid Electrodes for Dynamically Stretchable Pseudocapacitors. *Nanoscale* **2015**, *7*, 11626–11632.

4 Gu, T., Wei. B. High-Performance All-Solid-State Asymmetric Stretchable Supercapacitors Based on Wrinkled MnO_2/CNT and Fe_2O_3/CNT Macrofilms. *J. Mater. Chem. A* **2016**, *327*, 1603–1607.

5 Gu, T.; Wei, B. All-Solid-State Stretchable Pseudocapacitors Enabled by Carbon Nanotube Film-Capped Sandwich-like Electrodes. *ACS Appl. Mater. Interfaces* **2016**, *8*, 25243–25250.

6 Xu, S.; Zhang, Y.; Cho, J.; Lee, J.; Huang, X.; Jia, L.; Fan, J. a; Su, Y.; Su, J.; Zhang, H.; *et al.* Stretchable Batteries with Self-Similar Serpentine Interconnects and Integrated Wireless Recharging Systems. *Nat. Commun.* **2013**, *4*, 1543.

7 Weng, W.; Sun, Q.; Zhang, Y.; He, S.; Wu, Q.; Deng, J.; Fang, X.; Guan, G.; Ren, J.; Peng, H. A Gum-like Lithium-Ion Battery Based on a Novel Arched Structure. *Adv. Mater.* **2015**, *27*, 1363–1369.

8 Liu, W.; Chen, Z.; Zhou, G.; Sun, Y.; Lee, H. R.; Liu, C.; Yao, H.; Bao, Z.; Cui, Y. 3D Porous Sponge-Inspired Electrode for Stretchable Lithium-Ion Batteries. *Adv. Mater.* **2016**, *28*, 3578–3583.

9 Qin, J.; Zhang, Q.; Cao, Z.; Li, X.; Hu, C.; Wei, B. MnOx/SWCNT Macro-Films as Flexible Binder-Free Anodes for High-Performance Li-Ion Batteries. *Nano Energy* **2013**, *2*, 733–741.

10 Lee, S.; Cho, Y.; Song, H. K.; Lee, K. T.; Cho, J. Carbon-Coated Single-Crystal LiMn 2O 4 Nanoparticle Clusters as Cathode Material for High-Energy and High-Power Lithium-Ion Batteries. *Angew. Chemie - Int. Ed.* **2012**, *51*, 8748–8752.

11 Yoshimura, M.; Byrappa, K. Hydrothermal Processing of Materials: Past, Present and Future. *J. Mater. Sci.* **2008**, *43*, 2085–2103.

12 Yan, G.; Li, X.; Wang, Z.; Guo, H.; Wang, J.; Peng, W.; Hu, Q. Effects of 1-Propylphosphonic Acid Cyclic Anhydride as an Electrolyte Additive on the High Voltage Cycling Performance of graphite/$LiNi_{0.5}Co_{0.2}Mn_{0.3}O_2$ Battery. *Electrochim. Acta* **2015**, *166*, 190–196.

13 Ramana, C. V.; Massot, M.; Julien, C. M. XPS and Raman Spectroscopic Characterization of $LiMn_2O_4$ Spinels. *Surf. Interface Anal.* **2005**, *37*, 412–416.

Chapter 6

CONCLUSIONS AND FUTURE WORK

6.1 Summary of the Research Contributions

This dissertation covers the original research works in the emerging area of CNT film-based nanocomposite electrodes for stretchable energy storage devices, in particular stretchable pseudocapacitors as well as asymmetric stretchable supercapacitors and stretchable lithium-ion batteries. The progressive research focused on developing various nanocomposites and structural strategies evolving from stretchable pseudocapacitors in Chapters 2 and 3 to asymmetric stretchable supercapacitors in Chapter 4, followed by an all-manganese-based binder-free stretchable lithium-ion battery in Chapter 5. The high stretchability, robustness, adhesion, inherent superior conductivity, large specific surface area, and porous structure of CNT films could be fully taken advantage of to enhance the electrochemical and mechanical (stretching and bending) performance of the incorporated active materials in the nanocomposites. In the above illustration, we have demonstrated that CNT films act as a very important component to construct future stretchable energy storage devices.

To be specific, in Chapter 2, we reported the electrochemical performance of dynamically stretchable pseudocapacitors using buckled MnO_2/CNT hybrid electrodes for the first time. The extremely small relaxation time constant of less than 0.15 s indicates a fast redox reaction at the MnO_2/CNT hybrid electrodes, securing a stable electrochemical performance for stretchable pseudocapacitors. This finding and the

fundamental understanding gained from the pseudocapacitive behavior coupled with mechanical deformation under a dynamic stretching mode would guide to further improve their overall performance including a higher power density than LIBs, a higher energy density than EDLCs, and a long-life cycling stability.

Then this relatively low anchoring amount of active materials on stretchable CNT substrate stimulates the fabrication of novel stretchable electrode design as discussed in Chapter 3. All-solid-state stretchable sandwich-like pseudocapacitors by CNT capping with stable electrochemical and mechanical performance were fabricated. The results indicate that the sandwich-like structure approach to design stretchable electrodes deserves considerable attention on stretchable pseudocapacitors. This stretchable pseudocapacitor based on the CNT/MnO_2-FCNT/CNT configuration overcomes the limitation of the maximum mass loading of active pseudo-capacitive materials. The enhanced pseudo-capacitive performances result from the synergistic effect of the all-solid-state and binder-free structure: (1) faster ion diffusion rates and charge transport at electrode/electrolyte interfaces and (2) improved the mechanical property to mitigate the electrode degradation caused by ion insertion/extraction during charge-discharge and mechanically stretching-releasing cycles. This new component-level design offers an efficient way to improve the electrochemical performance of stretchable pseudocapacitors, and more importantly, this concept can be extended for improving the performance of other electrochemical systems such as stretchable supercapacitors, lithium-ion batteries, lithium-sulfur batteries, and solar cells, and accelerate its applications for wearable and implantable electronics.

By expanding the work of MnO_2/CNT based stretchable pseudocapacitors and solving the issue that stretchable single-cell energy storage devices suffering from a

relatively low operating voltage and thus a low energy density, in Chapter 4, we discussed an all-solid-state asymmetric stretchable supercapacitor with a high energy density using the wrinkled MnO_2/CNT hybrid film as a positive electrode and the wrinkled Fe_2O_3/CNT composite film as a negative electrode in a neutral gel electrolyte. Due to the high specific capacitance and excellent rate performance of MnO_2/CNTs and Fe_2O_3/CNTs, as well as the synergistic effects of the two electrodes with an optimized potential window, an optimized asymmetric stretchable supercapacitor can be reversibly cycled in the voltage window between 0 and 2 V, and shows a supreme energy density of 45.8 Wh kg^{-1} (corresponding power density of 0.41 kW kg^{-1}). Additionally, the ASS also exhibits exceptional cycling stability and durability, with 98.9% specific capacitance retained even after 10000 electrochemical cycles at multiple strains.

However, the sufficiently stretchable lithium-ion battery is still underdeveloped, and that is one of the biggest challenges preventing us from realizing fully deformable power sources. The majority of the reports have focused on the stretchable electrochemical double-layered supercapacitors due to their relatively less difficulty in fabrication and operation. Finally, in Chapter 5, we report a binder-free, all-manganese-based stretchable full Li-ion battery. The wrinkled LMO/CNT was synthesized using a low-temperature hydrothermal synthesis of a cathode material for the stretchable lithium-ion battery by the in-situ growth of LMO nanocrystals inside three-dimensional CNT film networks. The LMO/CNT film composite has demonstrated the chemical bonding between the LMO active materials and CNT scaffolds, which is the most important characteristic of the stretchable electrodes. When coupled with a wrinkled MnO_x/CNT film anode, a binder-free,

all-manganese-based stretchable full battery cell was assembled, which delivered a high average specific capacity of ~97 mAh g^{-1} and stabilized after over 300 cycles with an enormous strain of 100%. Furthermore, combining with other merits such as low cost, natural abundance and environmentally friendly, our all-manganese design is expected to accelerate the practical applications of stretchable lithium-ion batteries for fully flexible electronics.

6.2 Suggested Future Research Work

There is no doubt that research in stretchable energy storage devices is very promising and provides researchers with various background great opportunities to explore novel concepts. In the past few years, research in this area has witnessed significant advances and substantial achievements since 2009, which has benefitted from the progress on the discovery of novel nanomaterials as well as the design optimization of structural configurations. However, there still exist many challenges to be overcome before their large-scale commercial application.

6.2.1 Intrinsically stretchable electrodes

It is desirable to develop intrinsically stretchable electrode materials to meet all the specific requirements for a variety of applications in stretchable energy storage systems. Theoretical prediction and experimental study in new elastic electrode materials in stretchable energy storage are greatly expected. By achieving intrinsically stretchable electrodes, we do not have to rely on the extra stretchable scaffolds (e.g. buckled CNT film, textile materials or serpentine-connection) to make the electrodes fully stretchable. The real difficulty in mass production is to find reliable, low-cost,

highly controllable, and large-scale manufacturing methods to fabricate the intrinsically stretchable electrodes.

6.2.2 Stretchable gel electrolytes for LIBs

In Chapter 5, a traditional liquid electrolyte for LIBs was used and could be replaced by intrinsically stretchable electrolytes. The study of stretchable gel electrolytes with a comparable ionic conductivity of liquid electrolyte becomes an urgent problem. Unlike the stretchable gel electrolyte well developed for stretchable supercapacitors, intrinsically solid-state electrolytes with high stretchability is underdeveloped and needs further attention for stretchable LIBs.[1-3] Development of reliable stretchable all-solid-state gel electrolytes should have the following characteristics: high ionic conductivity, high strain, enough mechanical strength, and good interfacial adhesion with stretchable electrodes. Besides, this will also lower the package cost and eliminate the inherent danger of liquid electrolytes.

6.2.3 Beyond stretchable energy storage devices

Although LIBs and SCs are the two most prominent stretchable energy storage fields this research area should cover a wider range of devices with different applications. Other stretchable energy applications such as stretchable metal-O_2 battery, stretchable Na-ion batteries, stretchable Li-S batteries, and stretchable Li-ion capacitors are also desirable and promising in many areas.[4-7] Therefore, related work in this area is highly desired.

REFERENCES

1 Zhao, C.; Wang, C.; Yue, Z.; Shu, K.; Wallace, G. G. Intrinsically Stretchable Supercapacitors Composed of Polypyrrole Electrodes and Highly Stretchable Gel Electrolyte. *ACS Appl. Mater. Interfaces* **2013**, *5*, 9008–9014.

2 Yang, Z.; Deng, J.; Chen, X.; Ren, J.; Peng, H. A Highly Stretchable, Fiber-Shaped Supercapacitor. *Angew. Chemie - Int. Ed.* **2013**, *52*, 13453–13457.

3 Lee, G.; Kim, D.; Kim, D.; Oh, S.; Yun, J.; Kim, J.; Lee, S.-S.; Ha, J. S. Fabrication of a Stretchable and Patchable Array of High Performance Micro-Supercapacitors Using a Non-Aqueous Solvent Based Gel Electrolyte. *Energy Environ. Sci.* **2015**, *8*, 1764–1774.

4 Liu, Q.-C.; Xu, J.-J.; Xu, D.; Zhang, X.-B. Flexible Lithium-Oxygen Battery Based on a Recoverable Cathode. *Nat. Commun.* **2015**, *6*, 7892.

5 Chevrier, V. L.; Ceder, G. Challenges for Na-Ion Negative Electrodes. *J. Electrochem. Soc.* **2011**, *158*, A1011.

6 Zhou, G.; Li, L.; Wang, D. W.; Shan, X. Y.; Pei, S.; Li, F.; Cheng, H. M. A Flexible Sulfur-Graphene-Polypropylene Separator Integrated Electrode for Advanced Li-S Batteries. *Adv. Mater.* **2015**, *27*, 641–647.

7 Aravindan, V.; Gnanaraj, J.; Lee, Y. S.; Madhavi, S. Insertion-Type Electrodes for Nonaqueous Li-Ion Capacitors. *Chem. Rev.* **2014**, *114*, 11619–11635.

Appendix A

SCIENTIFIC AND TECHNICAL CONTRIBUTIONS DURING PH.D.

1 **Gu, T.**; Cao, Z.; Wei, B. All-Manganese-Based Binder-Free Stretchable Lithium-Ion Batteries *Adv. Energy Mater.*DOI:10.1002/aenm.201700369.

2 **Gu, T.**; Wei, B. All-Solid-State Stretchable Pseudocapacitors Enabled by Carbon Nanotube Film-Capped Sandwich-like Electrodes. *ACS Appl. Mater. Interfaces* **2016**, *8*. 25243–25250.

3 Bondade, R.; Zhang, Y.; Wei, B.; **Gu, T.**; Chen, H.; Ma, D. Integrated Auto-Reconfigurable Power Supply Network with Multi-Directional Energy Transfer for Self-Reliant Energy Harvesting Applications. *IEEE Trans. Ind. Electron.* **2016**, *63*, 2850–2861.

4 **Gu, T.**, Wei. B. High-Performance All-Solid-State Asymmetric Stretchable Supercapacitors Based on Wrinkled MnO_2/CNT and Fe_2O_3/CNT Macrofilms. *J. Mater. Chem. A* **2016**, *4*, 12289–12295.

5 **Gu, T.**; Wei, B. Fast and Stable Redox Reaction of MnO_2/CNT Hybrid Electrodes for Dynamically Stretchable Pseudocapacitors. *Nanoscale* **2015**, *7*, 11626–11632.

6 Liang, K.; **Gu, T.**; Cao, Z.; Tang, X.; Hu, W.; Wei, B. In Situ Synthesis of SWNTs@MnO_2/polypyrrole Hybrid Film as Binder-Free Supercapacitor Electrode. *Nano Energy* **2014**, *9*, 245–251.

7 Xu, P.; **Gu, T.**; Cao, Z.; Wei, B.; Yu, J.; Li, F.; Byun, J.-H.; Lu, W.; Li, Q.; Chou, T.-W. Carbon Nanotube Fiber Based Stretchable Wire-Shaped Supercapacitors. *Adv. Energy Mater.* **2014**, *4*, 1300759.

8 Liang, K.; Wang, N.; Zhou, M.; Cao, Z.; **Gu, T.**; Zhang, Q.; Tang, X.; Hu, W.; Wei, B. Mesoporous $LaNiO_3$/NiO Nanostructured Thin Films for High-Performance Supercapacitors. *J. Mater. Chem. A* **2013**, *1*, 9730–9736.

9 Li, X.; **Gu, T.**; Wei, B. Dynamic and Galvanic Stability of Stretchable Supercapacitors. *Nano Lett.* **2012**, *12*, 6366–6371.

Appendix B

PERMISSION FOR USING COPYRIGHTED MATERIALS

Copyright Clearance Center RightsLink®

Home | Account Info | Help

RSCPublishing

Title:	Textile energy storage in perspective	Logged in as: Taoli Gu
Author:	Kristy Jost,Genevieve Dion,Yury Gogotsi	Account #: 3001114802
Publication:	Journal of Materials Chemistry A	LOGOUT
Publisher:	Royal Society of Chemistry	
Date:	Feb 20, 2014	

Copyright © 2014, Royal Society of Chemistry

Order Completed

Thank you for your order.

This Agreement between Taoli Gu ("You") and Royal Society of Chemistry ("Royal Society of Chemistry") consists of your license details and the terms and conditions provided by Royal Society of Chemistry and Copyright Clearance Center.

Your confirmation email will contain your order number for future reference.

Printable details.

License Number	4053841403993
License date	Feb 21, 2017
Licensed Content Publisher	Royal Society of Chemistry
Licensed Content Publication	Journal of Materials Chemistry A
Licensed Content Title	Textile energy storage in perspective
Licensed Content Author	Kristy Jost,Genevieve Dion,Yury Gogotsi
Licensed Content Date	Feb 20, 2014
Licensed Content Volume	2
Licensed Content Issue	28
Type of Use	Thesis/Dissertation
Requestor type	academic/educational
Portion	figures/tables/images
Number of figures/tables/images	1
Distribution quantity	1
Format	print and electronic
Will you be translating?	no
Order reference number	
Title of the thesis/dissertation	CARBON NANOTUBE FILM BASED NANOCOMPOSITE FOR STRETCHABLE ENERGY STORAGE DEVICES
Expected completion date	Mar 2017
Estimated size	140
Requestor Location	Taoli Gu 130 Academy Street Room 126 NEWARK, DE 19716 United States Attn: Taoli Gu
Billing Type	Invoice
Billing address	Taoli Gu 130 Academy Street Room 126 NEWARK, DE 19716 United States Attn: Taoli Gu
Total	0.00 USD

Copyright Clearance Center RightsLink®

Home | Account Info | Help

Title: Stretchable Supercapacitors Based on Buckled Single-Walled Carbon-Nanotube Macrofilms

Author: Cunjiang Yu,Charan Masarapu,Jiepeng Rong,Bingqing Wei,Hanqing Jiang

Publication: Advanced Materials

Publisher: John Wiley and Sons

Date: Aug 12, 2009

Copyright © 2009 WILEY-VCH Verlag GmbH & Co. KGaA, Weinheim

Logged in as:
Taoli Gu
Account #:
3001114802

LOGOUT

Order Completed

Thank you for your order.

This Agreement between Taoli Gu ("You") and John Wiley and Sons ("John Wiley and Sons") consists of your license details and the terms and conditions provided by John Wiley and Sons and Copyright Clearance Center.

Your confirmation email will contain your order number for future reference.

Printable details.

License Number	4053900659103
License date	Feb 21, 2017
Licensed Content Publisher	John Wiley and Sons
Licensed Content Publication	Advanced Materials
Licensed Content Title	Stretchable Supercapacitors Based on Buckled Single-Walled Carbon-Nanotube Macrofilms
Licensed Content Author	Cunjiang Yu,Charan Masarapu,Jiepeng Rong,Bingqing Wei,Hanqing Jiang
Licensed Content Date	Aug 12, 2009
Licensed Content Pages	5
Type of use	Dissertation/Thesis
Requestor type	University/Academic
Format	Print and electronic
Portion	Figure/table
Number of figures/tables	1
Original Wiley figure/table number(s)	Figure 1 and 3
Will you be translating?	No
Title of your thesis / dissertation	CARBON NANOTUBE FILM BASED NANOCOMPOSITE FOR STRETCHABLE ENERGY STORAGE DEVICES
Expected completion date	Mar 2017
Expected size (number of pages)	140
Requestor Location	Taoli Gu 130 Academy Street Room 126 NEWARK, DE 19716 United States Attn: Taoli Gu
Publisher Tax ID	EU826007151
Billing Type	Invoice
Billing address	Taoli Gu 130 Academy Street Room 126 NEWARK, DE 19716